

REAL TIME TRIAXIAL RESISTIVITY AND PORE PRESSURE PENETRATION
MEASUREMENTS FOR MONITORING SATURATION AND ELECTRICAL
PROPERTY ALTERATIONS UNDER STRESS

by
A. Rixon

© Copyright by A. Rixon, 2016

All Rights Reserved

A thesis submitted to the Faculty and the Board of Trustees of the Colorado School of Mines in partial fulfillment of the requirements for the degree of Master of Science (Petroleum Engineering).

Golden, Colorado

Date _____

Signed: _____

A. Rixon

Signed: _____

Dr. Azra N. Tutuncu
Thesis Advisor

Golden, Colorado

Date _____

Signed: _____

Dr. Erdal Ozkan
Professor and Department Head
Department of Petroleum Engineering

ABSTRACT

The use of Archie's equation relating water saturation in clean sandstone formations to the electrical resistivity of the formations and the fluid properties has been key in electrical log interpretation. Archie's equation has been widely used for most sedimentary rocks for fluid saturation evaluation since its first application in sandstones. Recent studies have shown that Archie's equation is not an accurate representation of the electrical property representation in all formations (Herrick et al. 2001; Kennedy 2006; Kennedy and Herrick 2012; Mahmood et al. 1991; Moran and Gianzero 1979; Suman and Knight 1997).

Due to the recent shale boom in the United States and throughout the world, characterization of these unconventional hydrocarbon bearing reservoirs including shale gas, tight oil, carbonates, and unconsolidated sand formations has become an area of interest. Application of Archie's equation in these formations is not considered to be accurate and may result in significant error when determining fluid saturation utilizing the electrical resistivity logs (Worthington 1982), and other properties correlated to resistivity response. Conductive mineralogy, low permeability complex pore structures, in situ stress state, and formation anisotropy are the leading causes of erroneous interpretation of the resistivity data collected in the field through resistivity logs in shale reservoirs.

The results of an experimental investigation on the electrical impedance spectroscopy for sandstones and organic-rich shale (Archie and non-Archie) formations have been presented in this research study. The main objective of the study is to examine the effects of stress state, pore geometry changes, tracking of the fluid migration, and rock-fluid interactions on the electrical properties of the formations investigated. Berea Sandstone, Eagle Ford Shale, and Pierre Shale have been studied in detail and the results of the findings of the study are presented here.

A resistivity measurement system has been designed and implemented in a triaxial cell. The core samples and the pore fluid injection system were electrically isolated for accurate measurements of the electrical properties. The resistivity measurements have been coupled with geomechanical deformation, compressional and shear wave velocities, absolute permeability, and XRD scans of specific core samples simultaneously studied. These parameters were monitored as a function of stress state, elevated pore pressure, and fluid composition to create a detailed understanding on the interdependence and correlations between various monitored parameters.

Experimental results from Eagle Ford and Pierre Shale samples show that increasing stress on the rock increases the resistivity of the sample. This is mainly due to the closure of the natural fractures present in the sample, reduction of nano-pore space and elimination of part of the connectivity throughout the complex rock structure as a result of the closure of the pore space. In conjunction with the reduction in resistivity, permeability decrease is observed with increased stress. These observations represent the described pore geometry changes due to the increase in stress.

Additionally, the resistivity measurements were used to track the imbibition of a brine solution through a Berea Sandstone sample. A correlation between the measured resistivity and brine salt concentration has been developed and compared to the predicted concentration from a numerical model. The computer model closely matched a portion of the measured resistivity data; however, some errors are apparent.

TABLE OF CONTENTS

ABSTRACT	iii
LIST OF FIGURES	ix
LIST OF TABLES	xvii
LIST OF SYMBOLS	xviii
LIST OF ABBREVIATIONS	xxiii
ACKNOWLEDGMENTS	xxiv
DEDICATION	xxvi
CHAPTER 1 PROJECT DESCRIPTION	1
1.1 Statement of Problem and Significance	1
1.2 Introduction and Background to Resistivity Measurements	5
1.3 Literature Review	11
1.3.1 Measurements of Resistivity Dependence on Pore Throat Geometry	12
1.3.2 Stress State Effect on Pore Geometry and Resistivity	19
1.3.3 Relationship between Water Saturation and Resistivity Measurements	24
1.3.4 Resistivity Measurements in Anisotropic Conditions	28
1.3.5 Experimental Setup	32
1.3.6 Log Analysis	33
CHAPTER 2 EXPERIMENTAL SETUP	38
2.1 Sandstone Ambient Condition Validation Measurements	38
2.2 UNGI Laboratory Triaxial Test Assembly	41

2.2.1	Triaxial Cell	42
2.2.2	Pore Pressure Electrical Isolation Endcap	48
2.2.2.1	Two Probe Triaxial Cell Resistivity Test Assembly	51
2.2.2.2	Four Probe Triaxial Cell Resistivity Test Assembly	54
2.3	Data Collection	56
2.4	Triaxial Cell Validation Test on Berea Sandstone Calibration Sample	57
CHAPTER 3 STRESS DEPENDENT ROCK PROPERTIES		60
3.1	Selection of Core Samples for Testing	60
3.1.1	Formation Specific Core Sample Inventory	61
3.1.2	Eagle Ford Sample Porosity, Pore Size Distribution and Geometry	62
3.1.2.1	Determination of Eagle Ford Sample Absolute Porosity	62
3.1.2.2	Eagle Ford #GZ-6 Pore Distribution	65
3.1.2.3	Eagle Ford #GZ-6 Mineralogy and Organic Matter Composition	66
3.1.2.4	Geomechanical Property Determination	66
3.2	Stress Dependent Permeability of the Upper Eagle Ford Samples	69
3.2.1	Pulse-Decay Permeability Measurements	72
3.2.2	Steady-State Nitrogen Permeability	74
3.2.3	Comparison of Pulse-Decay and Steady-State Permeability Measurements	80
3.2.4	High Stress Directional Dependence of Gas Permeability	80
3.3	Shale Resistivity Stress Dependence	81
3.4	Effects of Osmotic Pressures on the Interpretation of Measured Resistivity	89

CHAPTER 4 TRACKING BRINE IMBIBITION WITH RESISTIVITY MEASUREMENTS	93
4.1 Sandstone Resistivity	93
4.2 Tracking Fluid Migration Using Resistivity	97
4.3 Difficulties Tracking Brine Concentration Flow in Shales	102
CHAPTER 5 LIMITATIONS AND APPLICATIONS OF THE RESEARCH RESULTS	106
5.1 Limitations	106
5.1.1 Controlled Experimental Conditions	106
5.1.2 Utilizing Resistivity for Tracking Injection Well Fluid Flow	108
5.1.3 Sensitivities Affecting Resistivity	109
CHAPTER 6 CONCLUSIONS AND RECOMMENDATIONS	111
REFERENCES CITED	115
APPENDIX A - MATERIALS, METHODS AND LABORATORY PROCEDURES UTILIZED TO STUDY THE DEPENDENCE OF RESISTIVITY ON STRESS	119
A.1 Porosity	119
A.1.1 Absolute Porosity	119
A.1.1.1 Bulk Density	120
A.1.1.2 Pycnometer Grain Density	121
A.1.2 Scanning Electron Microscope	123
A.2 Triaxial Cell Pore Pressure Penetration Tests	124
A.2.1 Sample Preparation	124
A.2.2 Resistivity Measurements	127
A.2.2.1 Two Probe Resistivity Setup	127

A.2.2.2	Four Probe Resistivity Setup	131
A.2.2.3	Assembling the Triaxial cell for Resistivity Measurements . .	133
APPENDIX B -	TRIAXIAL CELL ASSEMBLY	135
B.1	Tubing and Valve Specifications	138
B.2	Axial and Confining Stress Control	141
B.3	Pore Pressure Control System	142
B.4	Data Acquisition System	143
B.5	Pore Pressure Control System	146
B.6	Linear Deformation Measurement System	148
B.7	Temperature Control System	148
B.8	Sonic Measurement System	149

LIST OF FIGURES

Figure 1.1	Four probe resistivity measurement setup for a cylindrical shale sample with horizontal bedding planes. Two source current electrodes sandwiched the core (A and B), while two embedded sintered electrodes are used to measure the current between the probes (Woodruff et al. 2014).	9
Figure 1.2	Measured impedance dependence on varying frequency for different electrode/filter material combinations (Wang et al. 2009). The selection to perform the resistivity measurements at 1000 Hz is made to negate the material effects on the resistivity.	10
Figure 1.3	Complexities of connectivity and how it affects the path of ion flow through porous media, an infinite number of paths are possible due to the complex and ever changing pore structure throughout a reservoir. Furthermore, due to rock-fluid interactions and depletion from production the geometric structure of a specific section of rock could continuously change over time.	14
Figure 1.4	How the flow of electrical current is restricted at the pore throats as represented by the red lines and the constrictions at the pore throats are circled in blue.	18
Figure 1.5	Relation between electrical efficiency and pore geometry, how porosity alone does not determine electrical efficiency due to either highly connected pores, or isolated vugs. Image sourced from (Herrick and Kennedy 1993).	19
Figure 1.6	Experimental results showing the relation of increased rock pressures and resistivity. Shown are the effects of varying rock pressures, from 0 psi to 20,000 psi, on the measured resistivity as displayed by the ratio of the measured resistivity at increased pressures compared to the measured resistivity at zero pressure. These results are from Dobrynin (1962).	20
Figure 1.7	Experimental results showing the effects of increased stress ranging from 0 psi to 5,000 psi on the cementation factor for a saturated Berea Sandstone core. As it can be seen, there is minimal increase in the cementation factor with increasing stress. This experimental work is from Sharma et al. (1991).	21

Figure 1.8	Experimental results showing increases in resistivity due to an increase in overburden pressure while decreases in resistivity are observed with increasing pore pressure. This can be explained by the effective stress equation which represents the stress felt by the rock matrix (Mahmood et al. 1991).	23
Figure 1.9	Normalized resistivity and percent strain increase for Pierre shale exposed to 4% KCl which is circulated at the base of the core and imbibed vertically. This shows that resistivity increases due to the swelling of the clays which reduces the pore geometry and absorption of the free water (Javalagi et al. 1991).	28
Figure 1.10	Effects of anisotropy increase from decreases in water saturation due to the preferential desaturation of the macroporous layers. The data obtained is obtained from the experimental work by (Klein et al. 1997). .	32
Figure 1.11	Varying the spacing of electrodes for four probe resistivity measurements shows that the further apart the spacing is produces lower resistivity measurements for the same sample. This work was performed by Mahmood et al. (1991).	33
Figure 1.12	Relative dip angle influence on measured resistivity. It is seen that as the dip angle increases above 45 degrees the increase in resistivity become much more rapid. This work was performed by Bittar and Rodney, (1996).	35
Figure 1.13	Rotation of the tool measured conductivity tensor to match the bedding planes of a formation (Moran and Gianzero, 1979).	36
Figure 2.1	Atmospheric resistivity measurement test setup used for validation of the theory. (Left) the actual sandstone sample placed into a beaker with brine solution at the base. (Right) graphical representation of the electrode setup on the sandstone sample.	39
Figure 2.2	Resistivity measurements for an atmospheric sandstone sample with its base submerged in an 18wt.% NaCl solution. The two probe resistivity measurements were taken using the base electrode (0) as a reference to the other electrodes along the length of the sample.	40
Figure 2.3	Temperature controlled testing cabinet layout used in the UNGI Laboratory at Colorado School of Mines. Two heating elements with circulation fans are controlled to maintain a constant temperature throughout the duration of the testing period Padin (2016).	43

Figure 2.4	(Left) assembled triaxial testing cell displaying the end caps and (right) disassembled triaxial testing cell showing the internal axial piston (Padin 2016).	45
Figure 2.5	Schematic representation of the large triaxial cell setup as pictured within the triaxial cell. The core (orange) is centered between two axial pistons. Sandwiching the core are two porous metal filters to disperse the pore fluids. Sandwiching the filters are two electrode plates used as source current for resistivity measurements.. . . .	46
Figure 2.6	Schematic design of the larger triaxial test systems valve and pump setup used in the osmotic pressure and resistivity tests. The location of the non-conductive hoses are highlighted in green and labeled NC hose. .	47
Figure 2.7	Resistivity measurements performed to determine the isolation of the core. Three separate setups were checked to determine any variance in the resistivity measurements from outside electrical sources.	49
Figure 2.8	Schematic figure of the pore pressure isolation system design and implemented into the triaxial cell as to prevent electrical circumvention of the core sample.	50
Figure 2.9	Disassembled small triaxial cell with pore pressure cap attachment. The end cap attachments are hard anodized as to prevent any electrical current from flowing through the liquid and into the cell chamber. This adds an additional level of electrical isolation to the core for accurate resistivity measurements.	51
Figure 2.10	(Left) Schematic design of the electrode setup for two probe resistivity measurements. (Right) actual electrode setup for two probe resistivity sample used in the pore pressure penetration tests. It should be noted that for the pore pressure tests a set of porous metal filters would sit between the electrode plates and physical sample.	52
Figure 2.11	(Left) four probe setup of a shale sample showing the two potential electrodes embedded into the sample. (Right) schematic of the imbedded potential electrode to show depth of embedment and orientation to bedding lines.	55
Figure 2.12	Triaxial resistivity calibration test performed on a Berea sandstone core sample with series resistivity vertical data and corresponding compressional velocity data. It is observed that as saturation increased through the core the resistivity decreased down to a lower limit. The P-wave velocity data agrees with the saturation as seen in the resistivity measurements.	59

Figure 3.1	Stress-strain curves (top) as well as stress-lateral/axial strain curves (bottom) for samples Eagle Ford samples #1, #2, #3, and #4 . Samples #3 and #4 were exposed to varying stress state conditions where as samples #1, #2, and #5 were at a single stress condition. . . .	68
Figure 3.2	Failure criteria of samples #3 (top) and #4 (bottom) determined through the use of Mohr's circle. Various plugs at the same depths were tested at varying confining pressure for the parameters required to use for Mohr's plots. From interpretation of the plots cohesion, friction angle, and ultimate compressive strength are determined.	70
Figure 3.3	Results from an Upper Eagle Ford sample for consolidation and permeability measurements. Simultaneous measurements of pore pressure at the top of the sample (downstream pore pressure), circulation pressure (upstream pressure), axial displacement (vertical strain perpendicular to bedding), confining stress, effective stress, temperature, and wave velocities (Padin 2016).	73
Figure 3.4	Dependence of pulse-decay determined permeability on effective stress of the sample. It is observed that the permeability decreases with increasing effective stress in a power function trend. Also, the sharp decrease between 1,000 psi to 1,500 psi represents the closure of microfractures.	76
Figure 3.5	Calculation of the Klinkenberg gas slippage factor (b) from the plot of the measured permeability from multiple pore pressures and the inverse of those pore pressures. The Y-intercept is representative of (k_{∞}) and the slope is equal to ($b * k_{\infty}$)	77
Figure 3.6	Results of the Upper Eagle Ford steady-state nitrogen permeability measurements at increasing effective stresses.	78
Figure 3.7	Continuation of the results for the Upper Eagle Ford steady-state nitrogen permeability measurements at increasing effective stresses. . . .	79
Figure 3.8	Dependence of steady-state determined permeability on effective stress of the sample.	80
Figure 3.9	Comparison of the two methods of measuring permeability, pulse-decay and steady-state with increasing effective stress. There is minimal difference observed between the two methods of measurement, though it is concluded for an efficiency standpoint it is more effective to perform pulse-decay permeability measurements.	81

Figure 3.10	Results for resistivity measurements during pore pressure penetration on an Eagle Ford shale sample. Observed is the initial drop in resistivity due to the saturation of a 60,000 ppm KCl solution, then an increase in resistivity due to consolidation and injection of a 1,000 ppm KCl solution for the osmosis tests. Also, the corresponding P-wave velocity data is shown to increase with saturation as well as consolidation.	83
Figure 3.11	An observed increase in resistivity due to the increased effective stress state on the Eagle Ford shale sample, and a second increase in resistivity due to the introduction of a lower salinity fluid at the initiation of the osmotic pressure tests.	85
Figure 3.12	Measured resistivity as a function of effective stress in an Eagle Ford preserved shale core sample. A linear trend showing the increase of resistivity with increasing stress is displayed.	86
Figure 3.13	Compressional velocity as a function of effective stress in Eagle Ford preserved shale core sample measured in this study. The increased velocity reaches a plateau at 1,000 psi effective stress where in comparison to the resistivity data, the resistivity maintains a positive upward slope which signifies additional changes in the rock structure passed the effectiveness of the P-wave velocity measurements.	87
Figure 3.14	Stress dependency of permeability measurements of Eagle Ford shale sample. As the effective stress increases, this represents closure of the pore throats decreasing permeability of the rock	88
Figure 3.15	Relation between permeability and resistivity. As the permeability of the rock decreases due to closure of natural fractures, nano-pores and constriction of pore throats the resistivity also decreases from the reduction of the pore geometry.	88
Figure 3.16	Osmosis experiment with low salinity (1,000ppm) NaCL brine solution. At day 33 the top side pore pressure passed the base pore pressure and gradually increased and reached a peak of an additional 500psi of pore pressure at the top of the sample.	91
Figure 3.17	Correcting measured resistivity for effective stress due to the increase in pore pressure from osmosis shows a decrease in the actual resistivity of the rock if osmosis had not occurred. Also observed is a difference between the model and the measured resistivity at point which pore pressure passes the original 4,000 psi. This shows that there is a reaction time for the rock, that the deformation of the pore geometry is not instantaneous, rather slowly occurring.	92

Figure 4.1	Formation Factor (F_r) throughout the saturation period. It is observed that (F_r) decreases with the time of which the sample is exposed to 18 wt.% NaCl solution. Also displayed is the P-wave velocity data recorded throughout the saturation which is seen to increase with decreasing formation factor.	95
Figure 4.2	Comparison of water saturation calculation using Archie's Method and the method of Electrical Efficiency as presented by Herrick and Kennedy, (1993). As it is observed there is a strong difference in the calculated water saturation between the two methods.	96
Figure 4.3	Resistivity of varying brine concentrations. A power function relates the two resistivity of the varying concentrations of NaCl which is then used to determine the brine concentration from the measured total resistivity during triaxial tests.	97
Figure 4.4	Results from the model showing the concentration of NaCl brine moving through the core in comparison to the calculated concentration due to measured resistivity. It is seen that the electrodes 0 and 1 show a strong relation with the model, where as the results for 1-2 and 2-3 vary from the models prediction.	101
Figure 4.5	Results of the Eagle Ford shale resistivity osmosis test show that the upper electrodes 3 and 4 show much greater resistivity in comparison to the lower electrodes 1 and 2 which show much lower resistivity results. This could be due to salt precipitation within the pore space, increasing the volume of conductive minerals, thus decreasing the resistivity. . . .	104
Figure 4.6	FE-SEM images showing the precipitation of salt taken after the completion of pore pressure penetration tests. (A) NaCl precipitation throughout a continuous fracture. (B) precipitation of NaCl in open spaces of an intermittent fracture. (C) and (D) other examples of NaCl precipitation (Padin 2016).	105
Figure A.1	(A) The Sartorius Precision Balance with an error ± 0.001 grams. (B, C, D) Images showing stages of the Dean-Stark cleaning process (Padin 2016).	120
Figure A.2	The bulk density measurement setup within the mercury lab at CSM with an error of ± 0.1 cc. (A) A general view of the machine. (B) The calibrated mercury volume chamber. (C) The sample chamber calibration point (Padin 2016).	121

Figure A.3	(A) Preserved 1-foot core sample (B) A vertical and horizontal fracture which are common throughout the cores and must be avoided (C) A vertical fracture which propagated while trying to create parallel edges (Padin 2016).	125
Figure A.4	Example of the core being drilled and plugs taken. (A) A core being held in place for a plug to be drilled. (B) A diamond tipped drill. (C) A preserved core sample. (D) A drilled core sample (Padin 2016). . . .	126
Figure A.5	(A) A dilled plug from a core. (B) Cutting the core to length. (C) Using a lathe to ensure the edges are perfectly parallel. (D) A finished core sample ready for the resistivity measurements to be applied (Padin 2016).	127
Figure A.6	Designed and actual electrode setup for two probe resistivity sample used in the pore pressure penetration tests.	128
Figure A.7	(A) Sandstone sample with blue taped to mark off the location for the conductive epoxy. (B) Conductive epoxy applied to the sample. (C) Conductive epoxy applied and tapped removed from the sandstone sample. (D) A shale sample with the epoxy applied and wire connected for readings.	130
Figure A.8	Four probe setup of a shale sample showing the two potential electrodes embedded into the sample (left), schematic of the imbedded potential electrode o show depth of embedment and orientation to bedding lines (right).	131
Figure A.9	(A) Sandstone sample with electrodes and sandwiching electrode plates. It should be noted that the porous metal filters go between the electrode plates and the sample. (B) A shale sample with electrodes and wires attached. (C) The axial piston setup and wires connected to the electrical outputs. (D) The entire setup with epoxy sealant to ensure no leakage (Padin 2016).	134
Figure B.1	Solidworks 3D cross section of the triaxial cell with the main components labeled (Padin 2016).	136
Figure B.2	(A) Internal piston of the triaxial cell which creates the chamber for axial stress and the area where the confining pressure is applied. (B) The main confining chamber which the sample is placed into (Padin 2016).	137

Figure B.3	A graphical representation of the test setup, (A) Is the testing cell, (B and C) are the pore pressure pumps, (D) are the hydraulic pumps and (F) is the electrical pump control units (Padin 2016).	139
Figure B.4	Schematic representation of the pipe system to control the flow of fluids for the triaxial cell.	140
Figure B.5	Connection of non conductive hoses to the triaxial cell confining and axial pressure ports (Padin 2016).	141
Figure B.6	Schematic of the forces applied and the variables required to determine the stress exhibited on the rock sample (Padin 2016).	142
Figure B.7	ISCO Syringe Pump specification sheet.	144
Figure B.8	(A) The interface control of the syringe pumps with labeled readings. (B) The interface control of the LVDT with labeled readings (Padin 2016).	145
Figure B.9	Computer interface of sonic measurements with labeled readings (Padin 2016).	146
Figure B.10	(A) Pressure transducer used in coordination with the syringe pumps. (B) Pressure transducer used for the DPT (Padin 2016).	147
Figure B.11	(A) mounting the LVDT to the top axial piston. (B) The extensometer portion of the LVDT. (C) The digital readout and connection to the data acquisition system. (D) Aan aluminum plug used for calibration (Padin 2016).	149
Figure B.12	(A) The temperature control system with interface to set the desired temperatures. (B) The heating element with fins and the fans used to circulate the air throughout the cabinet. (C) The fuse which if the heating element over heats will break the electrical source to shut off the heating element (Padin 2016).	150
Figure B.13	Diagram of the location of the heating system and the circulation of the air within the temperature controlled cabinet.	151
Figure B.14	(A) The endcap of the axial piston which can be removed to attach a transducer. (B) The transducer located within the piston. (C) The pulser/receiver and RF witches for changing between P and S waves measurements (Padin 2016).	152

LIST OF TABLES

Table 3.1	Set of cored samples available for experimental use from the Eagle Ford, Vaca Muerta, Bakken, and Pierre shale formations.	63
Table 3.2	Bulk density of Eagle Ford Shale samples utilizing the mercury bulk density method.	64
Table 3.3	Results of XRD grain density and pycnometer grain density methods with displayed difference between the two methods.	65
Table 3.4	Absolute porosity calculation utilizing both methods of grain density calculation.	65
Table 3.5	Results from geomechanical determination: Static Young's modulus, Poisson's Ratio and Compressive Strength. Samples 3 and 4 enabled the calculation of the failure envelope using Mohr's Circle due to the varying stress conditions.	69
Table 3.6	Dynamic measurements taken simultaneously throughout triaxial stress strain tests.	71
Table 3.7	Extension of Table 3.6 displaying the results for the modulus determinations.	71
Table 3.8	Results of the Upper Eagle Ford pulse-decay nitrogen permeability for varying effective stresses.	75
Table 3.9	Comparison of the directional dependent gas permeability results at an effective stress of 1,500 psi for the steady-state method of measurements. It is observed that varying results are obtained dependent on the upstream and downstream flow of gas.	82
Table B.1	Required pump pressures for the pressure step ups while maintaining constant effective stress.	143

LIST OF SYMBOLS

absorption coefficient	α_c
Area	A
Archie's tortuosity exponent	a
Area of internal confining chamber	A_C
Area of sample	A_S
Electrical efficiency empirical constant	a_t
Electrical efficiency empirical constant	b_t
Compressibility of the downstream reservoir	c_d
Formation conductivity	C_o
Matrix solute concentration	$c_{s,m}$
Total compressibility in matrix	$c_{t,m}$
Compressibility of the upstream reservoir	c_u
Fluid conductivity	C_w
Depth	D
Bulk diffusivity coefficient	D^{eff}
Bulk diffusivity coefficient in fracture	D_f
Diffusivity coefficient in free solution	D_o
Electrical efficiency	E
Potential difference	E_c
Electrical geometric factor	E_o

Resistivity factor	F
Internal geometry factor for porous media	f_G
Formation resistivity	F_o
Resistivity index	I
Permeability	k
Matrix permeability	k_m
Thermal conductivity of water	K_w
Sample length	L
Tortuous travel length	L'
Ion mobility ratio	M
Archie's cementation exponent	m
Mass of the dry pycnometer at the desired temperature	M_p
Mass of the pycnometer at the desired temperature	$M_{pw,c}$
Rate of momentum exchange between rock matrix and water	$\dot{\mathbf{m}}_{sw}$
Rate of momentum exchange between water and rock matrix	$\dot{\mathbf{m}}_{ws}$
Archie's wettability exponent	n
Confining pressure	P_c
Axial pressure	P_a
Pore pressure	P_p
Flow rate	q
Matrix specific water rate	\hat{q}_{wm}
Pore specific water rate	\hat{q}_{wp}
Resistivity	R

Universal gas constant	R_{avg}
Macroscopic bulk resistivity horizontal component	R_h
Macroporous resistivity	R_M
Measured resistivity	R_s
Shale resistivity horizontal tensor component	R_{shale_h}
Shale resistivity vertical tensor component	R_{shale_v}
Total resistivity	R_T
Macroscopic bulk resistivity vertical component	R_v
Fluid resistivity	R_w
Perpendicular resistivity	R_{\perp}
Parallel resistivity	R_{\parallel}
Microporous Resistivity	R_{μ}
Water saturation	S_w
Water saturation in rock matrix	$S_{w,m}$
Water saturation in pore	S_{wp}
Temperature	T
Time	t
Tortuous travel time	t'
Temperature of rock matrix	T_m
Displacement in x, y, and z direction	u_x, u_y, u_z
Macroporous volume fraction	V_M
Pycnometer volume	V_p
Rock volume	V_R

Partial volume of solute	V_s
Relative volume of the conductive component	V_{sh}
Partial volume of water	V_w
Microporous volume fraction	V_μ
Impedance	Z
Compressibility factor	z
Wire impedance	Z_p
Biot's coefficient	α
Pressure Decay Slope	α_{hr}
Grid block dimension	$\Delta x, \Delta y, \Delta z$
Dielectric constant	ϵ
Elastic strain tensor	ϵ_e
Tortuosity	τ
Time step	Δt
Time step for mass transport equation	Δt_m
Oil density	ρ_o
Water density	ρ_w
Bulk density	ρ_{bulk}
Solid grains density	ρ_{solids}
Effective stress	σ_{eff}
Macroscopic bulk conductivity horizontal component	σ_h
Conductivity of conductive component	σ_{sh}
Conductivity of resistive component	σ_{sd}

Macroscopic bulk conductivity vertical component	σ_v
Porosity	ϕ
Matrix porosity	ϕ_m
Anisotropic coefficient	λ
Interfacial tension	γ
Water specific gravity	γ_w
Viscosity	μ
Viscosity of oil	μ_o
Viscosity of water	μ_w
Chemical potential of component i	μ_i
Ratio of sample areas	ψ
Osmotic efficient coefficient or membrane efficient coefficient or reflection coefficient . .	ω

LIST OF ABBREVIATIONS

Computer Tomography	CT
Differential Pressure Transducer	DPT
Volumetric Mineralogy	EDAX
Electrical Efficiency Theory	EET
Gamma Ray	GR
Grams per Cubic Centimeter	g/cc
Linear Variable Differential Transformer	LVDT
Logging While Drilling	LWD
Measure While Drilling	MWD
Nanometers	nm
Parts Per Million	PPM
Society of Automotive Engineers	SAE
Scanning Electron Microscope	SEM
Spontaneous Potential	SP
Total Organic Carbon	TOC
Ultimate Compressive Strength	UCS
Unconventional Natural Gas and Oil Institute	UGNI
Weight	wt.
X-Ray Diffraction	XRD

ACKNOWLEDGMENTS

The work displayed in my thesis is not the product of my individual performance, but the result of collaboration within the research team I have worked with and the support of others around me for the past two years. For this, I have to extend my gratitude.

My greatest gratitude is for my advisor at Colorado School of Mines, Dr. Azra N. Tutuncu. Her continuous support and guidance throughout my career at Mines has been critical to my success as a research student. Gaining knowledge from her Geomechanics Courses as well as the research and laboratory skills from my work as a researcher have greatly added to my knowledge and problem solving abilities as an engineer.

I would also like to express my gratitude for the contributions of the other members of my thesis committee: Dr. Erdal Ozkan, Dr. Linda Battalora, and Dr. Daisuke Katsuki.

Special thanks has to go to my research partners in the lab whom I spent many hours and countless long nights working with. Dr. Daisuke Katsuki was instrumental in the success of our experimental setup. We bounced ideas off each other and after several iterations, we developed a resistivity measurement system which was implemented into existing triaxial cells. His continuous help and guidance, as well as his humor, made our lab work not only successful, but also fun. I also worked closely with Dr. Anton Padin and his chemical osmosis research. Together, we successfully collaborated on numerous tasks to complete UNGI reports and presentations, and working through the night collecting data for our measurements.

My parents, John and Barbara have shown constant support and encouragement throughout not only my graduate school, but any and all of my adventures in life; I have been successful because of them. For their never wavering support, I dedicate my thesis to my parents.

In addition, I would like to express my gratitude to the people and companies who sponsor the Unconventional Natural Gas and Oil Institute (UNGI) research group and made my academic career financially possible. The monetary support of the UNGI CIMMM Consortium at Colorado School of Mines made it possible for meaningful research to be produced and improve our knowledge. For my specific work I have to show my gratitude to Dr. Ali I. Mese who donated the high-pressure triaxial cell utilized in this work. Without it, this work would not have been possible and for that I am very grateful to provide our group with such necessary and unparalleled tools to complete our research studies.

Finally, I would like to thank my friends at Mines who have supported me throughout this process. Volunteering as a coach with the Mines Javelin throwers and Wrestling team gave me mental breaks throughout my studies to refresh myself. Without these activities and the experiences, I would be still working on my research with not much success. Thank you to Jeff and Jorge on the track team, as well as Paul on the wrestling team.

Dedicated to my Parents, John and Barbara for their constant support for me throughout
my life's endeavors.

CHAPTER 1

PROJECT DESCRIPTION

The purpose of this chapter is to provide an explanation for the significance of this research study and to give a brief description of the theory and use of the resistivity measurements in laboratory and in the field environment.

1.1 Statement of Problem and Significance

Resistivity measurements are typically used to characterize hydrocarbon bearing reservoirs and have been extensively studied since their introduction in the first experimental surface resistivity measurements conducted in 1911, as performed by Conrad Schlumberger (Schlumberger et al. 1934). One of the first major contributions to the understanding of the electrical properties of reservoirs came from Archie (1942) in his theoretical study relating the saturation of clean sandstone rocks to the electrical resistivity of the rock and saturating brine solution. Archie's equation, as it has come to be known, has been accepted by the energy industry to interpret not only clean Archie sandstone rocks, but also has been adapted to examine other sedimentary formations. Recent experimental studies have shown that Archie's equation is not an accurate representation of the electrical property dependence to fluid saturation in all porous formations (Herrick et al. 2001; Kennedy 2006; Kennedy and Herrick 2012; Mahmood et al. 1991; Moran and Gianzero 1979; Suman and Knight 1997).

Due to the recent shale boom in the United States and throughout the world, characterization and economic viability of these unconventional hydrocarbon bearing reservoirs including shale gas, tight oil, carbonates, and unconsolidated sand formations have become an area of interest. Key to determining the viability of a hydrocarbon bearing reservoir is determining how much oil and gas is stored in the porous rock, and how expensive it would be to extract the hydrocarbons. Application of Archie's equation in these formations to aid in determining hydrocarbon volumes is not accurate and would result in significant error when

utilizing electrical resistivity logs (Worthington 1982). Also, other properties correlated to resistivity measurements would be incorrectly interpreted.

Conductive mineralogy, low permeability complex pore structures, in situ stress state, and anisotropy are the leading causes of erroneous interpretation of resistivity (Clavaud 2008; Clavier et al. 1984; Dobrynin 1962; Herrick and Kennedy 1993; Herrick et al. 2001; Klein 1996; Moran and Gianzero 1979; Patnode and Wyllie 1950; Schlumberger et al. 1934; Suman and Knight 1997; Winsauer et al. 1952; Woodruff et al. 2014; Wyble 1958; Wyllie and Rose 1950). Other variables affect resistivity and are covered in this work. Mineralogy becomes influential due to the dipping geologic beds which intersect the wellbore; also due to the recent advent of horizontal drilling and logging. The deposition of clay particles being flat in nature make conduction occur horizontally, or parallel to the bedding. When a resistivity logging tool reads at an angle to the bedding, the response or measured resistivity is not accurate to the true resistivity of the formation (Bittar and Rodney 1996) and will cause increased resistivity. These affects must be accounted for during log interpretation for accurate results and interpretation of the collected data.

The effects of pore geometry and rock stress state are related, because the pore geometry is dependent on the stress state of the rock. It has been shown that constrictions in the connectivity of the porous rock matrix influences the measured resistivity of saturated rocks. It has been observed in experimental work that as the stress state on the rock increases, representative of a decrease in the connectivity, an increase in resistivity is also observed (Brace et al. 1965; Dobrynin 1962; Winsauer et al. 1952). Archie's equation accounts for the pore geometry and other factors affecting the electrical properties of the rock through the use of empirically derived exponents (a), (m), and (n) representing tortuosity, cementation, and wettability. It has been proven by many researchers that these Archie exponents are not accurately accounted for or measured in many cases (Herrick 1988).

Anisotropy is most applicable in shale reservoirs, and other unconventional reservoirs. There are two causes of anisotropy, microanisotropy and macroanisotropy. Microanisotropy

is due to differing pore geometries and channels in various directions, being prevalent in shale formations. Macroanisotropy is a bulk property representative of the alternating conductive-resistive bedding layers. Due to the resolution of the current logging tools, the alternating layers are inadvertently grouped together by the logging tool producing an observed average over the differing layers. These layers are commonly observed in sand-shale sequences (Bittar and Rodney, 1996).

The results of an experimental investigation on the electrical impedance spectroscopy for both Archie and non-Archie formations have been presented in this research study. The core of this research is on examination for the effects of in situ stress state, pore geometry changes, tracking of the fluid migration, and rock-fluid interactions on the electrical properties of both Archie and non-Archie formations. Specifically Berea Sandstone, Eagle Ford Shale, and Pierre Shale were studied in detail. The industry standard Archie's equation for water saturation was compared to the equation proposed by Herrick (1988) that utilizes a geometric factor (E_o) to represent tortuosity, cementation, and wettability.

To complete this study, a resistivity measurement system has been designed and implemented into a triaxial cell. The core samples used and the pore fluid injection system in the experiments had to be electrically isolated to obtain accurate electrical measurements for our study. A detailed explanation of the electrical isolation has been included in the thesis due to the importance for such a system to achieve the accurate results in the experiments. The study performed utilized two different pore fluid injection systems within the triaxial cell which is explained in greater detail further in the thesis. Results from the two systems show potential sources of error for laboratory resistivity setup from the electrical shortcuts. A literature review for resistivity measurements using triaxial systems presented minimal documentation of such experimental setup, and the equipment used were not clearly detailed as to how the rock and pore fluid system were electrically isolated. This unknown casts a shadow on the complete electrical isolation, which would affect the measured data reported in the associated publications.

The resistivity measurements have been coupled with geomechanical deformation, compressional and shear wave velocities, absolute permeability, and XRD scans of the specific samples. These parameters were recorded as a function of in situ stress state, elevated pore pressure, and fluid composition to create a database of the affected properties. The collection of the large array of the coupled data provides valuable insight on the interdependence of the measured properties. Such work has not yet been completed for shale samples in this research study due to the complexities of the testing apparatus and longevity of the tests to be performed on particular shale reservoir core samples.

The resistivity measurements performed have been coupled with the work of Dr. Anton Padin (2016), where water and solute transport mechanisms in organic-rich carbonate mudrocks have been experimentally examined. The overall goal for the two studies is to find fracturing fluids that do not use harmful chemicals and that also improve hydrocarbon recovery factors. One potential alternative investigated in both studies was on how various salt types and concentrations form or affect osmotic pressures created by the opposing salt concentrations which can be utilized to lead an easier fracturing of the shale formations (Mese 2008). Also, the osmosis process can be used for improving oil production in shale formations. The osmotic pressure gradient has the potential to enhance the displacement of oil from the matrix pores (Fakcharoenphol et al. 2014).

One key experimental observation for better understanding of the osmotic pressure comes from better understanding on how the fluid migrates in the pore space and affects the local saturation of the core when low-salinity fluids are injected. It is observed that resistivity measurements during pore pressure penetration tests aid in the interpretation of the fluid-rock interactions taking place between the shale core samples and the various concentration brine solutions tested. Laboratory resistivity measurements enable us to correlate the measured resistivity, osmotic pressure created, strain, compressional and shear wave velocities, changes in porosity, and permeability in the formation.

The goal for the resistivity measurements presented in this research study is to detect the local brine concentration variations and to determine how the brine solution is imbibed through a core sample due to the osmotic pressure changes and associated effective stress changes introduced during the laboratory measurements. The influence of the rock's in situ stress state on pore throat geometry and concurrent changes in resistivity values measured have been investigated aiding in explanation of the modified Archie's equations for the geometric factor (E_o) as theoretically shown by Kennedy and Herick (1993). A closer examination into the cementation and saturation exponents show that the resistivity is strongly influenced by the pore geometry. The proposed equation by Kennedy and Herick and the geometric factor is intended to replace Archie's equation and the Archie exponents with a coefficient representing the matrix influence on the resistivity. During the osmosis tests, the effective stress is increased during the consolidation stage and then decreased due to the increase in pore pressure from the effects of the osmosis.

1.2 Introduction and Background to Resistivity Measurements

Resistivity or conductivity measurements (conductivity being the reciprocal of the resistivity) are utilized in many industries ranging from medical testing to determine bone fracture locations (Gupta et al. 2013), industrial manufacturing quality control and testing, and for geophysical prospecting of hydrocarbon bearing formations. Specific to the energy industry, resistivity measurements are used extensively and are a measure of the ability for electrical current to flow through the porous media. It is understood that the physical rock matrix is nonconductive, however due to the complex open pore structure which flows throughout the rock media, when saturated with conductive liquid enables electrical current to flow.

The interstitial or connate brine solution contained in the pores of the rock media also include dissolved salts. When these salts dissociate into positively charged cations and negatively charged anions, the ions will move under the influence of an electrical field and carry an electrical current through the solution. The electrical resistivity is then a measure

of the fluid-saturated media to impede the flow of electrical current. Resistivity is expressed in ohm-meters ($\Omega\text{-m}$).

The measured resistance to electrical current of the brine filled media aids in the physical characterization of the rock and quality of the reservoir. Electrical resistivity measurements have been used to correlate or calculate water saturation, hydrocarbon saturation, porosity, permeability, and formation consolidation. The simplest correlation using electrical resistivity is that a decrease in the measured resistivity comes from an increased porosity, and that an increase in resistivity comes from an increase in hydrocarbon volumes as hydrocarbons are a barrier to electrical current. Electrical resistivity may represent clear correlations between various reservoir properties; however, the electrical properties of a porous media are dependent on many factors, including: pore geometry, formation stress, wettability, composition of rock, anisotropy, salinity of connate fluid, and formation temperature which quickly complicate the interpretation of the measured resistivity.

One of the first major contributions to the energy industry to characterize the electrical properties of the rock formations came from Conrad Schlumberger who performed the first resistivity logging operation on a vertical wellbore in 1911, (Schlumberger et al. 1934). Schlumberger observed the increase in resistance to electrical flow with the presence of hydrocarbons. The next major knowledge jump in resistivity came from Archie (1942) who related the saturation of clean sandstone to the electrical resistivity of the rock and saturating brine solution. Archie's equation, as it has come to be known, has been accepted by the energy industry to interpret not only clean Archie rocks, but also adapted to examine non-Archie rocks.

Archie (1942) classified the relation between the formation resistivity and the connate water resistivity to be termed as the formation factor (F_R). The formation factor numerically characterizes the geometric effects on the electrical properties of the rock due to tortuosity of the pore channels, also relating the porosity to (F_R) (Worthington 1982). Further work performed by Patnode and Wyllie (1950) discovered that the formation factor is not constant

for a particular reservoir; but, the formation factor will change due to the resistivity of the saturating fluid. This change in the resistivity has been attributed to the presence of shales in the formation as well.

Furthering Archie's work, correlations between the formation factor, porosity, tortuosity, and cementation are also well documented. The simplest method of modeling porous media is a system of straight capillary tubes. As the number of tubes increase, representing an increase in porosity, the resistivity decreases. This inverse relation between porosity and resistivity is due to the increased conductivity from a greater cross-sectional area of flow. As the complexity of the path for the capillary tubes increase, the resistivity increases. This is representative of the direct relationship between resistivity and tortuosity. As the flow path becomes more complex or tortuous, the resistivity increases due to the more complex pore geometries and the impedance of the electrical current.

Grain particle cementation has a direct relation with resistivity. The cementing materials include silica, calcium, carbonate, and various other clays. The amount of cementation depends on the type, amount, and deposition of the geologic formation. Less-cemented sandstones tend to exhibit higher porosity; thus, lower measured resistivity and decreased formation factor. Greater-cemented sandstone tends to decrease porosity, thus, increasing resistivity and increasing formation factor (Rine et al. 2010). Standard values of cementation factor have been determined for various rock types. For chalky rocks and compact formations, cementation factor is roughly equal to 2, for highly cemented rocks the value can rise to 3.

Implementing resistivity measurements in the UNGI triaxial measurement cell for pore pressure penetration tests aids in the understanding on the dependence of the electrically properties of the rock on effective stress, pore geometry, fluid-rock interaction, and anisotropy. The physics behind the resistivity measurements is to apply a known electrical current to a sample and measure the drop in voltage across the material, being the material's resistance. Resistivity is then calculated knowing the measured resistance, lengths between electrodes, and the cross-sectional area as displayed in Equation 1.1 where the measured resistance (R_s)

is multiplied by the ratio of area (A) of the core sample and length (L) between electrodes.

$$R = R_s \frac{A}{L} \quad (1.1)$$

There are two types of experimental lab based measurements in determining resistivity. These are two probe and four probe measurements. Two probe resistivity tests require minimal alteration of the current triaxial cell in comparison to the four probe measurement setup as discussed in Wang et al. (2009). Two probe resistivity measurements are comprised of two electrodes and a meter used to transmit a known current and measure the materials resistance to that applied current. The method is simple; yet, the two probe measurement setup suffers from an inherent disadvantage of contact resistance which occurs between the electrode and the material surface (Taylor and Barker 2002). Probe and contact resistance are unknowingly accounted for in two probe measurements in the material resistance, known as electrode impedance or polarization impedance. Mathematically, impedance (z) is calculated by the sum of the sample, electrode, and wire impedances (Z_p). If polarization impedance is minimized, then the core resistivity would be equal to the impedance, as displayed in Equation 1.2 (Wang et al. 2009). Minimizing or even better, elimination of the polarization impedance is essential for conducting accurate resistivity measurements.

$$z = R_s \frac{A}{L} + Z_p \quad (1.2)$$

Four probe resistivity measurements are comprised of two pairs of evenly spaced probes. Two electrode plates are used as a source current that sandwiches the core sample on either end, as labeled A and B in Figure 1.1, while another pair of electrodes, M and N, are embedded in the core and are used to measure the materials resistance. The main advantages of the four probe method are that it negates the probe resistance, spreading resistance under each probe, and contact resistance between the probe and material. Resistivity is calculated the same way as with the two probe measurement while the resistance is measured between the two electrodes M and N. Further work to isolate the sample and probes was performed to ensure there were no electrical shortcuts. Adaptations to the triaxial cells were performed

to completely electrically isolate the sample and are explained further in the report in great detail. Mahmood et al. (1991) showed experimental measurements comparing both two and four probe resistivity measurements and observed that the four probe method produced lower resistivity values; they accredited these lower values of four probe resistivity to the existence of the contact resistance prevalent in the two probe method.

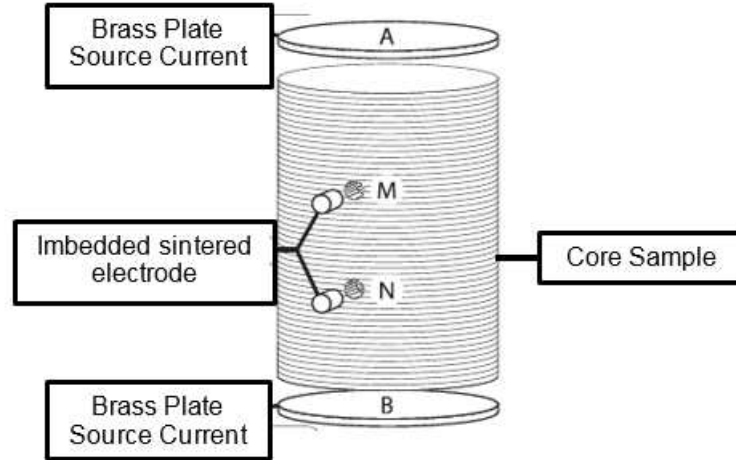


Figure 1.1: Four probe resistivity measurement setup for a cylindrical shale sample with horizontal bedding planes. Two source current electrodes sandwiched the core (A and B), while two embedded sintered electrodes are used to measure the current between the probes (Woodruff et al. 2014).

The material used for the probes has an effect on impedance and can skew results if not correctly accounted for. For the two probe measurements, silver conductive epoxy has been used to adhere copper wires which are installed circumferentially around the external surface of the core samples. Four probe measurements utilize silver-silver chloride sintered bare sensor electrode pellets supplied from In Vivo Metric. These pellet electrodes are homogenous silver-silver chloride with an embedded silver wire lead. The frequency which the resistivity measurements are taken also effects the impedance and is selected to be 1000 Hertz (Hz) due to the minimal effects on the impedance as shown in Figure 1.2 (Wang et al. 2009). As illustrated in the graph, the effect on the impedance is minimized for all electrode materials as the frequency increases, thus the use of 1000 Hz for this experimental work

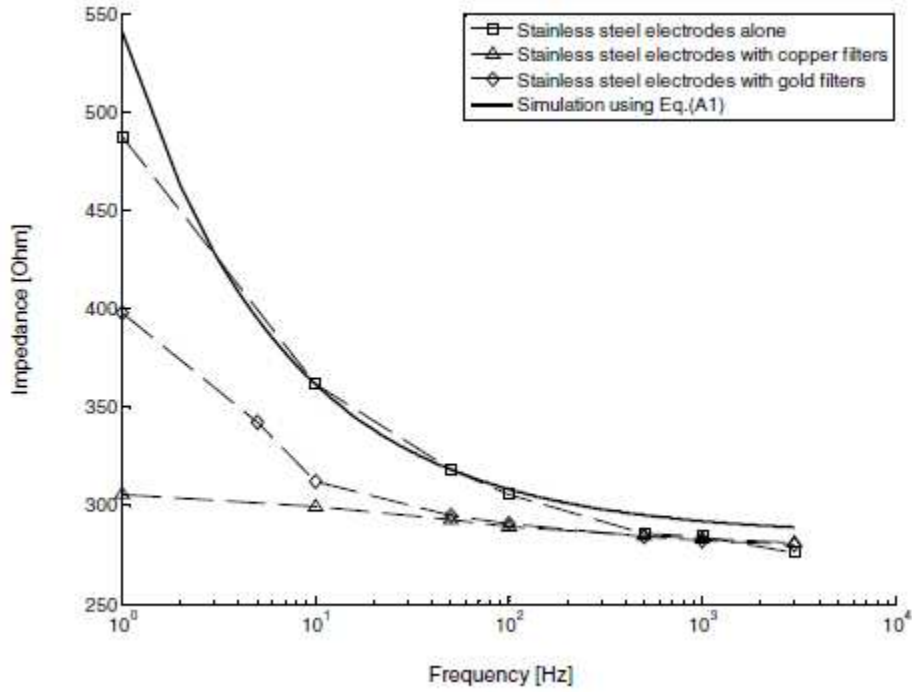


Figure 1.2: Measured impedance dependence on varying frequency for different electrode/filter material combinations (Wang et al. 2009). The selection to perform the resistivity measurements at 1000 Hz is made to negate the material effects on the resistivity.

provides accurate measurements.

To calibrate the triaxial cell resistivity measurements, atmospheric measurements have been performed on sandstone samples to show the probe setup and test the capability for the measurements to track the fluid migration. Two shale formations have been selected for the triaxial cell tests under in situ conditions. These are Eagle Ford and Pierre. Moreover a Berea Sandstone sample was also used for comparison. The shale types are selected due to availability of core samples as well as relevance to the UNGI CIMMM Consortium osmotic pressure investigation project. Resistivity has been initially measured using two probe method of measurement, and recently the experimental has be converted to the four probe method as described in this report.

The observed resistivity data from both the pore pressure penetration tests and the ambient pressure tests are compiled, an analysis of the resistivity data has been performed in

conjunction with the other properties which are simultaneously measured in the UNGI coupled experiments. Correlations between the resistivity and the osmotic pressure, strain, wave velocities, changes in the porosity, changes in the rock microstructure, and the permeability have been observed and can be implemented into the interpretation of the resistivity measurements obtained from the wireline log data in wells. Logging measurements are available for the Eagle Ford core samples tested in this study. An examination of the electrical log data for the section of the well which the core sample was taken is performed as to implement the findings of this research study with the log interpretation.

1.3 Literature Review

The purpose of this section is to examine past work into the topic of resistivity measurements and its influence on estimating the reservoir properties such as porosity, water saturation, formation factor, and other parameters. An in depth look at the physical characteristics of varying rock types and how these parameters affect resistivity has been performed. First, an examination of Archie's equation (1942) was conducted looking at the effects of tortuosity and pore throat geometry.

Oil reservoirs are deposited in a multitude of environments at varying rates, altering the porosity and pore geometric structure of the reservoir rocks. The pore fluid distribution has been noted as one of the key factors affecting the electrical properties of the rocks (Dobrynin 1962; Herrick and Kennedy 1993; Klein et al. 1997; Longeron et al. 1989; Sharma et al. 1991; Woodruff et al. 2014; Wyllie and Rose 1950). Also, wettability has been determined to be strongly influential on the value of Archie's saturation exponent (n). The saturation exponent dependence is high if the core is oil-wet or water-wet, between drainage or imbibition cycles, and strong dependence also exists on the stress state of the rock (Dobrynin 1962; Herrick and Kennedy 1993; Sharma et al. 1991).

Resistivity measurements have been predominately used to determine water saturation in oil bearing reservoirs; however, the origins of the resistivity-water saturation relation are not accurate. In the current research study, the original Archie relationships which used

graphically derived exponents was investigated to adjust the relationship to be linear on log-log plots, and introduced new factors which account for electrical efficiency of the rock, being a geometric factor representative of the rocks specific pore structure and properties. Through experimental work, it has been shown that the original parameters of the Archie's law utilizing factors for saturation, tortuosity, and cementation were not incorporated into the relationship accurately. In this section, a review of these parameters is conducted to determine why they have not been applied accurately. The results presented in this study has provided corrections on these factors and have introduced a new, mathematically determined electrical efficiency which accounts for the changing electrical parameters.

1.3.1 Measurements of Resistivity Dependence on Pore Throat Geometry

There are a number of experimental results published in the literature showing correlations between resistivity and saturation of rocks. Archie (1942) was the first to make a correlation between the formation resistivity and the water resistivity in clean sandstone formations. This correlation evolved and became to be known as Archie's equation for water saturation as represented by Equation 1.3, accounting for tortuosity (a), cementation (m), and saturation (n) with the associated exponents. If all variables remain constant besides the formation or true resistivity (R_t), then as water fills the rock pore space, conductivity increases due to increased water saturation (S_w), consequently decreasing true resistivity (Archie 1942). The simplified relationship for clean sandstones supports the theory of using resistivity measurements to track fluid flow over time as the resistivity can be used to determine the saturation and potentially the location of the fluid front from the observed decreases in the resistivity being correlated to the salt concentration of the brine solution.

$$S_w = \left(\frac{a * R_w}{R_t * \phi^m} \right)^{\frac{1}{n}} \quad (1.3)$$

There are concerns with the accuracy of Archie's equation as the exponents related to the rocks porosity, (a), (n) and (m) are derived from graphical analysis, manipulating the base equation to try and fit the experimental data. Patnode and Wyllie (1950) showed

that the calculated formation factor is less than the true formation factor when conductive solids are present within the cores tested. Further work was performed by Winsauer et al. (1952) who studied how tortuosity and porosity determine the resistivity factor and found out that the Archie model did not fit their data. Tortuosity (τ) is a ratio of the length of the tube which flow occurs to the length of the of the sample. Due to the complexities of the flow path in porous media, the length of the capillary tubes are not quite equivalent to the length of the flow path and the flow path can be much longer than the physical length of the sample. Tortuosity is mathematically related to the formation resistivity factor and porosity, as presented in Equation 1.4. Resistivity factor relates the formation resistivity with the fluid resistivity, Equation (1.5)(Archie 1942).

$$\tau^2 = F\phi \quad (1.4)$$

$$F = \frac{R_o}{R_w} = \frac{C_w}{C_o} \quad (1.5)$$

Winsauer et al. (1952) observed that the ratio of formation resistivity and fluid resistivity, the resistivity factor, is not an accurate relation if previous assumptions were made that the pore geometry does not change and that there would be no rock-fluid interactions. Due to the complexities of the rock pore structure it is very hard to predict or state that an electrical current will flow the exact same path everytime, for varying rocks within the same reservoir. Though, physics implies that an ion will travel the shortest path; the complex rock structure is not constant throughout a reservoir and varying results will be obtained. Within the larger voids of the pore space and restrictions at the pore throats there are many lines of travel which produce an almost infinite possible path lengths. As presented in Figure 1.3, six paths for current to flow are displayed within the same pore space where a number of other paths could also occur. It is well understood that an ion will travel the shortest distance; however, Figure 1.3 is meant to display how the connectivity complexities can alter greatly between the cores within the same reservoir. Displaying the tortuosity as a singular number is not an accurate assumption, because the path of current can travel a different route each time,

changing the tortuous length. If the path through the porous media were a singular, uniform straight tube, then a singular value for both tortuosity and resistivity would be acceptable. However, due to the complexity explained above concerning the pore space of a media, other variables must be accounted for to determine an accurate resistivity factor.

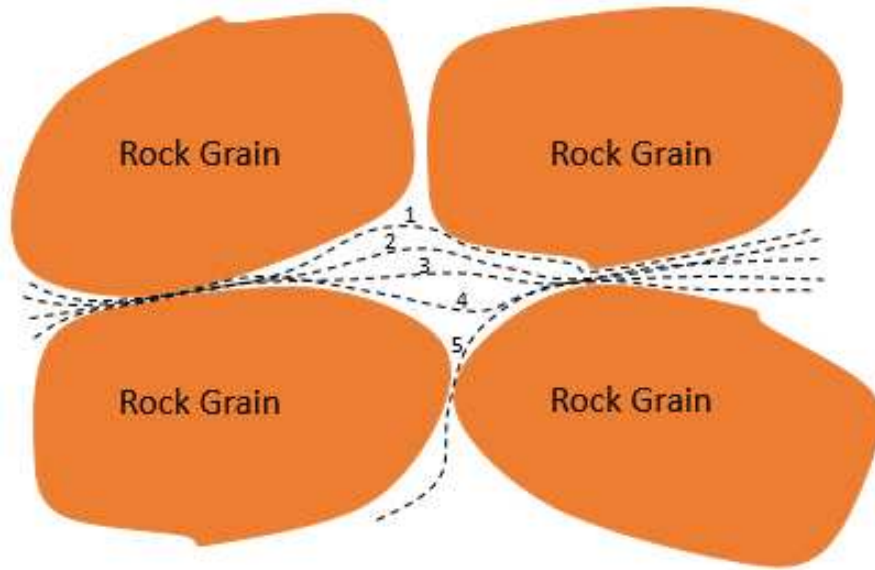


Figure 1.3: Complexities of connectivity and how it affects the path of ion flow through porous media, an infinite number of paths are possible due to the complex and ever changing pore structure throughout a reservoir. Furthermore, due to rock-fluid interactions and depletion from production the geometric structure of a specific section of rock could continuously change over time.

A more accurate determination of the tortuosity can be made as it is possible to measure the distance traveled by an ion determining the transit time of the ions traveling through the porous media. The length traveled in an uniform tube by the ion where (M) is the ionic mobility, $\frac{E_c}{l}$ is the potential gradient, and (t) is time is presented in Equation 1.6. If the ion travels through a tortuous media, then the equation is slightly adjusted as expressed in Equation 1.7 where the lengths represent the tortuous lengths (L') and the corresponding tortuous travel time (t'). The travel time varies for a straight line tube and a tortuous media for three reasons. First, simply because the travel length is longer; second, the potential gradient which transports the ion is less, though almost constant for shorter lengths (Kennedy

and Herrick 2012) and third, it is dependent on the particle size of the ion. Differing salt types, for example sodium chloride versus potassium chloride have differently sized ions that would travel at different rates. Assuming that the mobility ratio (M) and potential difference (E_c) are constant, if the test is run under the same conditions for a straight tube and a tortuous path, the two equations can be set equal to each other, as shown in Equation 1.8. Furthering the math, tortuosity can be solved for as the effective tortuous length over the straight tube length, as illustrated in Equation 1.9, producing a relation of tortuosity to the ion travel time. This produces a measurement of tortuosity directly related to ion travel time through the tortuous media which is directly related to the connectivity of the pore space within the rock matrix.

$$L = M \frac{E_c}{L} t \quad (1.6)$$

$$L' = M \frac{E_c}{L'} t' \quad (1.7)$$

$$\frac{L'^2}{t'} = M E_c = \frac{L^2}{t} \quad (1.8)$$

$$\sqrt{\frac{L'^2}{L^2}} = \tau = \sqrt{\frac{t'}{t}} \quad (1.9)$$

To alter or correct the resistivity factor in the original equation for resistivity, Equation 1.1 must be referred to. Combining the resistivity equation with formation resistivity factor in Equation 1.5, creates a relation of the straight line and tortuous paths to the ratio of the sample areas, as represented in Equation 1.10. The numerator is tortuosity (τ) and the denominator is a ratio of the apparent cross-sectional area of the saturated porous media (A') to the cross-sectional area of the sample (A). This indicates that the formation resistivity factor is dependent on the pore geometry due to the tortuosity factor. Winsauer et al. (1952) defines the resistivity factor as Equation 1.11 where (τ) is tortuosity and (ψ) is the ratio of areas. Substituting in the tortuosity derived in Equation 1.9 will produce the most accurate formation resistivity factor as it uses a direct measurement of tortuosity.

$$F = \frac{\frac{L'}{A'}}{A} \quad (1.10)$$

$$F = \frac{\tau}{\psi} \quad (1.11)$$

The determination of tortuosity utilizing ion travel time is a more accurate representation for calculating resistivity; however, a specific model describing the rock structures influence on the observed electrical behavior has still to be discussed. Originally proposed in (1993) by Herrick and Kennedy, electrical efficiency theory (EET) looked into determine how electric current passes through a brine solution within the complex rock pore space in relation to the same brine solution in a straight tube. The method of EET accounts for the effects of pore geometry and rock-fluid interactions on the conductivity. Utilizing the electrical efficiency theory, experimental studies have shown that tortuosity is commonly less than two in Archie rocks, and for rocks with uniform grain size and shape tortuosity drops to be less than 1.5 (Herrick 1988). It is generally assumed for Archie rocks that the value of the tortuosity factor be equal to two. This difference between the general assumption and the more accurate findings from Herrick (1988) can affect log interpretation studies for formation evaluation, which would lead to inaccuracies in the determinations of porosity, water saturation, and hydrocarbon volumes.

The electrical efficiency theory model relates the conductivity of a saturated rock to the conductivity of the conducting phase (C_w or R_w if noted as resistivity), porosity (ϕ), the saturation of the conducting phase (S_w), and the geometric distribution of the conducting phase within the pore structure (E). The final factor, as presented by Herrick and Kennedy, (1993), (E) accounts for the geometric distribution of the brine solution and its effects on the conductivity. A value of (E) equaling to one represents the most efficient path of travel in a conductive solution, being a single phase, fully saturated straight tube. A mathematical relation for the electrical efficiency (E) is shown in Equation 1.12 (Herrick and Kennedy, 1993). As the electrical currents path becomes more complex, the value of (E) decreases

with increasing complexity of the pore structure in the rock. This is also shown in the equation, because the denominator represents the conductivity of a solution in a straight tube, while the total conductivity (C_t) of the water-bearing rock would decrease to zero if the path becomes too complex that it cuts off electrical current. Assuming that the rocks saturation and porosity does not change, the electrical efficiency is purely a function of the geometric characteristics and any potential rock-fluid interaction of the interconnecting pore space (Herrick 1988). The pore structure of the rock is dependent on many factors which further complicate the accurate determination of the electrical properties of porous rock media.

$$E = \frac{C_t}{C_w S_w \phi} \quad (1.12)$$

As mentioned, a simple straight tube model of porous media produces an electrical efficiency equal to one, and the ratio of total conductivity and brine conductivity in such case are equal to porosity if fully saturated. As the brine filled tube bends and twists randomly in a more natural porous rock like structure, the electric current distribution is not even. The constrictions created between grains, i.e. the pore throats, restrict the flow of electric current and decrease the electrical efficiency. Also, there are an infinite number of paths which current can flow, as described in Figure 1.3, a measure of tortuosity which affects electrical efficiency. Hence, electrical efficiency is a geometric factor characterizing the effect of pore fluid distribution on the rock-fluid systems conductivity Herrick and Kennedy(1993). Further work from Herrick and Kennedy (1993) showed that conductance in a porous system is dependent on the pore throat geometry, other pore-geometric parameters have minimal effect on the conductivity in comparison to the pore throats. Figure 1.4 illustrates how the pore throats restrict the flow, while the total porosity is less influential on the geometric factor as the complexities at the pore throats decrease the electrical efficiency factor.

Not only does the pore geometry affects the conductivity, but so does the direction of flow when pore geometry changes with the direction. This represents that total conductivity and Archie's cementation and saturation exponents are then directionally dependent (Herrick

et al. 2001). This is also relevant from the results of directionally dependent permeability measurements shown later in the results of this work. Directional dependent electrical properties then leads to question that differing water saturations can be determined dependent on the measured direction of the flow. The calculation of water saturation independent of direction is addressed in a latter section and the effects of the anisotropy on resistivity are also discussed.

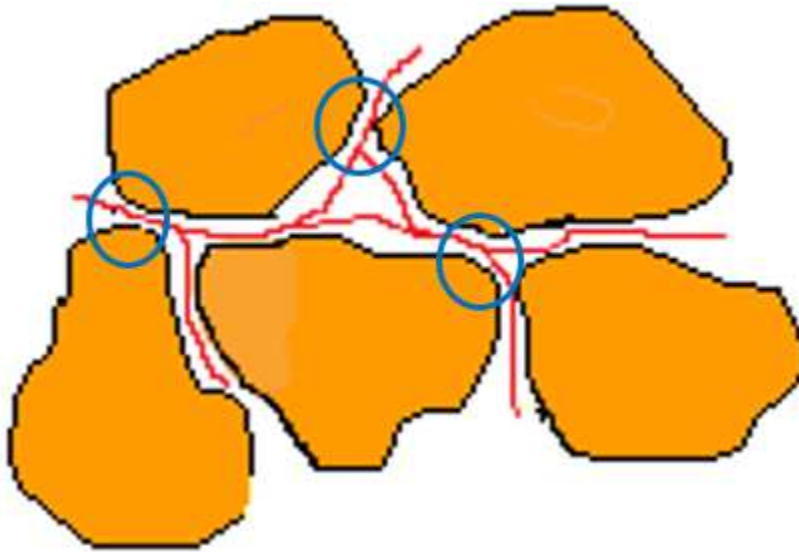


Figure 1.4: How the flow of electrical current is restricted at the pore throats as represented by the red lines and the constrictions at the pore throats are circled in blue.

When examining real world rocks like sandstones, shales, and carbonates a realization is observed that porosity does not influence the electrical efficiency factor. For example, shales typically exhibit high electrical efficiency due to surface conduction and the brine conduction within a highly connected pore structure (between clay platelets filled with bound water). Carbonates with isolated vugs with higher porosity will have low electrical efficiency due to the isolation of the pore fluids and low connectivity. On the other hand, a carbonate which is highly fractured will increase electrical efficiencies. A relation between the different rock types and electrical efficiency is shown in Figure 1.5 (Herrick and Kennedy, 1993). There seems to be relationships between porosity and electrical efficiency as normally high porosity

systems will have greater connectivity between pore space; however, this is a property of the pore geometry and connectivity, not porosity.

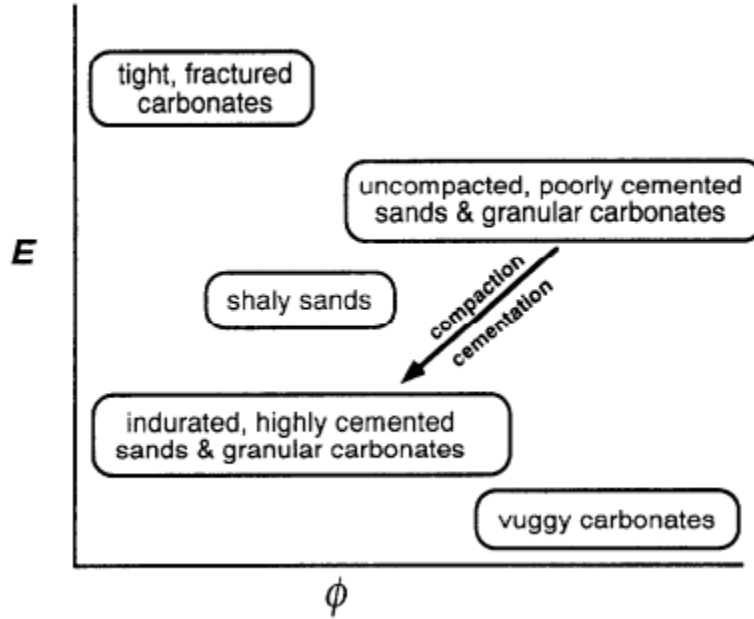


Figure 1.5: Relation between electrical efficiency and pore geometry, how porosity alone does not determine electrical efficiency due to either highly connected pores, or isolated vugs. Image sourced from (Herrick and Kennedy 1993).

1.3.2 Stress State Effect on Pore Geometry and Resistivity

Changing the stress state of the rock has been observed to affect significantly the porosity, permeability, resistivity, density, and wave velocities (Dobrynin 1962). Understanding the relationship between the effective stress and the resistivity measurements performed by understanding how the pore structure changes due to increases or decreases in the effective stress. Early work showing how effective stress specifically influences resistivity was performed experimentally by Dobrynin (1962) where she concluded that the changes in resistivity are primarily influenced by the closure or shrinkage of the smaller pore channels and presence of fine materials. Experimental data showing the effects on resistivity are presented in Figure 1.6. Longeron, Argaud, and Feraud (1989) followed, linking effective stress changes to varied values of both cementation and saturation exponents of Archie's equation, though

further work by Sharma et al. (1991) showing minimal effects on the cementation factor with stress increase as indicated in Figure 1.7. The cementing material for the grain structure is deformed with the reduction in porosity from the increased stress, thus increasing the cementation exponent (m); though, cementation factor is also dependent on lithology (Dobrynin 1962). Data produced from Sharma et al. (1991) experimental study did not match Archie's equation for saturation; altering the cementation and saturation exponent to match the experimental data brought the data set closer to the output of Archie's equation. Further work by Mahmood et al. (1991) showed that resistivity, formation factor, and Archie's cementation exponent all increase with increasing stress. This contradicts work of Sharma et al. (1991) that showed minimal change with increasing stress.

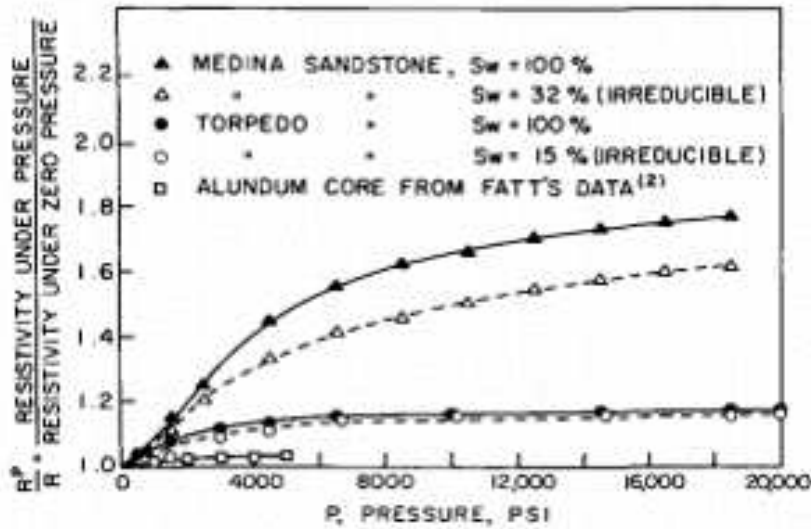


Figure 1.6: Experimental results showing the relation of increased rock pressures and resistivity. Shown are the effects of varying rock pressures, from 0 psi to 20,000 psi, on the measured resistivity as displayed by the ratio of the measured resistivity at increased pressures compared to the measured resistivity at zero pressure. These results are from Dobrynin (1962).

The change in cementation has been attributed to the pore structure change due to the stress state changes. Closure of the small, crack-like pore space is one of the primary influences on the cementation factor (Brace et al. (1965); Wyble (1958)). The effect on the cementation from the reduction in the pore throats as described is also dependent on the

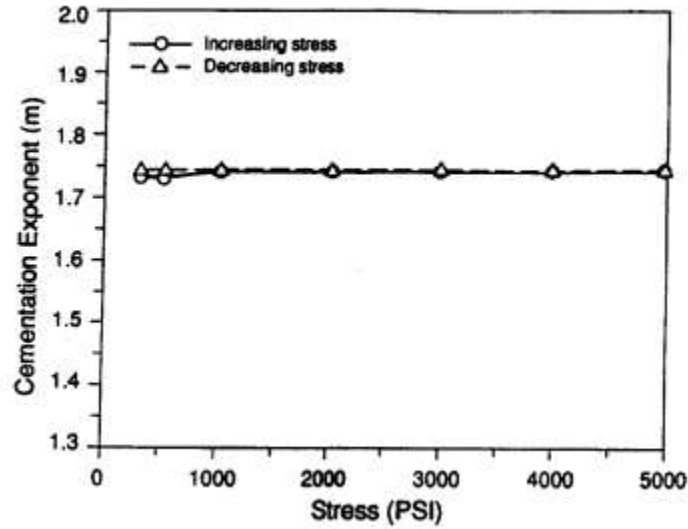


Figure 1.7: Experimental results showing the effects of increased stress ranging from 0 psi to 5,000 psi on the cementation factor for a saturated Berea Sandstone core. As it can be seen, there is minimal increase in the cementation factor with increasing stress. This experimental work is from Sharma et al. (1991).

porosity of the rock. Porous media with medium to low porosity experienced greater changes in the cementation factor with increased stresses (Glanville 1959). Where as Redmond (1962) reported the opposite, that a decrease in cementation factor was observed with greater effects for sandstone rocks with higher porosities. Also, clay content of the rock inadvertently affects the cementation factor in that there is an increase in cementation factor due to clay swelling which is influenced by the saturating fluid; however, the effects of clay swelling can be accounted and adjusted for (Clavier et al. 1984). Let it be known, that temperature also has an effect on the cementaion factor, as shown by Mahmood et al. (1991) in the form of increased temperatures resulting in decreased cementation values. This change is attributed to increase in liquid pressure due to the temperature increase, which in turn would cause changes in the porosity from the relation between pore pressure and rock stress as explained in the effective stress equation.

As the effective stress on a rock increases, compaction can occur. An increase in resistivity is observed because the pore space decreases with compaction; therefore, decreasing

conductivity due to an increase in tortuosity and decreasing pore throat cross sectional area. Formation factor also changes due to a decrease in porosity because as tortuosity increases the formation factor will also increase as shown in Equation 1.5. Changes in wettability with stress are more challenging to interpret as studies have shown both increases and decreases in wettability with increasing stress, (Longeron et al. 1989; Mahmood et al. 1991). Experimental work performed by Sharma et al. (1991) showed that saturation exponent is affected by stress differently for oil and water-wet rocks. Results showed that water-wet cores saturation exponent varied 7% during drainage, while oil-wet cores varied only 4% during drainage. In the same work performed by Sharma et al. (1991), oil-wet beads which were asphaltene-coated showed plastic deformation under increased stress. These inelastic deformations cause hysteresis in the test data, because when stresses are relieved the deformed state of the pores remain, altering porosity and tortuosity. This is relevant for in situ reservoirs as compaction can occur during depletion; however, the enhanced oil recovery techniques like water injection could bring pore pressures back up and create error during the log interpretation stage.

Further experimental studies have shown the differing results from changing overburden pressure, pore pressure, and net confining pressure. Mahmood et al. (1991) observed that the measured resistivity of a fully saturated sandstone is independent of absolute pore pressure and overburden pressure; that resistivity is a function of net confining pressure. Looking at their results in Figure 1.8 it is evident that there is an increase in resistivity as overburden pressures increase at any given constant pore pressure. Moreover, increasing the pore pressures decreases the resistivity. These correlations are evident when examining how each affects the effective stress. As discussed before, an increase of overburden pressure increases effective stress while an increase in pore pressure decreases effective stress. Knowing that effective stress changes the rock structure, thus affecting pore geometry explains why resistivity is dependent on the stress state of the rock. Looking at the net confining pressure in Figure 1.8, it is observed that at constant net confining pressures the resistivity stays

relatively constant, showing a slight decrease with increasing pore pressure.

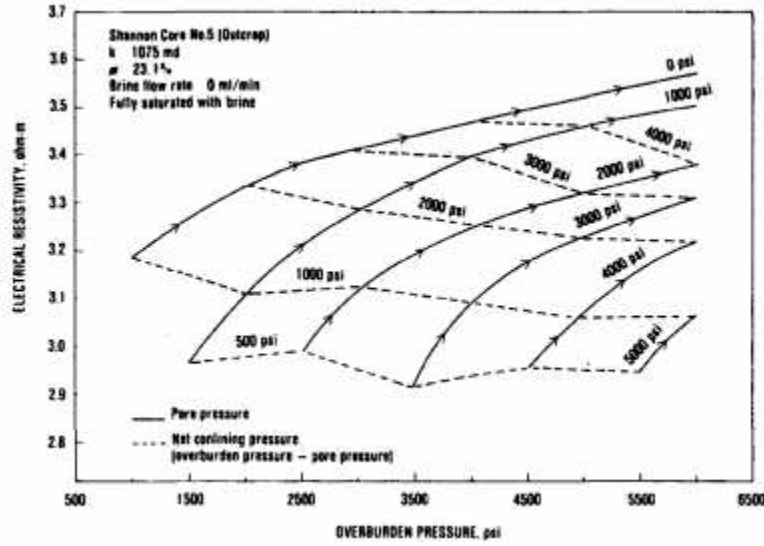


Figure 1.8: Experimental results showing increases in resistivity due to an increase in overburden pressure while decreases in resistivity are observed with increasing pore pressure. This can be explained by the effective stress equation which represents the stress felt by the rock matrix (Mahmood et al. 1991).

During the consolidation test of the rock samples for this experimental study, resistivity is measured to examine how the compression and closure of the nano-pore space affects the measured values. This change relates the effective stress applied on the sample to resistivity, bringing us to Archie's method of relating bulk resistivity of a clean sandstone to brine resistivity, porosity, and saturation as shown in Equation 1.13. The relationship can be calculated to predict water saturation of the rock, once bulk conductivity (σ_t), brine conductivity (σ_w), and porosity (ϕ) are known. This relationship is altered with the three adjustable parameters, cementation exponent (m), saturation exponent (n), and a tortuosity factor (a). Further examination of the variables shows that porosity, brine conductivity, and water saturation are bulk properties, while bulk conductivity, cementation, and saturation are dependent on pore geometry (Herrick et al. 2001), leading to the understanding that alterations in effective stress results in changes to the rock matrix pore structure, consequently affecting the resistivity. It can then be theorized that Archie's equation should not

be dependent on cementation and saturation exponents, rather a geometric factor (E_o), as proposed by Kennedy and Herrick (2012). The geometric factor is similar to the electrical efficiency as described earlier. The relation of the geometric factor with conductivity and porosity is shown in Equation 1.14 (Kennedy and Herrick, 2012).

$$\sigma_t = \sigma_w * \phi^m * S_w^n / a \quad (1.13)$$

$$E_o = \frac{\sigma_o}{\sigma_w * \phi} \quad (1.14)$$

An experimental plan is developed to adapt the current triaxial cell for resistivity measurements in determining the saturation and potentially track fluid migration through the shale samples studied in this research. In Chapter 2 of this thesis, the changes to the experimental set-up has been outlined and the proposed test matrix is presented. Pore pressure penetration tests have been performed on Berea Sandstone, Eagle Ford and Pierre shale samples with results displayed later in Chapters 3 and 4.

1.3.3 Relationship between Water Saturation and Resistivity Measurements

Archie's original work characterized the formation resistivity to be related to the product of the formation fluid resistivity, the formation resistivity factor, and the resistivity index (I) as presented in Equation 1.15. Furthering this equation, water saturation can be determined if relationships between the formation resistivity factor and the porosity, as well as the resistivity index and the formation water saturation can be established. The relation between formation factor and porosity is complex; determining an exact relation depends on the deposition of the rock to be ideal, but not efficient. Experimentally, (F_r) is determined by saturating cores with a brine solution, then resistivity is measured, allowing (F_r) to be computed for the sample. Utilizing multiple samples with varying porosity creates a relation between porosity and formation resistivity factor which can be plotted. This exact plot, F_r vs: (ϕ) is how Archie determined the porosity exponent (m) representing cementation of the grains. Discrepancies in the calculation of (m) due to plot scatter are most likely related to differences in deposition and diagenesis (Herrick et al. 2001).

$$R_t = R_w F_r I \quad (1.15)$$

Looking at the inaccuracies observed in Archie's equation, 1.3 for tortuosity, cementation, and pore throat geometry there are also questions concerning the relation of resistivity index (I) correlation to water saturation as it is an empirical relationship altered by the saturation exponent (n), which is again obtained from the slope of a log-log experimentally derived plot. This relation is determined experimentally by using a single core to increase and decrease water saturation to determine the respective resistivity. What is not accounted for is the microanisotropic changes from the saturation of the core. Rock-fluid interaction alters the physical pore geometry, thus affecting the electrical current path and ultimately varying resistivity (Herrick et al. 2001). Determining water saturation utilizing the Electrical Efficiency theory equates water saturation from the electrical properties of the rock and groups the effects of pore geometry into the term (E_o) as presented in Equation 1.16 (Herrick et al. 2001). The electrical efficiency is separate from that of porosity and water saturation, however it is still empirically related to the two factors.

$$\sigma_t = \sigma_w \phi S_w E_o \quad (1.16)$$

Utilizing the electrical efficiency, as introduced in the prior section, for clean rocks linear trends are observed between electrical efficiency and the water saturation (Herrick and Kennedy, 1993). Further work performed by Herrick and Kennedy (1993) showed the relation between water saturation calculated from the electrical efficiency in isotropic conditions with two adjustable parameters (a_t) and (b_t) which are empirically solved for, in Equation 1.17. The relationship is linear, compared to Archie's equation for porosity values above ten percent the two equations correlate well; however, below 10 percent porosity subtle differences occur. Also, the discrepancies are observed between the two relations at low water saturations. A more complex relation is formed to relate resistivity index to water saturation, accounting for the electrical efficiency of the porous rock structure as shown in Equation 1.18. Altering Equation 1.18 for conductivity, a quadratic relationship between porosity and

water saturation is presented in Equation 1.19, which is representative of isotropic rocks. To form the equation for anisotropic conditions, (a_t) and (b_t) are directionally dependent, thus, the conductivity in the x, y, and z can then be broken out, represented by the tensor in Equation 1.28.

$$E = a_t \phi S_w + b_t \quad (1.17)$$

$$I = \frac{1}{E_o \phi} [a_t (S_w \phi)^2 + b_t (S_w \phi)] \quad (1.18)$$

$$\sigma_t = \sigma_w [a_t (\phi S_w)^2 + b_t \phi S_w] \quad (1.19)$$

Other factors play a role in the effects of Archie's saturation exponent (n) value. Sharma et al. (1991) showed in a experimental study how the wettability of the rock, either water-wet or oil-wet, affects Archie's saturation exponent. Experiments were performed on glass-bead packs utilizing two and four probe resistivity measurements. Results showed that the saturation exponent values were greater for oil-wet rocks in comparison to water-wet rocks. In a water-wet system oil occupies the larger pore space, a larger number of pore throats are filled with water and the oil cannot displace the water, resulting in minimal change to the resistivity with increasing water saturation. On the other hand, in an oil-wet system the pore throats are filled with oil which the water may or may not be able to flow through. Because of this, it is expected that larger changes in resistivity occurs with minimal changes in water saturation, dependent on the connectivity of the pores with water. This can be explained as the accessibility to the pore space during drainage and imbibition (Suman and Knight, 1997). For a water wet system the smaller pore areas, also pore throats, control the pore accessibility during drainage; whereas during imbibition, the larger pore areas control the pore accessibility.

Further, Sharma et al. (1991) showed that changing the stress conditions of the rock samples results in differing (n) values as well as the stress state determines the pore geometry of the rock. Experimental work to show the effects of pore geometry on the electrical properties and water saturation determination are challenging; however, Sharma et al. (1991) utilized

theoretical modeling to study the effects. Results showed that Archie's saturation exponent decreased in both oil and water-wet rocks when connectivity increased. The key conclusion from this small study is that increasing the mean pore size reduces the effects of wettability; while increasing the standard deviation of the pore size has the opposite effect. When standard deviation of the pore size increases, meaning a larger range in pore sizes becoming more non-uniform, it also increases the effects of wettability. For a water-wet rock with a higher standard deviation of pore size there will be a larger number of pores filled with water (Suman and Knight, 1997). This is due to the fact that when there is a large distribution of pore size, the number of water saturated small pores is higher than the number of water saturated large pores. This characteristic improves connectivity keeping conductivity relatively constant, which translates to the saturation exponent being reduced.

Correlations between time lapse resistivity and changes in shale water content have been introduced in more recent studies. However, these tests have been performed at atmospheric conditions and for wellbore stability purposes. Work performed by Javalagi et al. (1991) concerning shale absorption to aid wellbore stability calculations showed that at the core scale, resistivity decreases as saturation increases for both Pierre and Wellington shale samples tested when different salinities of NaCl and KCl were examined. The change in resistivity due to saturation versus time for a Pierre shale core with normalized resistivity data is shown in Figure 1.9. In this Figure, the decrease in resistivity as a function of increasing strain is presented. The increase in strain is representative of clay swelling within the core due to the increased saturation. Shale saturation was theoretically determined assuming a correlation between saturation and swelling, as measured with strain gauges measuring an increase in total porosity due to clay absorption. Coupling the dual-water model (Clavier et al. 1984) with the measured total porosity creates a comparison for the measured resistivity as water is absorbed (Javalagi et al. 1991). Measured resistivity values were in agreement with the dual-water model at early stages of the water infiltration supporting the theory that resistivity measurements can be utilized to track the fluid flow in shale samples over long period

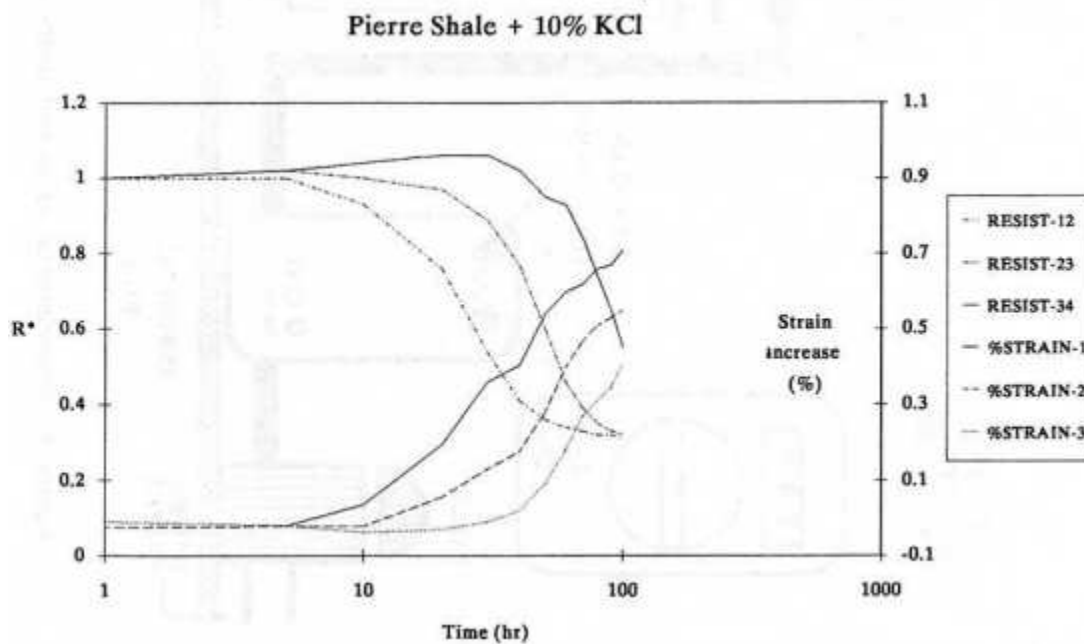


Figure 1.9: Normalized resistivity and percent strain increase for Pierre shale exposed to 4% KCl which is circulated at the base of the core and imbibed vertically. This shows that resistivity increases due to the swelling of the clays which reduces the pore geometry and absorption of the free water (Javalagi et al. 1991).

of time.

1.3.4 Resistivity Measurements in Anisotropic Conditions

Archie's law was originally determined in isotropic media, with anisotropy ignored for the interpretation of the resistivity. Anisotropy occurs due to alternating, thin bedding layers of varying resistivity where the layers are so thin that they are less than that of the resolution of the resistivity logging tool. The assumption to ignore anisotropy was largely agreed upon because the horizontal component of the resistivity tensor solely influenced the resistivity logging tools; thus, making it possible to ignore the vertical component (Herrick et al. 2001). Geological deposition of mineral crystals which are flat or elongated, mica and kaolin, cause much of the anisotropy. During deposition these minerals naturally laid down in parallel orientation of the bedding planes, making electrical current travel in the direction parallel to bedding (Kunz and Moran 1958). Due to their mineralogy, this is very common in shale

formations. Also, due to the alternating layers of varying lithologic characteristics adds to the differing values of resistivity observed in a formation. A simple quantification of the abundance of anisotropy is the ratio of the resistivity measured parallel and perpendicular to the bedding planes as described in Equation 1.20 (Kunz and Moran 1958).

$$\lambda = \sqrt{\frac{R_{\perp}}{R_{\parallel}}} \quad (1.20)$$

In recent times with the advent of horizontal wells anisotropy can no longer be ignored for correct resistivity log interpretations for formation evaluation. Anisotropic formations electrical properties are described by parallel and perpendicular resistivity components where the parallel is measured with the bedding and perpendicular is measured against the bedding, as presented in Equation 1.21 and Equation 1.22 (Schlumberger et al. 1934). Further work was performed by Klein, Martin, and Allen (1997) relating water saturation to both parallel and perpendicular resistivity by substituting Archie's Equation into resistivity of the macroporous (m) and microporous (μ) layers, obtaining Equations 1.23 and 1.24. Solving for water saturation using Equations 1.23 and 1.24 do not account for the directional dependence of the Archie exponents due to microanisotropic conditions. Further, conductivity or resistivity are also directionally dependent; therefore the value of water saturation would not be accurate unless specified for only one bedding layer.

$$R_{\parallel} = \left(\frac{V_m}{R_m} + \frac{V_{\mu}}{R_{\mu}} \right)^{-1} \quad (1.21)$$

$$R_{\perp} = V_m R_m + V_{\mu} R_{\mu} \quad (1.22)$$

$$R_{\parallel} = \left(\frac{V_m}{\left(\frac{a R_w}{\phi^m S_w^n} \right)_m} + \frac{V_{\mu}}{\left(\frac{a R_w}{\phi^m S_w^n} \right)_{\mu}} \right)^{-1} \quad (1.23)$$

$$R_{\perp} = V_m \left(\frac{a R_w}{\phi^m S_w^n} \right)_m + V_{\mu} \left(\frac{a R_w}{\phi^m S_w^n} \right)_{\mu} \quad (1.24)$$

Looking at the different causes of anisotropy there are two distinctly defined forms of anisotropy, microanisotropy and macroanisotropy. Microanisotropy is due to differing

pore geometries and channels in various directions and is prevalent in shale formations. Macroanisotropy is a bulk property representative of the alternating conductive-resistive bedding layers, these layers are grouped together by a logging tool with an observed average of the differing layers due to the resolution of the equipment, and are commonly seen in sand-shale sequences (Bittar and Rodney, 1996). Bulk conductivity, as described, can then be characterized by the average conductivity relative to the volume of measured media. The horizontal and vertical components of the macroscopic conductivity are found as represented by Equations 1.25 and 1.26, respectively (Schlumberger et al. 1934). These equations represent the volume-weighted average of the resistivity in both the vertical and horizontal directions (Clavaud 2008). One major issue grouping the volume together to form an average is that it does not account for the finite differences between each layer, which would result in differing water saturations. Going back to Equations 1.23 and 1.24 shows how if each layers' electrical properties can be measured then an accurate determination of water saturation can be solved; however, modern logging tools are not capable of measuring to such a degree of accuracy.

$$\sigma_h = V_{sh}\sigma_{sh} + (1 - V_{sh})\sigma_{sd} = \frac{1}{R_h} \quad (1.25)$$

$$\frac{1}{\sigma_v} = \frac{V_{sh}}{\sigma_{sh}} + \frac{(1 - V_{sh})}{\sigma_{sd}} = R_v \quad (1.26)$$

Archie's base equation for water saturation operates under the assumption that wettability, cementation, and conductivity are not directional dependent; however, these parameters are directionally dependent (Herrick et al. 2001; Mahmood et al. 1991; Woodruff et al. 2014). To correctly write Archie's equation accounting for the directional dependence, a tensor equation is formed, as shown by the series of 3 x 3 matrices in Equation 1.27. The individual equations can then be worked out from the tensor. Further work for water saturation in anisotropic conditions was performed by Herrick et al. (2001) which introduced (a_t) and (b_t) as empirically based constants to replace the cementation, wettability, and tortuosity exponents from Archie's equation for directionally dependent rock parameters. Determin-

ing water saturation in terms of electrical efficiency in anisotropic rocks is broken down in the x, y, and z directions in Equation 1.28, written in tensor form. These equations are only valid when the electrical measurements are taken in alignment with the conductivity tensor (Herrick et al. 2001). Solving for water saturation for this quadratic equation can be performed by completing the squares. This method is not applicable to the field though as modern logging tools do not have the ability to measure $(\hat{\sigma})$, rather this method is most useful for lab based work. Eliminating the use of the empirically derived exponents and replacing them with Electrical Efficiency as described previously simplifies the equations. Again, electrical efficiency is directionally dependent. Therefore, there will be conductivity equations for the x, y, and z directions as represented by the tensor notation in Equation 1.29.

$$\begin{bmatrix} \sigma_{tx} & 0 & 0 \\ 0 & \sigma_{ty} & 0 \\ 0 & 0 & \sigma_{tz} \end{bmatrix} = \sigma_w \begin{bmatrix} \phi^{m_x} & 0 & 0 \\ 0 & \phi^{m_y} & 0 \\ 0 & 0 & \phi^{m_z} \end{bmatrix} \begin{bmatrix} S_w^{n_x} & 0 & 0 \\ 0 & S_w^{n_y} & 0 \\ 0 & 0 & S_w^{n_z} \end{bmatrix} \quad (1.27)$$

$$\hat{\sigma}_t = \sigma_w [\hat{a}_t (\phi S_w)^2 + \hat{b}_t \phi S_w] \quad (1.28)$$

$$\hat{\sigma}_t = \sigma_w \phi S_w \hat{E} \quad (1.29)$$

Eliminating the use of the empirically derived exponents and replacing them with electrical efficiency as described previously simplifies the equations. Again, electrical efficiency is directionally dependent. Hence, there will be conductivity equations for the x, y, and z directions. It has also been studied that the effects of anisotropy are dependent on water saturation, as the macroporous layers drain more quickly than the microporous layers resulting in an increase of the anisotropy, up until irreducible water saturation occurs (Klein 1996). This effect of decreasing water saturation while observing an increase in the measured anisotropy is also observed by Klein et al. (1997). The resistivity ratio between parallel and perpendicular measurements is shown to increase for lower water saturations, this increase in the ratio represents an increase in the effects of anisotropy as shown in Figure 1.10.

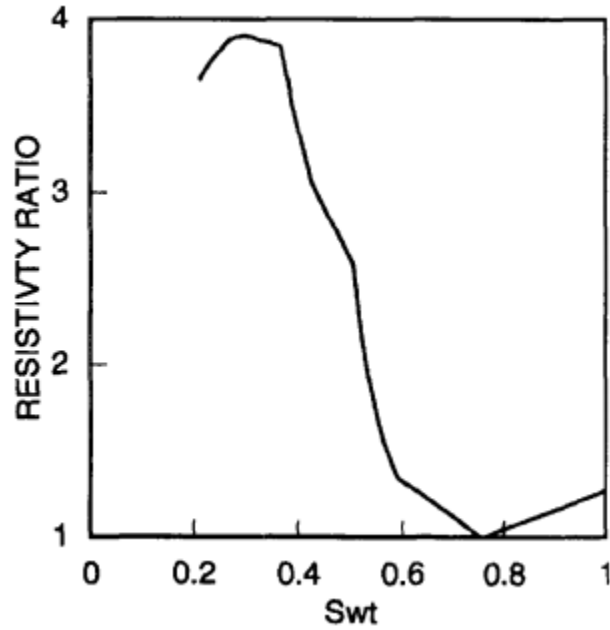


Figure 1.10: Effects of anisotropy increase from decreases in water saturation due to the preferential desaturation of the macroporous layers. The data obtained is obtained from the experimental work by (Klein et al. 1997).

1.3.5 Experimental Setup

The experimental setup for resistivity measurements is essential for accurate measurements. Previous work performed presents how volatile resistivity measurements are for stress state, temperature, fluid type, mineralogy, spacing between electrodes, voltage, and many other factors (Dobrynin 1962; Herrick et al. 2001; Mahmood et al. 1991; Redmond 1962; Sharma et al. 1991; Winsauer et al. 1952; Wyble 1958). Essential to the accuracy of the measurements is an appropriate lab setup for the tests.

One of the key differences between resistivity measurements is the use of two and four probe measurements. In general, experimental studies have shown that two probe measurements produce greater resistivity values than that of four probe measurements (Mahmood et al. 1991; Sharma et al. 1991). The use of a four probe measurement setup is more accurate as it negates the electrode surface resistance. Also, the choice of frequency does not affect the four probe method in comparison to large changes in resistivity seen by the two probe

method (Wang et al. 2009). It is best to determine the formation factor of a core with a very low resistivity fluid as it will negate the effects of conductive mineral deposits within the pore space like clay (Patnode and Wyllie, 1950). Examining the distance between electrodes, performed by Mahmood et al. (1991), showed that increasing the spacing of electrodes in a four probe measurement would decrease the resistivity index, as evident in Figure 1.11. Also observed from the results are how the effects of electrode spacing are increased for the lower electrolyte saturated cores.

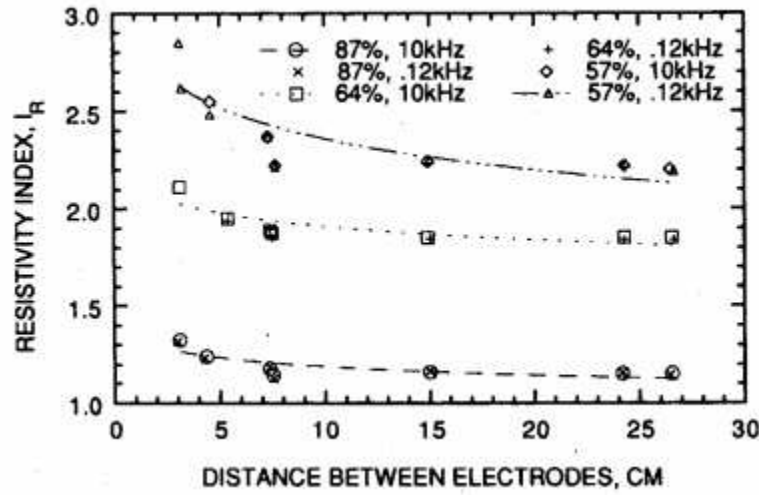


Figure 1.11: Varying the spacing of electrodes for four probe resistivity measurements shows that the further apart the spacing is produces lower resistivity measurements for the same sample. This work was performed by Mahmood et al. (1991).

The experimental setup used in this research is discussed in depth in Chapter 2 and in Appendix A. This section of the literature review is minimized as not to repeat what is discussed in the triaxial and resistivity measurement setup.

1.3.6 Log Analysis

An essential purpose of the resistivity log is determining water and hydrocarbon saturation of reservoirs for log interpretation and reservoir modeling purposes. Two key parameters are interpreted from resistivity logs; first, the porosity from the formation factor as first described by Archie (1942). Second, the relation between the electrical properties of the rock

and the saturation of that porous media. As described previously throughout this work the formation factor is heavily dependent on tortuosity, saturation, wettability, cementation, stress state, and anisotropy (Clavaud 2008; Dobrynin 1962; Herrick et al. 2001; Kennedy and Herrick 2012; Patnode and Wyllie 1950; Suman and Knight 1997). It is important to be able to account for these factors for log interpretation as an accurate representation of the reservoir is required for modeling purposes. Determining the formation factor from well logs is challenging due to the reading depth of the resistivity tool. To measure true formation resistivity, the deepest reading tool is best, being an AT90. Comparing the formation resistivity to that of the brine resistivity is most accurate representation of the formation factor. However, a hydrocarbon bearing reservoir formation cannot be determined directly due to the effects of the hydrocarbons on electrical resistance. Adjacent water saturated reservoir rocks can be used to determine the formation factor if it is deemed that the rocks share similar properties. If applicable, it is best to determine the formation factor within the same reservoir rock beneath the oil-water contact, though this is not always possible depending on the type of the reservoir.

Clavaud et al. (2005) showed that an overestimation of hydrocarbon saturation in upwards of 40 percent can occur if shale anisotropy is neglected during log interpretation. The effects of hydrocarbon overestimation are compounded when in transition zones or when the laminated shale volume is large. To accurately account for the anisotropy in shale, interpretations must be performed understanding the shale resistivity tensor components (R_{shale_h}) and (R_{shale_v}), the horizontal and vertical shale resistivity as seen in Equations 1.25 and 1.26 (Clavaud 2008). Early analysis with these equations performed by Worthington (1982) used the volume of shale (V_{sh}) to represent the fractional volume of wet-clay material, broken down to be the volume of dry clay and clay-bound water. Later work showed that (V_{sh}) should be equal to the fractional volume of rock occupied by clay, clay-bound water, and silt (Clavaud 2008). This analysis is still challenging due to the deposition of the rock as modern logging equipment does not have the clarity to define the extents of the shale and

sandstone layers to accurately determine the respective volumes of the differing rock types.

The dip angle of the bedding can affect the resistivity tool interpretation because the phase shift and attenuation measurements respond to the resistivity of the formation parallel to the bedding. As the dip of the bedding increases to about 45 degrees the effects are minimal; however, once the dip increases greater than 50 degrees the effects are significant (Bittar and Rodney, 1996). With the advent of deviated drilling and horizontal wells it is very common to have bedding angles intersecting the resistivity tool running down hole at angles greater than 50 degrees. Bittar and Rodney, (1996) studied the effects of the bedding dip on the phase shift response of a multiple-frequency measure while drilling (MWD) tool. As seen in Figure 1.12, the phase shift varies for greater bedding dip angles.

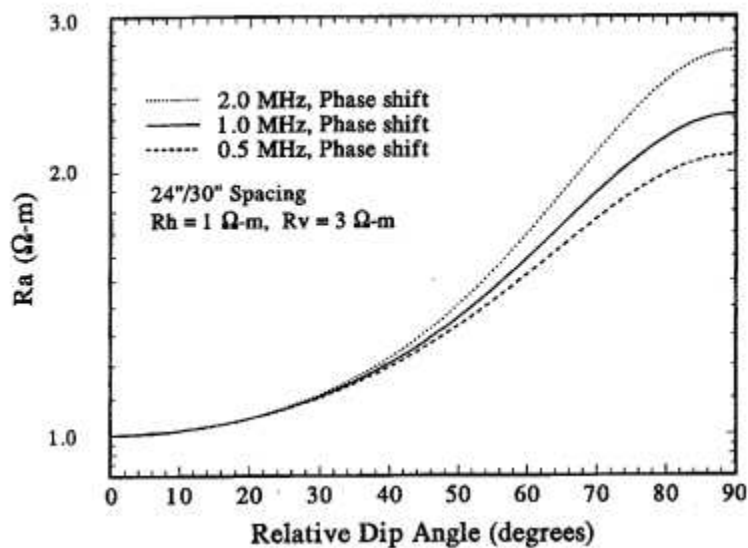


Figure 1.12: Relative dip angle influence on measured resistivity. It is seen that as the dip angle increases above 45 degrees the increase in resistivity become much more rapid. This work was performed by Bittar and Rodney, (1996).

When accounting for anisotropy in resistivity log interpretation, it is important to orient the resistivity tool readings to the bedding. Extensively explain by Moran and Gianzero, (1979), the transformation of the conductivity tensor from the x, y, and z coordinates to align with the bed coordinate system of x'', y'', and z''. Two rotations between the tool and bedding coordinates systems must be performed. First, for the z axis as noted by the

angle α in Figure 1.13, representing the dip angle of the bedding plane P. Second, is the dip azimuth as represented by the angle β , which aligns the x-axis with the dip azimuth and the y-axis with the direction of strike. The corrected conductivity for the bedding planes is then described for the x-x, x-y, x-z, y-y, and z-z directions as seen in Equations 1.30, 1.31, 1.32, 1.33, 1.34 respectively.

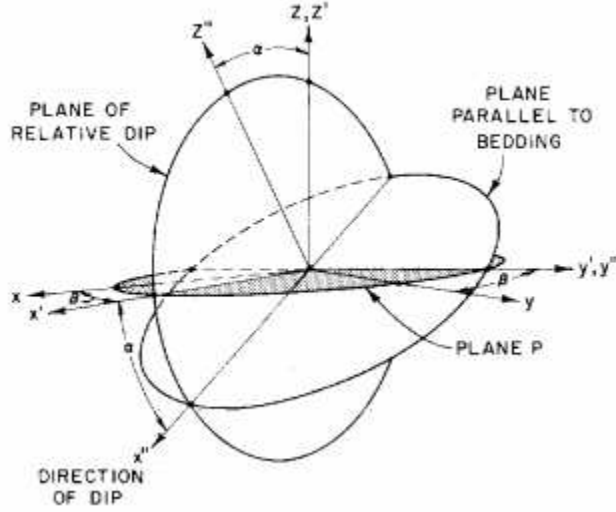


Figure 1.13: Rotation of the tool measured conductivity tensor to match the bedding planes of a formation (Moran and Gianzero, 1979).

$$\sigma_{xx} = \sigma_{\parallel} + (\sigma_{\perp} - \sigma_{\parallel}) \sin^2 \alpha * \cos^2 \beta \quad (1.30)$$

$$\sigma_{xy} = (\sigma_{\perp} - \sigma_{\parallel}) \sin^2 \alpha * \sin \beta * \cos \beta \quad (1.31)$$

$$\sigma_{xz} = (\sigma_{\perp} - \sigma_{\parallel}) \sin \alpha * \cos \alpha * \cos \beta \quad (1.32)$$

$$\sigma_{yy} = \sigma_{\parallel} + (\sigma_{\perp} - \sigma_{\parallel}) \sin^2 \alpha * \sin^2 \beta \quad (1.33)$$

$$\sigma_{zz} = \sigma_{\perp} - (\sigma_{\perp} - \sigma_{\parallel}) \sin^2 \alpha \quad (1.34)$$

Using resistivity to determine porosity can also be misleading as there are two forms of porosity which sum to total porosity, being the porosity associated to the flow or channel porosity and the porosity of the trapped fluid or trapped porosity. This has been mathemat-

ically shown in Equation 1.35. Relating the formation factor and the trapped and channel porosity is seen in Equation 1.36, where (f_G) is an internal geometry factor of the porous media. Resistivity measurements only account for the porosity which attributes to flow. This can be both beneficial and detrimental, because the porosity which attributes to flow is important to engineers. However, with hydraulic fracturing it would be possible to fracture into the closed pore space and extract the hydrocarbons in these areas as well.

$$\phi_{total} = \phi_{channel} + \phi_{trapped} \quad (1.35)$$

$$F_R = 1 + f_G \left(\frac{1}{\phi_{ch}} - 1 \right) \quad (1.36)$$

CHAPTER 2

EXPERIMENTAL SETUP

In this section, the experimental setups used for the laboratory study performed in this research study are described. There are three different experimental setups that were utilized. First, an atmospheric test assembly was used to initially to determine the viability of using resistivity measurements to track fluid flow. The results from the atmospheric test proved that the resistivity setup could provide insight into the fluid migration through the samples tested. From this positive result a resistivity measurement system was designed and implemented into the larger triaxial cell. The second setup is for the large triaxial cell which required minor adaptations to implement resistivity measurements for the shale and sandstone samples tested. Third, a smaller triaxial cell was adapted for a new pore fluid injection system to electrically isolate the core and pore fluid injection system from potential of an electrical shortcut occurring around the sample through the injected pore fluid. The separate pore fluid injection system was custom designed and manufactured at the Colorado School of Mines campus by Andrew Rixon and Dr. Daisuke Katsuki.

2.1 Sandstone Ambient Condition Validation Measurements

To prove our experimental design that the electrodes selected could measure resistivity and could track fluid migration, a set of atmospheric saturation tests were performed using sandstone samples. Multiple tests were performed on multiple sandstone samples to determine if the electrode setup and resistivity measurements would work as intended. Each sandstone sample used is three inch tall by one-and-a-half inch diameter Berea Sandstone core with six circumferential electrodes placed perpendicular to its length, utilizing a two probe resistivity measurement. The samples were placed into beakers with the base submerged into either distilled water or a brine solution. The first test was performed using deionized water, then followed by a test with 18% potassium chloride (KCl), and another

with 18% sodium chloride (NaCl). The electrodes adhered on to the sample were comprised of a copper ring epoxied to the sample surface using a silver-chloride epoxy. Wire leads were connected to the copper wires for our multimeter to connect to for resistance measurements. The atmospheric resistivity test assembly is shown in Figure 2.1 accompanied by its designed graphical representation.

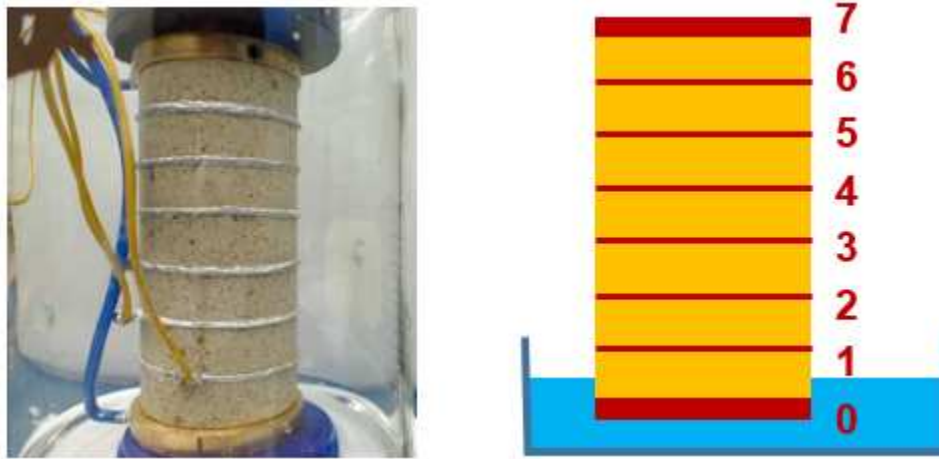


Figure 2.1: Atmospheric resistivity measurement test setup used for validation of the theory. (Left) the actual sandstone sample placed into a beaker with brine solution at the base. (Right) graphical representation of the electrode setup on the sandstone sample.

Results from the three atmospheric tests showed that there is a clear correlation between the visible water height and an observed decrease in resistivity. The results for the 18% KCl solution are represented graphically in Figure 2.2. The displayed resistivity results are measured between the base electrode (0) and the other electrodes vertically spaced up on the core. The visual water level migrated vertically through the sample and as a result the resistivity decreased. The lowest electrodes, closest to the water surface, were the first to indicate a decrease in resistivity. As the brine solution migrated vertically, the other electrode resistivities also dropped. It was observed that for each set of electrodes the resistivity decreases to a lower asymptotic limit.

It can be concluded from this benchtop experiment that full saturation of the sandstone sample does not occur until all of the electrode pairs resistivity measurements reach the

observed lower limit. Comparing the resistivity measurements with the observed water height, highlighted in red in Figure 2.2, represents that the water migrates in the shape of a concave up paraboloid. Migration occurs more quickly around the edges and slower at the center. This observation can be concluded upon due to the faster increasing water height on the outside of the core which is visually observed in comparison to the interval resistivity which represents when full saturation occurs. For the purpose of the shale osmotic pressure tests in a triaxial cell, it is essential to have full saturation of the core.

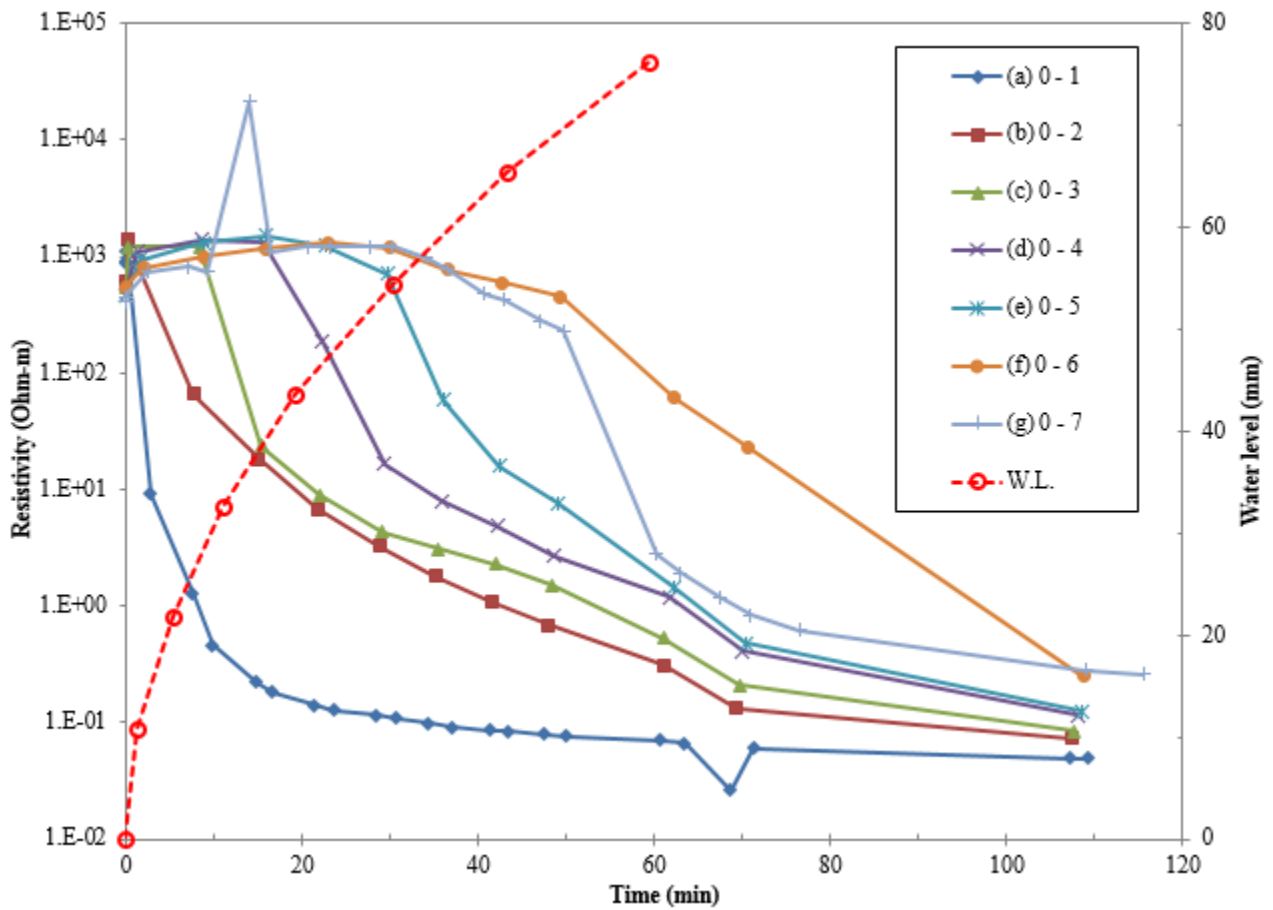


Figure 2.2: Resistivity measurements for an atmospheric sandstone sample with its base submerged in an 18wt.% NaCl solution. The two probe resistivity measurements were taken using the base electrode (0) as a reference to the other electrodes along the length of the sample.

The resistivity data must be carefully monitored and a second verification of saturation through the use of Skempton's b-coefficient as displayed in Equation 2.1 will be calculated. Skempton's b-value is a strong evaluation of core saturation in an experimental setup. The equation works by physically altering the pore pressure of the pore fluid (this is not possible for atmospheric conditions, rather only in a triaxial cell). The change in pore pressure should represent a direct change in stress. In perfect conditions, and if the core is fully saturated, Skempton's b-coefficient should be equal to one. However, the equation is only accurate assuming no change in pore volume due to the accompanied pore pressure change. Skempton's b-value normally ranges around 0.8, and represents an acceptable value to represent full saturation. If the values are lower than 0.8, the core is most likely not saturated fully and a change in pore pressure without an equal change in stress either filling or evacuating the pore space.

$$B = \frac{\Delta P_p}{\Delta \sigma} \quad (2.1)$$

Results from the atmospheric test proved our initial design concept worked. Further iterations of the atmospheric design are required for use in the triaxial cell. A resistivity measurement system for the triaxial cell must be first designed and then implemented into the cell and again tested for its validation.

2.2 UNGI Laboratory Triaxial Test Assembly

The original test assembly for the pore pressure penetration tests for the purpose of the osmotic pressure work did not include resistivity measurements. The data acquisition included vertical strain through a linear variable differential transformer (LVDT), pressure differential between the top and bottom surfaces of the samples through a differential pressure transducer (DPT), vertical compressional and shear wave velocity measurements, and permeability measurements. The addition of resistivity provided an aid in correlating all the previously mentioned measurements in an effort to better understand the fluid-rock interaction taking place during the osmosis process.

2.2.1 Triaxial Cell

Central to the success of this experimental study is the use of a 10,000 psi custom designed and fabricated triaxial cell, which has been graciously donated to Colorado School of Mines UNGI Consortium by Dr. Ali I. Mese, for this we are very grateful. This cell provides the ability to simulate reservoir conditions on rock samples in our laboratory. Four pumps provide the necessary overburden and axial pressure, confining or radial pressure, and inlet pore and back pressure. For the pore pressure system, two syringe pumps are separated from the pore fluid system and drive two piston cylinders containing the pore fluid. The purpose of the cylinders are to separate the high precision syringe pumps from the potentially harmful pore fluid. Contained in the pore fluid are salts which would damage the integrity of the syringe pump seals. Also, the two cylinders enable the use of other injection fluids like hydraulic fracture fluids with other chemical composition. In addition to the syringe pumps is a vacuum pump connected into the system to ensure all the air is vacuumed out of the pore fluid lines prior to each experiment.

Proper assembly of the cell is essential for the integrity of the system to be maintained throughout the long experiments. First, it is imperative to apply vacuum grease to all seals before the triaxial cell is assembled. Second, the bolts which attach the end caps to the main body must be carbon steel grade seven bolts, because this material will not respond elastically to the increase of fluid pressure, eliminating any pressure relaxation due to prolonged high stress exposure during testing. Lastly, all connection attachments must suffice the pressure requirements of the cell. HiP and Swagelok high pressure joints, unions, connections, pipe work, and valves are utilized due to the high standards of manufacturing and pressure ratings.

The triaxial cell is designed to sustain prolonged pressures for testing. The limits are as follows: axial pressure-10,000 psi, confining pressure-7,000 psi, pore pressure-6,000 psi, and vacuum system-150 psi (based on the syringe um limits and not based on the system design limits. The system can sustain up to 50,000 psi in each direction as well as 30,000 psi

pore pressure). As known from basic engineering courses, pressure is highly dependent on temperature. To consistently control the test conditions that will impact the measurement accuracy and safety, the entire testing assembly has been placed within a custom temperature controlled insulated cabinet, as depicted in Figure 2.3 (Padin 2016). The cabinet not only keeps the system at a constant temperature, but also protects the assembly from potential damage or wrongful alterations as it contains the entire assembly, the triaxial cell, pumps, and valve system. Within the cabinet a constant temperature flow of air is maintained at 40 degrees Celsius.

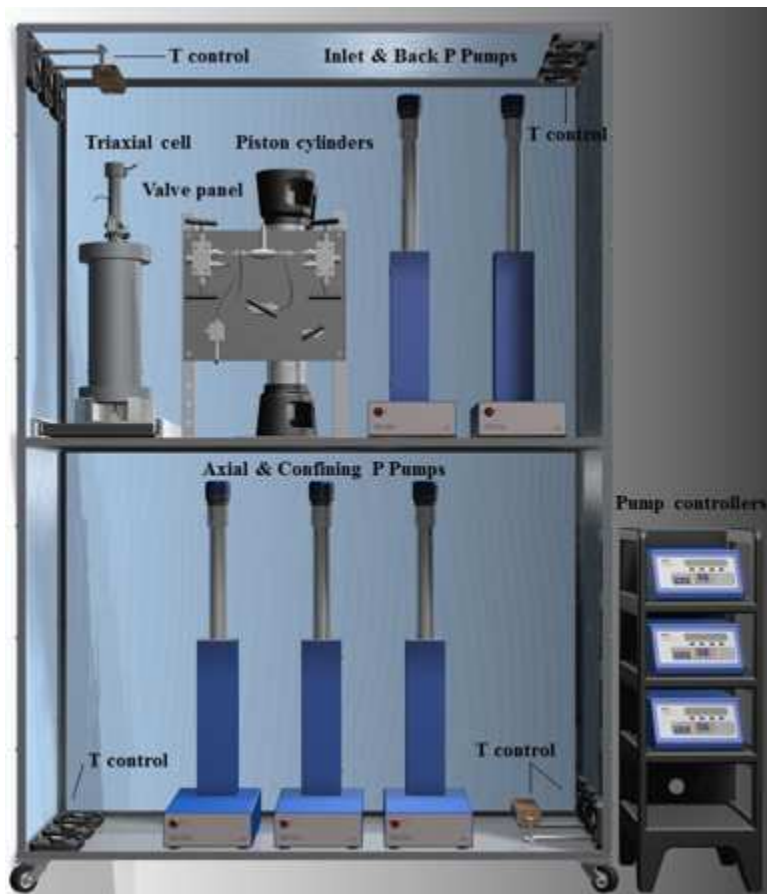


Figure 2.3: Temperature controlled testing cabinet layout used in the UNGI Laboratory at Colorado School of Mines. Two heating elements with circulation fans are controlled to maintain a constant temperature throughout the duration of the testing period Padin (2016).

The hydraulic fluids used to apply pressure on the core sample must be isolated within the cell. For this, the cell is designed to have two chambers which are sealed from one another using a triple O-ring placed on the center axial piston. The O-ring seals help to close off the pathway for escaping fluids. The integrity of the high pressure system and absence of leaks is highly dependent on the high quality O-ring seal. For these O-rings torus or doughnut in shape Viton elastomer 90 durometer, in the AS-568 scale are utilized. These are the standard for the Aerospace industry according to the Society of Automotive Engineers (S.A.E.).

Essential to accurately measuring the core samples resistivity is to electrically isolate the core sample within the triaxial cell from any source of current or potential electrical shortcut circumventing the core sample. The custom designed and fabricated triaxial cell has been designed to electrically isolate the core within the cell. To disassemble and assemble the test cell a series of O-rings have been used for leak prevention and for the electric isolation of the cells end caps and axial piston. Moreover, the use of non-conductive hydraulic fluid is essential for both confining and axial fluids as to not allow current to flow around the core through these hydraulic fluids.

Also, a set of conductive probes are fit into the base endcap to provide an electrically isolated method of taking electronic measurements inside of the cell and propagating the results through the cell wall to an appropriate meter. The pore pressure penetration testing cell when disassembled and assembled is shown in Figure 2.4. One main issue which prior experiments had not addressed, as found in an extensive literature review is the flow of current through the injected pore fluid. A new end cap for pore fluid injection has been designed to prevent a shortcut around the test cell from the current flowing through the pore fluid and around the core.

With the assembled triaxial cell the core plug sits between two axial pistons, when hydraulic fluid pressure is applied to the axial chamber the upper piston compresses the sample to the selected in situ overburden pressure. Confining fluid is pumped into the side of the cell to simulate the horizontal confining pressure. This triaxial cell can produce isotropic



Figure 2.4: (Left) assembled triaxial testing cell displaying the end caps and (right) disassembled triaxial testing cell showing the internal axial piston (Padin 2016).

conditions, meaning a vertical stress and a singular horizontal stress. Pore pressure is introduced at the base of the core, where pore fluid is constantly circulated and imbibed vertically through the core. A rubber sleeve isolates the core from the confining pressure; however, this sleeve has small perforations created to run wires to the resistivity electrodes. These small perforations were sealed to stop hydraulic fluid from entering the sample, or for pore fluid from leaking out. A schematic representing the large triaxial cell set up with the core in place is represented in Figure 2.5.

To further isolate the sample within the large triaxial cell, the pipe and valve layout were altered to include non-conductive high-pressure hoses into the pipe layout. Previously, the stainless steel pipe system directly ran into the triaxial cell without an electrical separation, the addition of non-conductive hoses prevents the flow of electricity through the stainless steel pipe material. The location of the non-conductive hoses are illustrated in Figure 2.6, which represents the complete schematic setup of the triaxial testing system. Non-conductive hoses are represented in the schematic by the green lines labeled NC.

Plexiglas backing plates were installed between the structural frame of the testing cabinet and all pipes, valves, pumps, fluid reservoirs, and the testing cell. The backing plates isolate

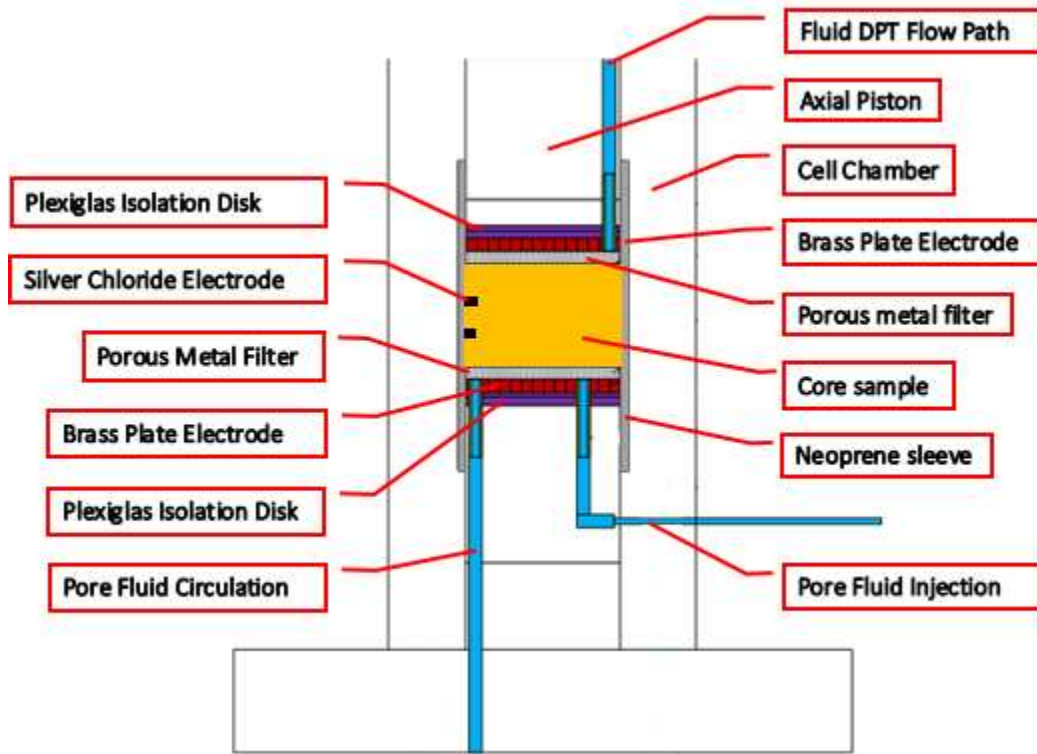


Figure 2.5: Schematic representation of the large triaxial cell setup as pictured within the triaxial cell. The core (orange) is centered between two axial pistons. Sandwiching the core are two porous metal filters to disperse the pore fluids. Sandwiching the filters are two electrode plates used as source current for resistivity measurements..

the items from any electrical current from passing between the testing frame and the fluid system. A set of plexiglas buffer disks were fabricated and installed onto the ends of the testing cell axial pistons, placed between two custom fabricated brass end caps and the cell pistons. Incorporating these changes isolated the core from potential electrical interference that would skew resistivity measurements.

While performing pore pressure penetration calibration tests on sandstone samples, the effectiveness of the electrical isolation of the core was checked to observe any effects of the measured resistance. The following three alternative setups were tested to observe any changes in resistance measurements on the sample.

1. Isolated: Drain, vacuum, and disconnect non-conductive hoses to isolate the pump pore pressure fluid from the core native fluid and disconnect all electrical plugins for

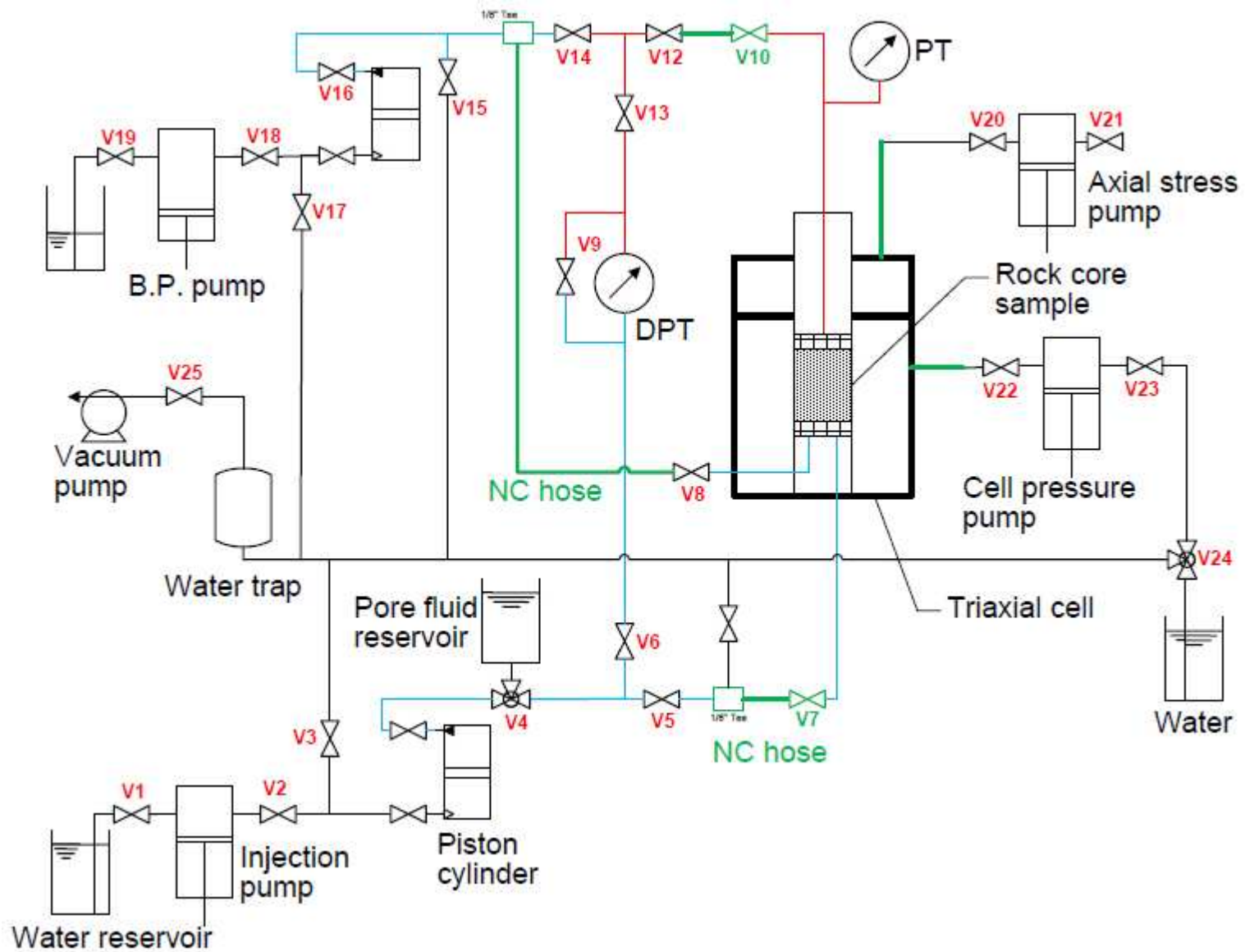


Figure 2.6: Schematic design of the larger triaxial test systems valve and pump setup used in the osmotic pressure and resistivity tests. The location of the non-conductive hoses are highlighted in green and labeled NC hose.

differential pressure transducer (DPT), linear variable differential transducer (LVDT), and acoustic assembly.

2. Non-isolated: Drain and vacuum non-conductive hoses to isolate the pump pore pressure fluid from the core fluid and connect all electrical plugins for gauges.
3. Non-isolated DIW: Allow for flow of water into triaxial sample cell and keep all electrical plugins connected.

Resistance measurements observed from the three alternative setups on the sandstone showed little difference between the isolated and non-isolated alternatives, as seen in Figure 2.7. The third alternative which maintained fluid flow while the measurements were being taken showed the greatest difference. As shown in the graph, the three varying setups follow the same trends, while the isolated and un-isolated vacuumed trials are close to identical. From the observed findings, it is concluded that to achieve the most accurate resistivity measurements, the pore fluid system should be completely isolated from the triaxial cell under the current setup.

2.2.2 Pore Pressure Electrical Isolation Endcap

The newly designed end cap for pore pressure is imperative for complete electric isolation of the core samples being tested. Originally the larger triaxial cell as pictured in Figure 2.4 did not have the capabilities of electrically isolating the pore fluid as the electrical current will flow the path of least resistance, circumventing the core through the wall of the testing cell. For impedance measurements a current must pass through the core. To ensure this, a custom set of end caps were designed and machined.

A schematic drawing of the function of the end cap is presented in Figure 2.8. The end caps are machined out of 1.5 inch diameter aluminum rod and coated with a black-hard anodize coating. The anodized coating isolates the pore pressure end cap from the axial piston, stopping electrical current passing through the pore fluid, into the axial piston and circumventing the core around the triaxial cell. The pore pressure pipes which enter into

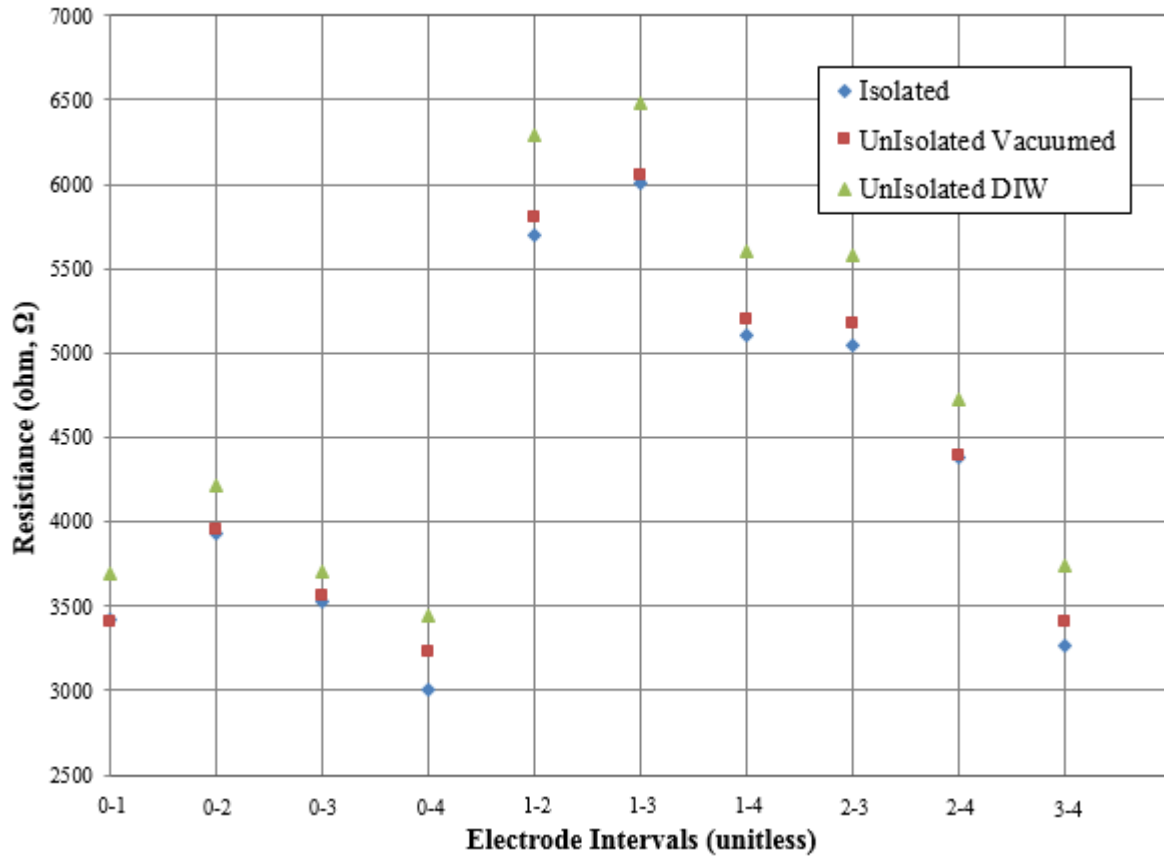


Figure 2.7: Resistivity measurements performed to determine the isolation of the core. Three separate setups were checked to determine any variance in the resistivity measurements from outside electrical sources.

the triaxial cell are isolated using plastic casings; these are then cemented into a custom machined plug. This setup completely isolates the pore fluid from the testing cell, ensuring electrical current to flow through the core sample for accurate resistivity measurements at in situ reservoir conditions. These end caps were attached to a smaller triaxial cell, also donated by Dr. Ali I. Mese.

The smaller triaxial cell functions similarly to the described larger triaxial cell in the previous section. One major difference, however, is that the axial stress is applied utilizing a uniaxial load frame. Specifically, the UNGI laboratory has an MTS Landmark Servo-Controlled Hydraulic test system capable of static and dynamic loading, though this works utilizes the static configuration. This systems large range of capabilities far exceed what is

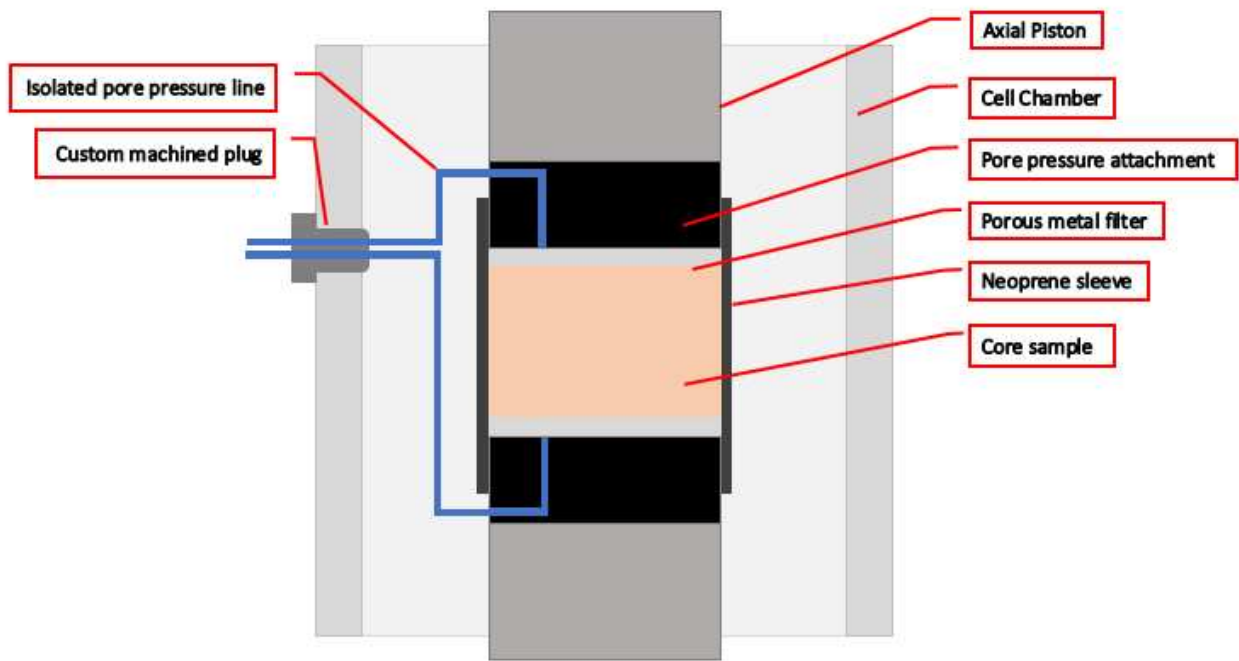


Figure 2.8: Schematic figure of the pore pressure isolation system design and implemented into the triaxial cell as to prevent electrical circumvention of the core sample.

required of our work, but we utilize the precision loading and vertical strain measurements.

The triaxial cell is assembled and placed in between the load cells grips, which applies a vertical force to simulate overburden stress on the rock sample tested. The confining pressure is applied similarly to the large triaxial cell in that a hydraulic pump pressurizes the inner cell volume. Again, a neoprene sleeve wraps the core sample as to prevent invasion of hydraulic fluid into the sample, or from pore fluid escaping out of the sample. The small triaxial cell disassembled can be seen in Figure 2.9. As mentioned, the new pore fluid end caps are the black end pieces attached to the axial pistons, as labeled in the Figure. The black anodizing was performed to electrically isolate the fluid system from the rest of the test cell. A 0.001" thick hard-anodize layer was applied to the whole end cap surface, effectively electrically isolating the core and pore fluid system from the pistons and cell chamber.

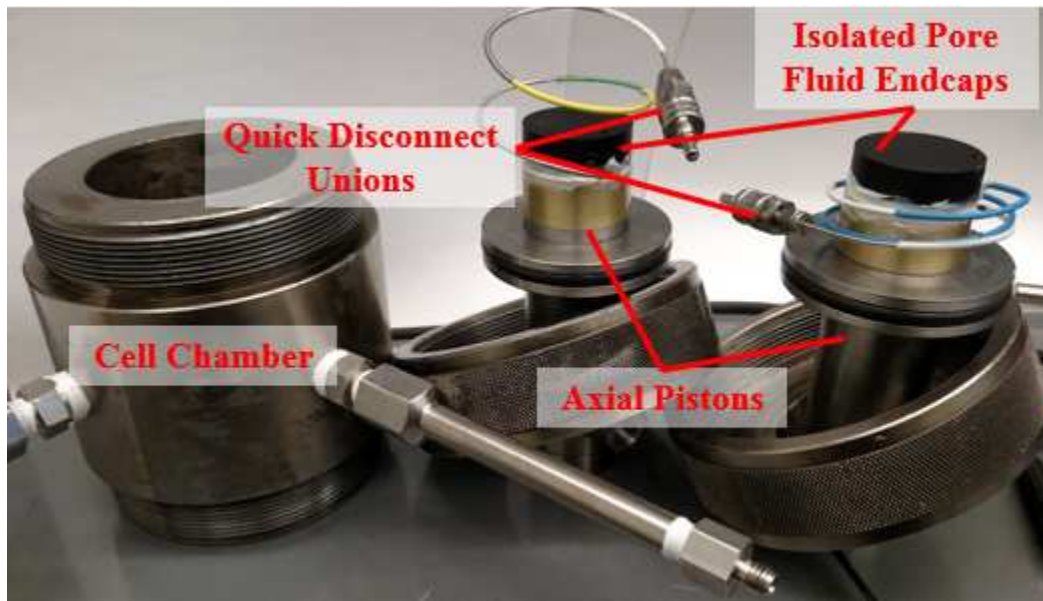


Figure 2.9: Disassembled small triaxial cell with pore pressure cap attachment. The end cap attachments are hard anodized as to prevent any electrical current from flowing through the liquid and into the cell chamber. This adds an additional level of electrical isolation to the core for accurate resistivity measurements.

2.2.2.1 Two Probe Triaxial Cell Resistivity Test Assembly

The experimental setup for two probe resistivity measurements for a one inch sandstone sample consists of three conductive epoxy electrode rings which circle the sample and are spaced at equal intervals along the sample length. The schematic electrode setup as well as the sandstone sample used in the calibration are shown in Figure 2.10. It should be noted that the two porous metal filters which are placed between the brass electrodes and the core are not seen in this picture. Two probe measurements are performed by sending an electrical current between any two electrodes; for example: zero to one, zero to two, etc. The known source current is then compared to the measured, the difference being the drop in voltage or resistance. For the osmotic pressure tests performed in this work the two probe resistivity measurement method is implemented for initial tests, though is deemed inaccurate after performing two shale tests and changed for the optimal four probe measurement.

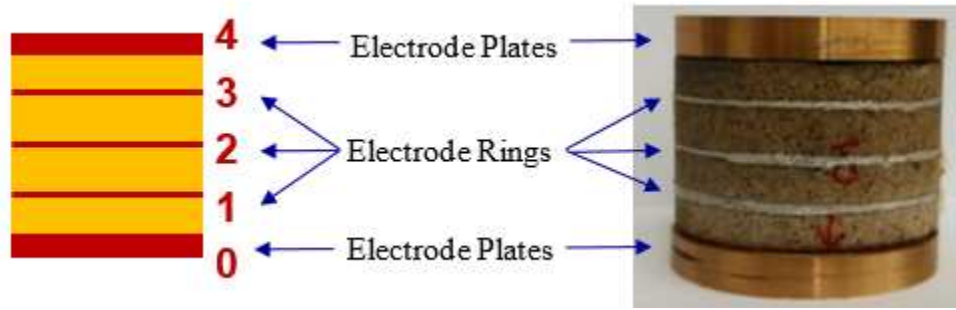


Figure 2.10: (Left) Schematic design of the electrode setup for two probe resistivity measurements. (Right) actual electrode setup for two probe resistivity sample used in the pore pressure penetration tests. It should be noted that for the pore pressure tests a set of porous metal filters would sit between the electrode plates and physical sample.

Modifications were required to the neoprene sleeve covering the core sample during the triaxial tests to isolate the core from the confining pressure fluid invasion. Wires are connected to the electrodes and passed through the neoprene sleeve via small openings. Multiple methods to effectively seal the wire openings were tested. The most consistent sealing method at high pressures was found to be using a combination of two epoxy adhesives to seal a hole just large enough for a wire to pass through. An automotive adhesive, Seal-All, is applied to the small openings made in the neoprene sleeve. Once the first layer epoxy is cured (approximately one hour), a second adhesive layering is applied, 3M Marine Adhesive Sealant, in two layers. The marine adhesive is then cured for twenty-four hours before assembling the triaxial cell. There are a total of five perforations required for the two probe measurements; two perforations for the brass plates, and three for the electrode rings which all need the described sealing procedure prior to the resistivity tests.

After a perfectly cylindrical and parallel sample has been obtained, an electrode setup is attached for measuring resistivity. The resistivity electrodes can then be attached to the outer surface of the core sample. To attach the electrodes for the resistivity measurements the following steps are performed:

- Cut four pieces of blue painters tape 0.235 in. wide and 5.0 in. in length and apply them evenly along the length of the core. There should be three 0.03 in. spaces between

each piece of tape.

- Apply conductive epoxy to the sample over the open areas, creating three rings of conductive epoxy.

- Attach a single wire strand to each epoxy ring (total of three), ensuring to cover the wire strand with additional conductive epoxy if required.

- Remove the blue painters tape from the core.

- Place the core into a sealed container to allow for the conductive epoxy to cure for one hour.

- Remove the core from the container and attach a 16 gauge wire lead to each electrode ring using conductive epoxy.

- Place the core into a sealed container to allow for the conductive epoxy to cure for four hours.

- Sand the neoprene sleeve around the areas where slots have been cut to match the wire leads attached to the core.

- Feed the wire leads through the slots in the neoprene sleeve from the inside out.

- Carefully push the core up into the neoprene sleeve, making sure to keep the wire leads aligned with their respective slots.

- Sandwich the core with two porous metal filters placed into the neoprene sleeve from either end.

- Feed the brass electrode wire lead through the respective slot on the top side of the neoprene sleeve, and carefully push the brass electrode into position above the top porous metal filter.

- Apply gasket sealant to the triaxial cell base piston shaft which the sample will be placed onto.

- Feed the wire lead attached to the piston brass plate through the respective slot on the bottom side of the neoprene sleeve, and carefully slide the neoprene sleeve with core assembly onto the piston.

- Directly apply automotive epoxy to the contact surface between the neoprene slots and wire protrusions.
- Wait one hour for the automotive epoxy to cure.
- Apply a thin layer of 3M Marine Grade Epoxy Sealant to the area surrounding each wire protrusion.
- Wait six hours for the epoxy sealant to cure.
- Apply a second thin layer of 3M Marine Grade Epoxy Sealant above the first layer
- Wait twenty-four hours for the epoxy sealant to cure.
- The testing cell can then be assembled.

2.2.2.2 Four Probe Triaxial Cell Resistivity Test Assembly

The experimental setup for four probe resistivity measurements consists of two source silver-silver chloride sintered electrodes and two identical potential electrodes. Two potential electrodes are embedded into the side of the sample at equal spacing, as illustrated in Figure 2.11. The two source electrodes are embedded in a similar manner, however they are embedded into the two parallel ends. The four probe measurements are performed by sending current through the two source electrodes, and the voltage measured between probes one and two. The difference in the known supplied current and the measured current in the sample is the resistance. This can then be used to determine the resistivity knowing the cross-sectional area of the sample and spacing distance between electrodes.

Unlike the two probe setup, there is no need to perforate the neoprene sleeve confining the shale sample. The hair like silver wires extending from the electrodes are run vertically down the shale sample under the neoprene sleeve and exits at the base. This minimizes potential leak paths for the high pressure confining fluids to enter the shale sample and contaminate the sample. A visual explanation of the four probe setup in the triaxial cell is depicted in Figure 2.5.

After a perfectly cylindrical and parallel sample has been obtained, an electrode setup is attached for measuring resistivity. The resistivity electrodes can then be attached to the

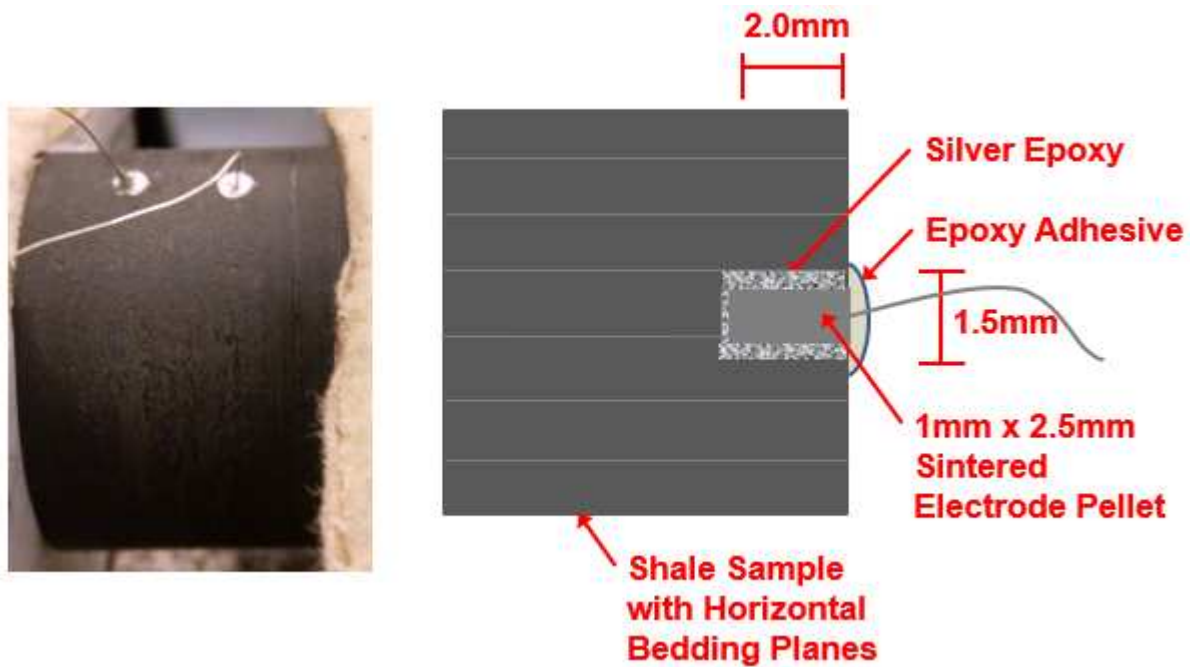


Figure 2.11: (Left) four probe setup of a shale sample showing the two potential electrodes embedded into the sample. (Right) schematic of the imbedded potential electrode to show depth of embedment and orientation to bedding lines.

outer surface of the core sample. To attach the electrodes for the resistivity measurements the following steps are performed:

- Measure out and mark on the sample every third of the sample length.
- Drill two 1.5mm diameter x 2.0mm long holes into the sample utilizing a drillpress.
- Take the two silver-silver chloride electrodes and coat them in a special silver-silver chloride conductive epoxy.
- Place the two electrodes into the two predrilled holes and ensure the conductive epoxy is cleaned around the edges.
- Place the core into a sealed container to allow for the conductive epoxy to cure for four hours.
- Sand the neoprene sleeve around the areas where slots have been cut to match the wire leads attached to the core.
- Feed the wire leads through the slots in the neoprene sleeve from the inside out.

- Carefully push the core up into the neoprene sleeve, making sure to keep the wire leads aligned with their respective slots.

- Sandwich the core with two porous metal filters placed into the neoprene sleeve from either end.

- Feed the brass electrode wire lead through the respective slot on the top side of the neoprene sleeve, and carefully push the brass electrode into position above the top porous metal filter.

- Apply gasket sealant to the triaxial cell base piston shaft which the sample will be placed onto.

- Feed the wire lead attached to the piston brass plate through the respective slot on the bottom side of the neoprene sleeve, and carefully slide the neoprene sleeve with core assembly onto the piston.

- Directly apply automotive epoxy to the contact surface between the neoprene slots and wire protrusions.

- Wait one hour for the automotive epoxy to cure.

- Apply a thin layer of 3M Marine Grade Epoxy Sealant to the area surrounding each wire protrusion.

- Wait six hours for the epoxy sealant to cure.

- Apply a second thin layer of 3M Marine Grade Epoxy Sealant above the first layer

- Wait twenty-four hours for the epoxy sealant to cure.

- The testing cell can then be assembled.

2.3 Data Collection

The resistivity data for preserved shale samples have been collected in this research during the pore pressure penetration tests. The two probe method of resistivity has been utilized throughout the first set of measurements. The resistance of the sample is directly measured, then the resistivity is calculated due to the interval length between electrodes and the cross-sectional area of the sample. The resistance measurement is performed using an ohm-meter,

sending a current through a set of electrodes and measuring the voltage drop between the same two electrodes. A detailed explanation of the other data acquisition systems is described in Appendix A.

2.4 Triaxial Cell Validation Test on Berea Sandstone Calibration Sample

Before performing the shale pore pressure penetration tests with resistivity measurements, a calibration test was performed on a Berea Sandstone sample of the same size to ensure the data acquisition system functions correctly. A one inch long Berea sandstone sample was prepared and three conductive epoxy rings spaced at quarter inch intervals were applied as represented in Figure 2.12. The triaxial cell is then assembled and placed into the temperature controlled chamber to be pressurized incrementally until reaching the final pressures of 9,333 psi axial, 6,000 psi confining, and 4,000 psi pore pressure states.

At the onset of the saline pore fluid injection of an eighteen percent KCl, resistance and acoustic data recordings were initiated. Resistance data was continuously recorded for the first 80 minutes at which point it was determined that the core was close to full saturation as the resistivity reached the lower limit as seen in the atmospheric tests. Electrical resistance was recorded for two hour, four hour, seven hour, and then for a final twenty hour intervals to ensure that the full saturation of the core had occurred. Acoustic data was recorded approximately every five minutes for the first eighty minutes, then every two hours for the remainder of the experiment. The resistivity data, accompanied by the corresponding compressional velocities are shown in Figure 2.12.

The general trend of the resistivity data is a downward, concave-up curve which reaches a lower limit at around 90 minutes. The first electrode to decrease in resistivity is the lowest pair, zero and one; next being electrodes zero and two. Timing of the initial resistivity drop is in coordination with the vertical spacing of the electrodes, the lower electrodes decrease first, followed by the higher electrodes. This shows a strong correlation relating the fluid migration to the observed decrease in resistivity. It is observed that the resistivity between the two brass plates, labeled zero and four, reaches the lower limit at 140 minutes, while

all other resistivity measurement reached lower limits at 80 minutes. From this trend, pore fluid injection should not stop until the brass plates lower limit is reached and Skempton's b-coefficient is evaluated.

From the resistivity data, it is evident that as the saturation level increases, represented by the downward trend of the resistivity, the compressional velocity increases. An increase in compressional velocity is directly related to an increase in density and bulk modulus of the sample. As seen in Figure 2.12, the plot of the primary wave velocity are the black circles which increase with saturation. The calculated compressional velocity range is between 3.750 and 3.775 km/s depending on the level of saturation. Comparing experimental compressional velocities to typical sandstone velocities of 2.5 to 3.5 km/s, it appears that compressional velocity values obtained in the experiments are slightly higher than anticipated. This increase could be due to the raised stress state on the rock, increasing the density and thus increasing the wave velocities.

The results from the pore pressure penetration sandstone validation tests indicate that the resistivity measurement acquisition setup in the larger triaxial cell works effectively. Clearly observed graphical correlations between saturation, compressional velocity, and resistivity provide valuable information for the osmotic pressure measurements on shale core samples. Further correlations are being studied to show the stress dependence of the resistivity and other measured parameters measured during the pore pressure penetrations tests on shale samples.

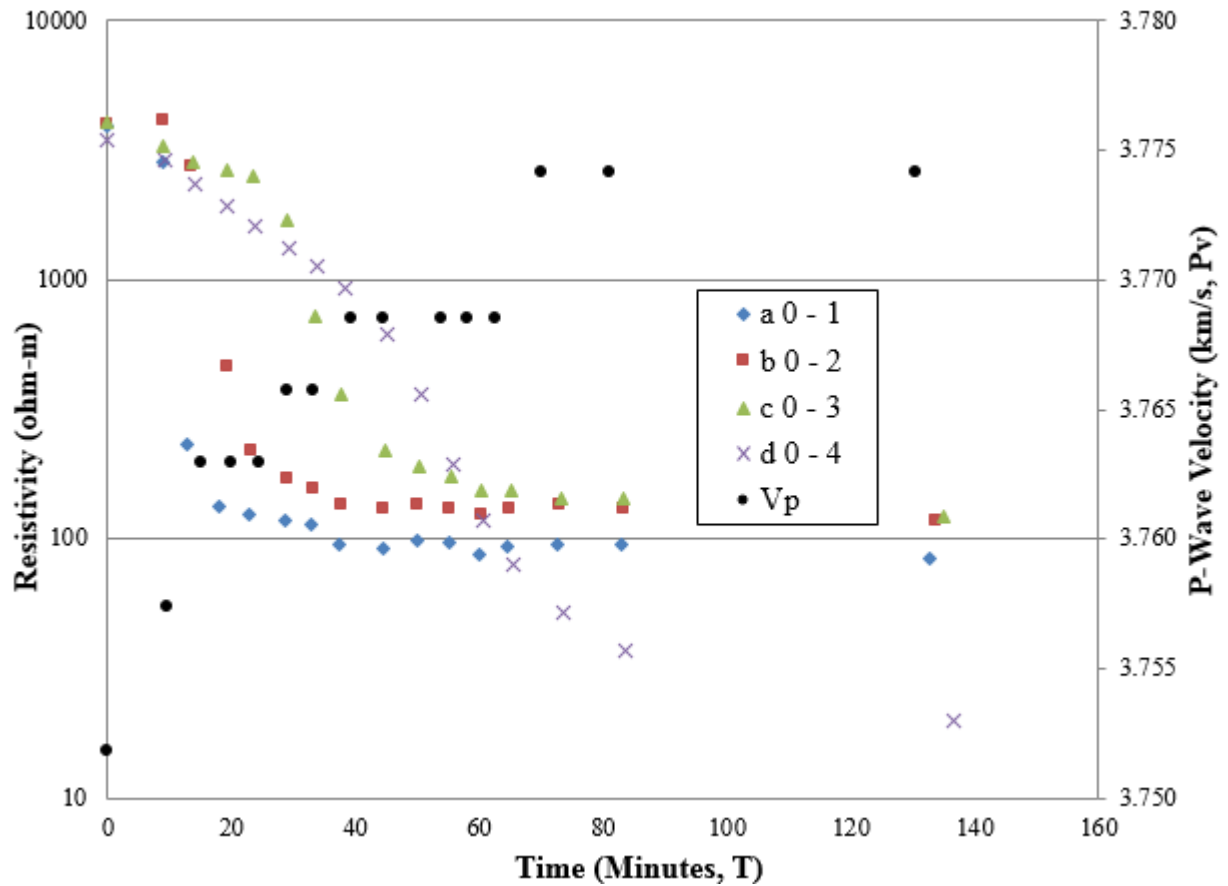


Figure 2.12: Triaxial resistivity calibration test performed on a Berea sandstone core sample with series resistivity vertical data and corresponding compressional velocity data. It is observed that as saturation increased through the core the resistivity decreased down to a lower limit. The P-wave velocity data agrees with the saturation as seen in the resistivity measurements.

CHAPTER 3

STRESS DEPENDENT ROCK PROPERTIES

The objective of this research, as previously stated, is to determine the stress dependency of the electrical properties of shale samples and to determine the accuracy of the tracking fluid migration utilizing resistivity measurements. This chapter is focused on examining the experimental results from Eagle Ford Shale (Texas), Bakken (North Dakota), Pierre Shale (Colorado), and Berea Sandstone (Ohio) samples tested in the laboratory. Relationships are observed between the rocks stress state, permeability, and resistivity. From the three samples only the Eagle Ford sample had ample well log data for field interpretations. The Berea Sandstone, Bakken and Pierre shale samples did not have log data. Much work has been performed characterizing the electrical properties of clean sandstone, however, not much work has been performed for this topic on shale rocks. This work is unique as clear relationships are observed between resistivity, stress state, permeability, and pore geometry changes.

3.1 Selection of Core Samples for Testing

The outcrop core samples of the Berea Sandstone and Pierre Shale were directly cut and ground by a subcontractor, Kocurek Industries. Therefore, there is no log-based sample selection for these formations. The initial tests incorporating resistivity for the shale osmosis were performed on Eagle Ford Shale samples. Extensive log data and core samples were available for the Eagle Ford wells through the UNGI CIMMM Consortium members. The core samples utilized for the Eagle Ford tests were selected after a full range of well logs were interpreted.

Well logs examined for the selection of the Eagle Ford sample are Gamma Ray (GR), formation resistivity, Spontaneous Potential (SP), spectral Gamma Ray (potassium, thorium

and uranium curves), Total Organic Carbon (TOC), density-porosity, neutron-porosity, volumetric mineralogy (EDAX), pore pressure, acoustic velocities from dipole sonic logs, in situ stress magnitudes derived from the sonic velocities and pore pressure measurements, and geomechanical properties such as dynamic Young's Modulus and Poisson's ratio. The selection and analysis was largely conducted by Padin (2016). Computer Tomography (CT) scans of the Eagle Ford cores were performed before the osmosis tests to aid in the selection of the core to identify any natural fractures and after the osmosis test to identify any fractures created from the tests.

Three core plugs were taken and preserved from a one foot sample (sample #GZ-6), which was cored from the upper Eagle Ford in Gonzales County, Texas. Due to the three plugs being cored in the laboratory from the same one foot sample, it is assumed they contain the same mineralogical composition and fabric, if there are slight differences they will be due to small heterogeneities. These samples were used for geomechanical analysis to determine compressive strengths, permeability measurements, and for the osmosis test.

The depth locations of the Eagle Ford samples were selected due to the presence of fracturing, as a non-fractured rock is required for testing, and the described analysis of the log data. Selection of testing parameters pertaining to stress state were selected due to analysis of the in situ stress state and permeability as determined from the log interpretation. The selection of testing parameters for the Bakken, Pierre, and Berea samples were selected from extensive known literature on these formations.

3.1.1 Formation Specific Core Sample Inventory

The selection of samples for the Eagle Ford formation is far more extensive than the Bakken, Pierre, or Berea Sandstone formations. Also available to the consortium were a few core samples from the Vaca Muerta formation in Argentina. However, no resistivity analysis was performed for this formation. Because of the abundance of the samples and corresponding log data, the Eagle Ford formation has been the focus of this study. As shown in Table 3.1, the number of samples available from the Eagle Ford, along with the other

formation samples were utilized in this study.

3.1.2 Eagle Ford Sample Porosity, Pore Size Distribution and Geometry

One of the key reservoir properties to understand is porosity; when compared with permeability can be a great aid in determining rock texture and fabric. The pore structure which holds the porosity and creates the flow or permeability of the rock is dependent on the deposition of that rock. In the Eagle Ford shale, the porosity is most influenced by grain shape, sorting and packing (Ahr 2011). However, due to the large volume of organic content, catagenesis is very influential on the porosity; catagenesis being the diagenesis of organic matter (Flugel 2010).

Reservoir permeability is controlled by the three key factors: pore volume, mean size of pore throats, and connectivity (Flugel and Munnecke, 2010). The pore volume controls the volume of fluid contained within the rock. The mean size of pore throats characterizes the cross-sectional area which flow can occur through; if the mean size is smaller, there are more constrictions which would decrease permeability. Lastly, the connectivity is representative of the number of paths for flow to occur through the core; conversely, the more open pathways for flow represents greater permeability.

Analysis of the pore size distribution and pore geometry is attempted to be performed using QEMSCAN, petrographic thin sections and FE-SEM analysis performed by Padin (2016). The nature of the shale formations, better classified as mudrocks, are very fine grained nano-pore size rocks. The resolution of the QEMSCAN did not allow for accurate imaging or interpretation of the pores, nor did the thin section analysis as the interpretation of SE2 images is challenging due to damages to the nano pore structure from milling the cores.

3.1.2.1 Determination of Eagle Ford Sample Absolute Porosity

The determination of absolute porosity for three Eagle Ford samples #GZ-5, #GZ-6, #GZ-7 was performed. The calculation of absolute porosity is the fractional volume (a value of 1) minus the ratio of bulk density (ρ_{bulk}) and the density of solid grains (ρ_{solids}), as

Table 3.1: Set of cored samples available for experimental use from the Eagle Ford, Vaca Muerta, Bakken, and Pierre shale formations.

Formation	Well #	County, State	Field	Sample #	Core Depth (Ft)		Log Depth (Ft)	
					Base	Top	Base	Top
Eagle Ford	1	Gonzales, TX	Confidential	#GZ-1	Confidential			
				#GZ-2	Confidential			
				#GZ-3	Confidential			
				#GZ-4	Confidential			
				#GZ-5	Confidential			
				#GZ-6	Confidential			
				#GZ-7	Confidential			
				#GZ-8	Confidential			
				#GZ-9	Confidential			
				#GZ-10	Confidential			
				#GZ-11	Confidential			
				#GZ-12	Confidential			
	2	La Salle, TX	Confidential	#LS-1	Confidential			
				#LS-2	Confidential			
				#LS-3	Confidential			
				#LS-4	Confidential			
				#LS-5	Confidential			
	Outcrop	Del Rio, TX	Confidential	#OU-1	Confidential			
			Confidential	#OU-2	Confidential			
			Confidential	#OU-3	Confidential			
Vaca Muerta	LJE-1010	Neuquen, Argentina	Loma Jarillosa Este Block	#VM-1	3,102.50		-	-
Bakken	1	North Dakota	Confidential	#BK-1	Confidential			
Pierre	Outcrop	Colorado	-	#PI-1	-	-	-	-

displayed in Equation 3.1. Before the absolute porosity was determined, the Dean-Stark extraction with toluene was performed to extract hydrocarbons from the samples. It should be noted that exposure to toluene is dangerous and must be avoided as toluene is a neurotoxin. Cleaning of the cores is performed in an air circulation cabinet as to prevent inhalation of the toluene. A more in depth description of the Dean-Stark extraction method is detailed in Appendix A. Two methods of porosity measurements were performed, being the pycnometer method and using XRD weight percentages.

$$\phi_{abs} = 1 - \frac{\rho_{bulk}}{\rho_{solids}} \quad (3.1)$$

First, the mercury bulk density is determined utilizing a high pressure pump to fill the open space surrounding the test sample. This methods and procedures are explained in Appendix A.1.1.1. The results of the mercury bulk density are listed in Table 3.2. For the pycnometer method, an unknown sample volume is dried and weighed, then placed into the pycnometer for the volume to be determined. The exact procedure and internal workings of the pycnometer are detailed in Appendix A.1.1.2. Knowing the weight and volume, density can be determined from the ratio of the weight to volume. The second method to determine porosity can be calculated using XRD measurements of crushed samples. Determining the weight mineral percentage for each sample, the grain density can then be calculated knowing the original volume of the sample. Results from the XRD analysis for grain density, with the difference between the pycnometer method are displayed in Table 3.3. From the grain density results, absolute porosity can then be determined as listed in Table 3.4.

Table 3.2: Bulk density of Eagle Ford Shale samples utilizing the mercury bulk density method.

Sample #	Sample wt. (g) After Toluene Wash and Drying	Mercury Bulk Volume (cc)	Bulk Density (g/cc)
#GZ-5	5.799	2.10	2.76
#GZ-6	17.614	6.93	2.54
#GZ-7	18.907	7.39	2.56

Table 3.3: Results of XRD grain density and pycnometer grain density methods with displayed difference between the two methods.

Sample	Grain Density (g/cc) from XRD	Grain Density (g/cc) from Pycnometer	Difference (%)
#GZ-5	2.647	2.664	1.719
#GZ-6	2.719	2.722	0.297
#GZ-7	2.702	2.690	1.216

Table 3.4: Absolute porosity calculation utilizing both methods of grain density calculation.

Sample #	Bulk Density (g/cc)	Porosity XRD (frac.)	Porosity Pycnometer (frac.)	Difference (%)
#GZ-5	2.760	0.043	0.036	4.2
#GZ-6	2.540	0.066	0.067	6.5
#GZ-7	2.560	0.053	0.048	5.2

3.1.2.2 Eagle Ford #GZ-6 Pore Distribution

The porosity measurements as seen in the above tables present good comparisons between the different samples, though the general porosity does not accurately represent the complex pore structure which is present in mudrocks (Kuila 2013). Porosity distribution in mudrocks are claimed by King et al. (2015) to follow two distinct patterns. The first pattern is that two-thirds of the porosity follows a wide power-law distribution, and is strongly linked to non-organic material. The second pattern would be the resulting one-third of porosity consists of interparticle organic matter pores which are smaller than three nanometers. It was found by Rine et al. (2010) that the pore diameters in the Eagle Ford range between 10-30nm. Loucks et al. (2012) compared the porosity of mudrocks to be similar to that of carbonates and coarse grained siliciclastics. The mudrocks contain similar shaped pores, though they are smaller in overall size and contain organic porosity. A complete analysis of the varying porosities observed in the Eagle Ford samples is detailed by Padin (2016).

3.1.2.3 Eagle Ford #GZ-6 Mineralogy and Organic Matter Composition

Eagle Ford sample #GZ-6 is cored from the upper Eagle Ford, an organic-rich, laminated, pyritic and fossiliferous dark gray marine calcareous marl interval (Padin 2016). The mineralogy of this sample is comprised of 63.7 wt. % calcite, 12.45 wt. % quartz, 12.45 wt. % illite/mica, 4.79 wt. % plagioclase, and 1.63 wt. % pyrite. From Rock-Eval pyrolysis it is determined that the sample contains 4.24 wt. % TOC, 0.39 mg HC/g of rock (S1), hydrocarbon generative potential (S2) of 10.74 mg HC/g rock and a carbon dioxide content of 0.34 mg CO_2 /g rock. SEM images show that the rock matrix is very tight and dominated by carbonates. For a complete analysis of the mineralogy the readers are recommended to Padin, (2016).

3.1.2.4 Geomechanical Property Determination

Determination of the geomechanical properties of the rock samples are essential to understand the correlation between the stress state and the resistivity. The general understanding of stress and the effects of stress on geomechanical properties of the rock like Young's modulus, Poisson's ratio, permeability, and other properties show how influential stress is on rock properties and behavior. Determination of the rock geomechanical properties used in this work is imperative; five preserved samples from various depths of the Eagle Ford were tested to determine the geomechanical properties.

The cores used in the geomechanical study were two to three inches in length, and one and a half inch in diameter. The optimal length to diameter ratio for geomechanical studies is 2:1 (ASTM-D-7012, 2004). For the osmosis tests the low permeable shales were shortened in length due to the duration of the tests for complete saturation to occur, because for longer cores the time frame was deemed too long and impractical. Preparation of the sample had to be precise, first the cores parallel ends had to be within ± 0.0004 inches of each other. If the parallel ends were not prepared accurately to the specifications concentrated stresses would occur at the high side due to the axial compression and skew the results. This is true

for the geomechanical study and for the osmosis tests.

The samples were placed into a triaxial cell, between two flat, un-grooved, stainless-steel axial pistons. A neoprene sleeve covered both the sample and a portion of the pistons as to seal the confining fluid from the sample. Machined and attached in the base of each side of the axial piston two, 1 MHz transducers (Olympus-NDT 2006) ultrasonic velocity measurement sender and receiver are epoxied in place to create both compressional and shear waves for dynamic measurements. Strain gages are attached to the side of the core to observe any lateral strain. Vertical stress and strain is controlled and measured by the MTS servo-controlled hydraulic load frame. Once the test is setup, confining and axial pressure were increased while stress, vertical strain, lateral strain, and velocity measurements are simultaneously recorded. Strain is increased at a constant rate of $+1 \times 10^{-5}$ inches per second. The strain rate is maintained past the sample failure, until post-failure equilibrium is achieved at the final residual strength.

Results from the experimental geomechanical determination of static Young's modulus, Poisson's ratio and compressive strength are shown in Table 3.5. Young's modulus is determined from the slope of the stress-strain graph using the average method as described in ASTM-D-7012, 2004. Poisson's ratio is determined by dividing the axial deformation by the radial deformation and compressive strength is the maximum stress before the rock fails. Graphical representation of the stress strain curves, both axial and lateral, for samples #2, #3, and #4 are plotted in Figure 3.1.

From the results, it can be observed that the samples with higher clay content, being #1, #2, and #3 exhibit more ductile tendencies as there is greater deformation and higher stresses before failure. Samples #2 and #4 show a sharp failure point, followed by a rapid reduction in strength; where as sample #3 has a less defined failure point, and less strain softening. Further analysis of the geomechanical properties is performed utilizing Mohr's circle to determine the failure criteria for samples #3 and #4 as shown in Figure 3.2. Results from the failure criterion are standard to ductile mudrocks as low cohesion and ultimate

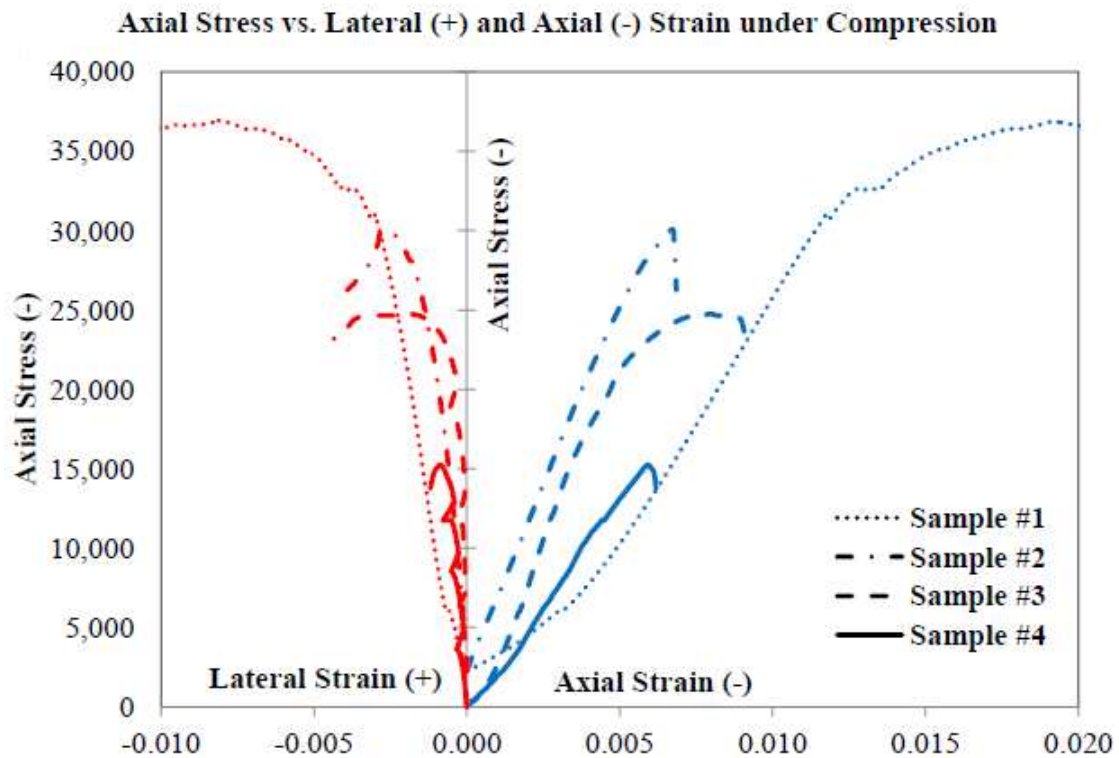
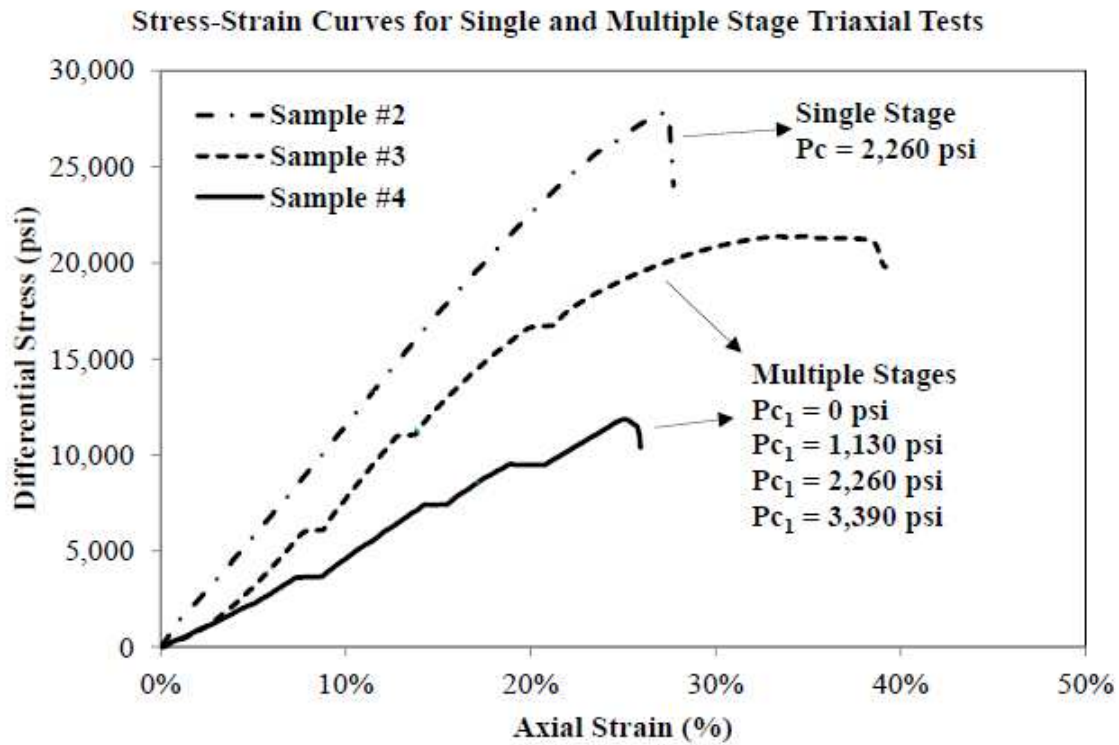


Figure 3.1: Stress-strain curves (top) as well as stress-lateral/axial strain curves (bottom) for samples Eagle Ford samples #1, #2, #3, and #4 (Padin 2016). Samples #3 and #4 were exposed to varying stress state conditions where as samples #1, #2, and #5 were at a single stress condition.

Table 3.5: Results from geomechanical determination: Static Young's modulus, Poisson's Ratio and Compressive Strength. Samples 3 and 4 enabled the calculation of the failure envelope using Mohr's Circle due to the varying stress conditions.

Sample Number	Bulk Density (g/cc)	Confining Pressure (psi)	Compressive Strength (psi)	Young's Modulus ($\times 10^6$ psi)	Poisson's Ratio (Unitless)
1	2.57	2,260	36,955	3.20	0.27
2	2.56	2,260	30,082	4.83	0.26
3	2.56	0	6,060	4.30	0.09
		1,130	12,120	4.45	0.15
		2,260	18,925	4.92	0.25
		3,390	24,764	4.10	0.30
4	2.45	0	3,626	2.20	0.12
		1,130	8,549	2.50	0.21
		2,260	11,782	2.88	0.26
		3,390	15,246	2.58	0.32
5	2.36	3,390	17,852	1.12	-

compressive strength (UCS) values are observed.

Lastly, dynamic properties are measured from the propagation of primary and shear waves in the axial direction only. The dynamic measurements aid in the interpretation of the stress dependent rock parameters. Changes in wave velocity are correlated to changes in porosity and water saturation (ASTM D2845-05, 2014). Other application of the sonic measurements are identification of natural fractures, being the main form of anisotropy in the rocks (Tutuncu et al. 2011). Results from the dynamic measurements for samples #1, #2, and #3 are presented in Table 3.6 and Table 3.7. The increase in stress as seen in the results of sample #3 correlates to an increase in the bulk modulus, Young's modulus, shear modulus, and Poisson's ratio. This change in the rock geomechanical properties is a clear sign of geometric changes in the pore structure, (Josh et al. 2012) which would relate to a change in resistivity.

3.2 Stress Dependent Permeability of the Upper Eagle Ford Samples

For each of the samples used in the osmotic pressure tests, the permeability is determined utilizing three separate methods, a steady state constant pressure-gradient permeability test

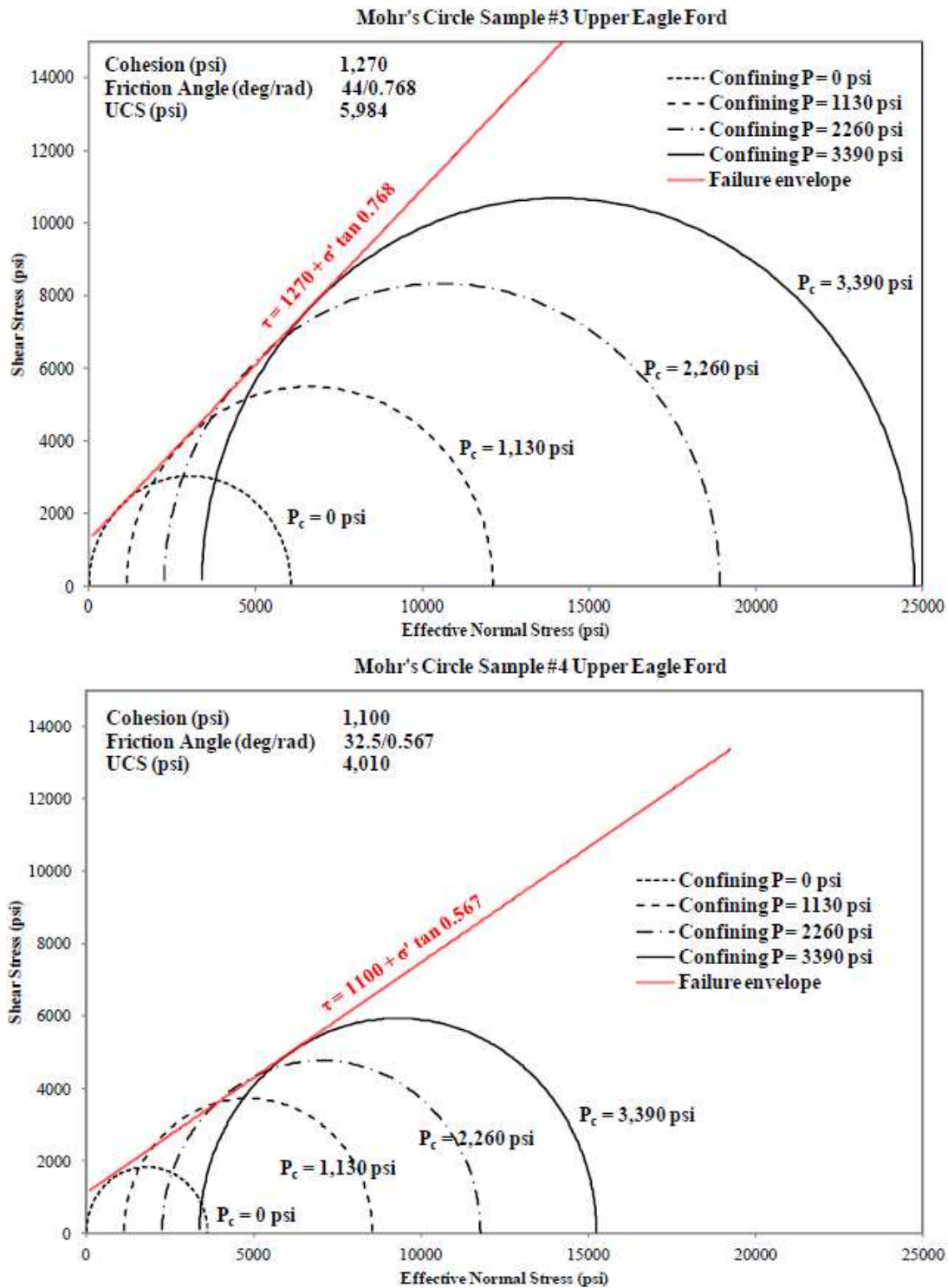


Figure 3.2: Failure criteria of samples #3 (top) and #4 (bottom) determined through the use of Mohr's circle. Various plugs at the same depths were tested at varying confining pressure for the parameters required to use for Mohr's plots. From interpretation of the plots cohesion, friction angle, and ultimate compressive strength are determined.

Table 3.6: Dynamic measurements taken simultaneously throughout triaxial stress strain tests.

Sample #	Bulk Density (g/cc)	Confining Pressure (psi)	Axial Pressure (psi)	Acoustic Velocity (ft/s)	
				Compressional (P)	Shear (S)
1	2.57	2,260	1,000	16,276	9,224
			11,000	18,401	9,815
2	2.56	2,260	2,260	15,901	8,956
			12,600	17,726	9,904
3	2.52	0	1,000	16,304	9,694
		1,130	6,000	17,381	10,023
		2,260	11,000	18,466	10,266
		3,390	16,000	19,373	10,438

Table 3.7: Extension of Table 3.6 displaying the results for the modulus determinations.

Extension of Table 3.6 to display modulus results				
Sample #	Bulk Modulus	Young's Modulus	Shear Modulus	Poisson's Ratio
	(*10 ⁶ psi)	(*10 ⁶ psi)	(*10 ⁶ psi)	(Unitless)
1	5.25	7.45	2.95	0.26
	7.28	8.69	3.34	0.30
2	5.03	7.02	2.77	0.27
	6.33	8.62	3.38	0.27
3	4.77	7.83	3.19	0.23
	5.71	8.54	3.41	0.25
	6.81	9.14	3.58	0.28
	7.81	9.59	3.70	0.30

performed with both nitrogen and brine, as well as a pressure-pulse decay with nitrogen. Gas adsorption and the Klinkenberg gas slippage effect are accounted for during the gas permeability tests. The relatively fast transient permeability test can negate the effects of nitrogen adsorption, where as the steady-state method which takes up to two days must account for nitrogen adsorption. The results of the permeability measurements taken during the consolidation of the shale samples shows the inverse relationship between permeability and stress, in that as stress increases the permeability decreases. The decrease in permeability represents a change in the pore geometry of the rock and would consequently affect the measured resistivity as well.

For the permeability tests, one inch in length by one and a half inch diameter shale samples were prepared as previously described. The shortened samples are used due to the long duration to fully saturate such a low permeable sample. The stress dependent permeability effect was shown and measured during the consolidation of the shale samples to reservoir conditions. The consolidation and permeability measurements took up to about twenty days to complete per sample. This is due to the length of the procedure for the permeability measurements and to ensure stabilized conditions occur for each increase in the stress state. For each stress increase, steps of 500 psi per stage, two to three steady-state measurements and one or two pulse-decay measurements have been performed. Figure 3.3 is an example of one of the permeability tests for the Eagle Ford shale sample. Permeability is measured in similar fashion for the Bakken and Pierre shale samples as well, though is not described in detail as it the same procedures are followed.

3.2.1 Pulse-Decay Permeability Measurements

Pulse-decay measurements are taken by placing a core between two reservoirs of known volume and pressure, setup within the triaxial cell in the UNGI laboratory. Correctly setting up the core, as well as assembling the triaxial is detailed in Appendix A. Pressure in the upstream reservoir, for this test the pressure at the base of the core is considered upstream, is increased and equilibrium is achieved. Initial nitrogen injection started at 200 psi injection pressure and 200 psi effective stress. The injection pressure and stress are increased while maintaining an effective stress of 200 psi until 1,700 psi confining stress and 1,500 psi pore pressure is achieved. Due to the high pore pressures ($P_p > 1,000$ -1,200 psi) in this tests it should negate the Klinkenberg effect on the measured gas permeability.

With equilibrium achieved across the sample the pulse-decay permeability test can then begin. The upstream side of the sample is isolated from the gas reservoir, then pressure is increased until a difference between the pore pressure and reservoir pressure is greater than 1,000 psi. This increased reservoir pressure is then quickly released into the sample. The decay of the upstream reservoir pressure and the increase in the downstream pressure are

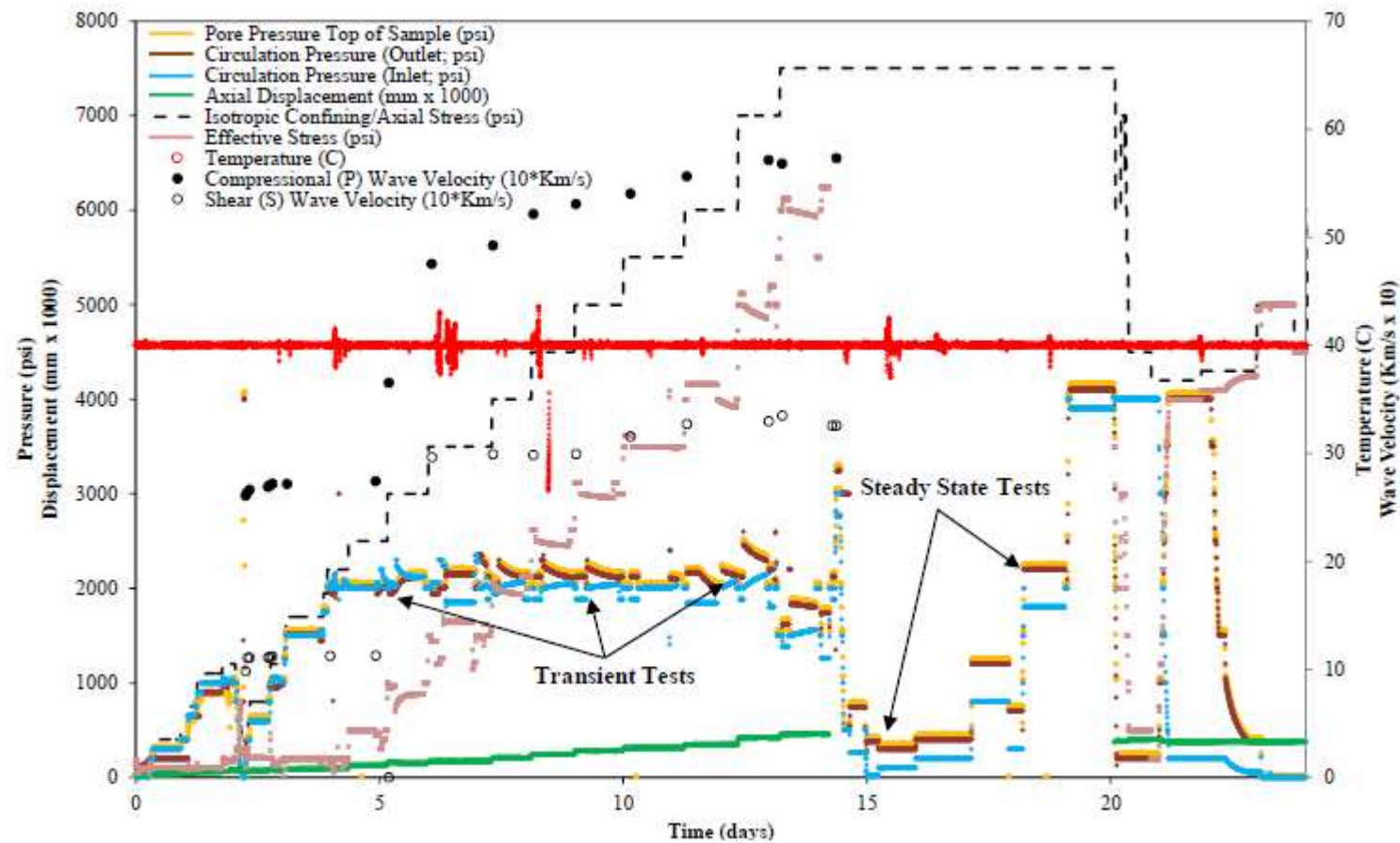


Figure 3.3: Results from an Upper Eagle Ford sample for consolidation and permeability measurements. Simultaneous measurements of pore pressure at the top of the sample (downstream pore pressure), circulation pressure (upstream pressure), axial displacement (vertical strain perpendicular to bedding), confining stress, effective stress, temperature, and wave velocities (Padin 2016).

measured. From this, the permeability of the sample can then be determined. This test is performed multiple times at different downstream pressure conditions for accurate findings and isolating if there are any effects of the gas slippage.

The equation for an exponential curve can describe the decline in pressure (ΔP) from the initial pressure offset (ΔP_o), as seen in Equation 3.2 (Hsieh et al. 1981). Plotting the results of the pulse-decay enables the calculation of the slope of the pressure decay (α) Davies and Holditch (1998), over the given time (t) which the sample was exposed. With (α), the permeability can then be calculated as seen in Equation 3.3, knowing the length of the core (L), compressibility of the upstream reservoir (c_u), compressibility of the downstream reservoir (c_d), area (A), and dynamic viscosity (μ) of the nitrogen gas (0.0184 mPas at the pressure and temperature defined). Results for the Upper Eagle Ford pulse-decay nitrogen permeability are shown in Table 3.8.

$$\frac{\Delta P}{\Delta P_o} = e^{-\alpha t} \quad (3.2)$$

$$k = \alpha \frac{\mu L c_u c_d}{A(c_u + c_d)} \quad (3.3)$$

From the pulse-decay permeability results it is observed that the permeability decreases along an exponential curve with increasing effective stress as can be seen in Figure 3.4, with the representative exponential equation for the fitted trendline. There is an observed abrupt decrease in the measured permeability between 1,000 psi to 1,500 psi. The fast decrease in permeability is attributed to the closure of microfractures within the rock matrix, dramatically decreasing the area for fluid flow to occur. Once effective stress rises above 4,000 psi the permeability ranges from 10 nD to 4 nD, being representative to the permeability at reservoir in situ stresses.

3.2.2 Steady-State Nitrogen Permeability

Steady-state nitrogen permeability tests are performed by placing the rock sample under a constant pressure gradient. Pressure and fluid flow equilibrium occurs across the core

Table 3.8: Results of the Upper Eagle Ford pulse-decay nitrogen permeability for varying effective stresses.

Parameter	$\sigma_{eff} = 0.2\text{ksi}$	$\sigma_{eff} = 0.5\text{ksi}$	$\sigma_{eff} = 1.0\text{ksi}$	$\sigma_{eff} = 1.5\text{ksi}$	$\sigma_{eff} = 2.0\text{ksi}$
Area, A (m ²)	1.14E-03	1.14E-03	1.14E-03	1.14E-03	1.14E-03
Length, L (m)	0.0257	0.0257	0.0257	0.0257	0.0257
Viscosity, μ (mPas)	0.0184	0.0184	0.0184	0.0184	0.0184
Volume Upstream Reservoir, $V_{ur}(\text{cc})$	90.14	82.10	74.40	98.76	113.29
Volume Downstream Reservoir, $V_{dr}(\text{cc})$	78.33	84.33	87.24	63.24	51.76
Compressibility Upstream, $c_u(\text{m}^3/\text{Pa})$	6.464E-12	5.965E-12	5.487E-12	7.000E-12	7.902E-12
Compressibility Downstream, $c_d(\text{m}^3/\text{Pa})$	5.991E-12	6.365E-12	6.546E-12	5.053E-12	4.338E-12
Pressure Decay Slope $\alpha_{hr}(1/\text{hr})$	0.653	0.517	0.410	0.152	0.126
Pressure Decay Slope $\alpha_s(1/\text{s})$	1.81E-04	1.44E-04	1.14E-04	4.22E-05	3.50E-05
Permeability, k (m ²)	2.34E-19	1.83E-19	1.41E-19	5.14E-20	4.06E-20
Permeability, k (nD)	237	186	143	52	41

Parameter	$\sigma_{eff} = 2.5\text{ksi}$	$\sigma_{eff} = 3.0\text{ksi}$	$\sigma_{eff} = 3.5\text{ksi}$	$\sigma_{eff} = 4.0\text{ksi}$	$\sigma_{eff} = 5.0\text{ksi}$	$\sigma_{eff} = 6.0\text{ksi}$
Area, A (m ²)	1.14E-03	1.14E-03	1.14E-03	1.14E-03	1.14E-03	1.14E-03
Length, L (m)	0.0257	0.0257	0.0257	0.0257	0.0257	0.0257
Viscosity, μ (mPas)	0.0184	0.0184	0.0184	0.0184	0.0184	0.0184
Volume Upstream Reservoir, $V_{ur}(\text{cc})$	125.04	134.32	2.27	1.03	3.22	3.16
Volume Downstream Reservoir, $V_{dr}(\text{cc})$	41.38	33.29	2.26	3.52	1.59	10.09
Compressibility Upstream, $c_u(\text{m}^3/\text{Pa})$	8.6632E-12	9.208E-12	1.007E-12	9.293E-13	1.054E-12	1.054E-12
Compressibility Downstream, $c_d(\text{m}^3/\text{Pa})$	3.692E-12	3.189E-12	1.258E-12	1.336E-12	1.122E-12	1.122E-12
Pressure Decay Slope $\alpha_{hr}(1/\text{hr})$	0.094	0.077	0.163	0.153	0.099	0.029
Pressure Decay Slope $\alpha_s(1/\text{s})$	2.61E-05	2.14E-05	4.53E-05	4.25E-05	2.75E-05	8.06E-06
Permeability, k (m ²)	2.80E-20	2.10E-20	1.05E-20	9.66E-21	6.20E-21	1.82E-21
Permeability, k (nD)	28	21.3	10.6	9.8	6.3	1.8

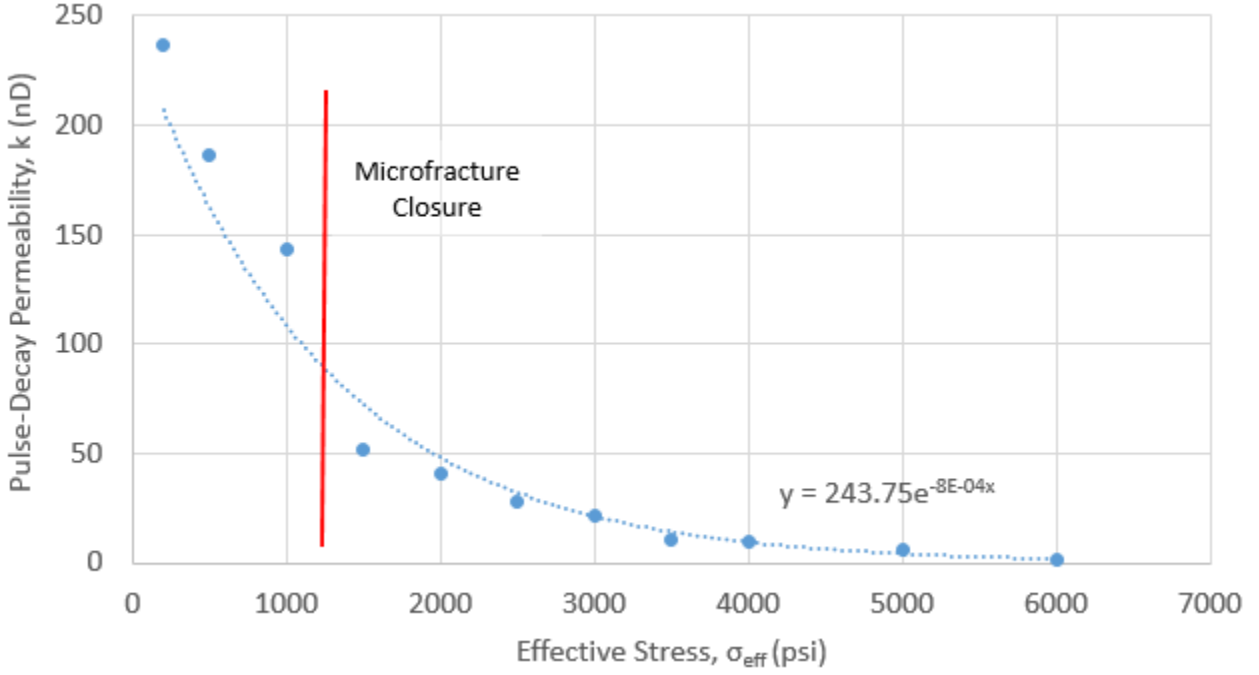


Figure 3.4: Dependence of pulse-decay determined permeability on effective stress of the sample. It is observed that the permeability decreases with increasing effective stress in a power function trend. Also, the sharp decrease between 1,000 psi to 1,500 psi represents the closure of microfractures.

between the upstream and downstream reservoirs and steady state is reached, consequently the mass flow rate is constant. To calculate permeability from this data Darcy's Law, corrected for gas slippage, is utilized as indicated in Equation 3.4. The derivation of this equation is out of the scope of this work, for a detailed explanation, the reader is recommended to see Padin (2016). (C_1) and (C_2) are unit conversion constants, (P_1) and (P_2) are the injection and outflow absolute gas pressures, respectively, (q_r) is the mass flow rate, and (z) is a compressibility factor.

$$k_g = \frac{2C_2\mu P_r q_r z_m}{C_1 z_r G_f (P_1 - P_2)(P_1 + P_2)} \quad (3.4)$$

To determine the effects of gas slippage the measured permeability must be plotted inversely to the mean pore pressure. The Klinkenberg gas slippage factor (b) is equal to the ratio of the slope of the measured permeability to the inverse of the mean pore pressure

and the y-intercept of the same graph, (k_{∞}) . This can be displayed by Equation 3.5, and has been presented in Figure 3.5. Results from the steady-state permeability are shown in Figure 3.6 and Figure 3.7.

$$k_g = k_{\infty} \left(1 + \frac{b}{P_m} \right) \quad (3.5)$$

The results from the steady-state permeability measurements show that the permeability decreases with the increasing effective stress. This relation shows that as the effective stress increases, the nanopores and pore throats constrict and can even cutoff flow if completely closed. Once the rock samples are exposed to reservoir pressures ($\sigma_{eff} > 3,000psi$) the permeability reaches a lower limit ranging from 15 to 2 nano-Darcy. A similar large decrease in permeability is observed again between effective stress rates of 1,000 psi and 1,500 psi, which is accredited to the closure of microfractures as shown in Figure 3.8.

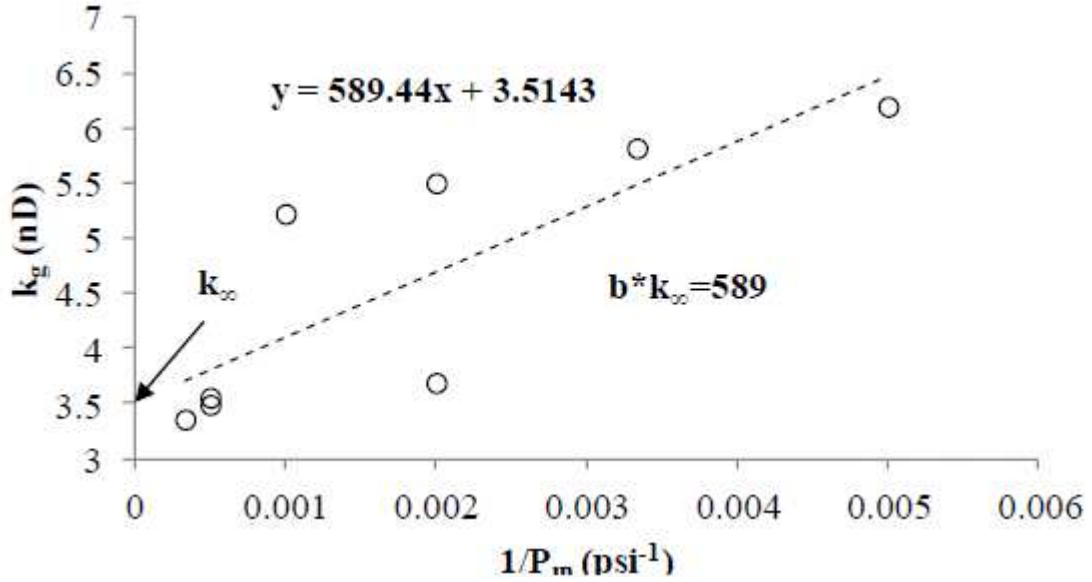


Figure 3.5: Calculation of the Klinkenberg gas slippage factor (b) from the plot of the measured permeability from multiple pore pressures and the inverse of those pore pressures. The Y-intercept is representative of (k_{∞}) and the slope is equal to $(b * k_{\infty})$ (Padin 2016).

$\sigma_{\text{eff}}=200$ psi				$\sigma_{\text{eff}}=500$ psi			
Parameter	Values			Parameter	Values		
Area (m ²)	1.14E-03			Area (m ²)	1.14E-03		
Length (m)	0.0257			Length (m)	0.0257		
Viscosity μ_f (mPas)	0.0184			Viscosity μ_f (mPas)	0.0184		
Downstream Flow Rate (cc/day)	40.168			Downstream Flow Rate (cc/day)	33.236		
Downstream Flow Rate (m ³ /s)	4.65E-10	1.59E-13		Downstream Flow Rate (m ³ /s)	3.85E-10	1.59E-13	
	psi	Pa	atm		psi	Pa	atm
Upstream P _p	2060	14203700	140.17476	Upstream P _p	2060	14203700	140.17476
Downstream P _p	1940	13376300	132.00924	Downstream P _p	1940	13376300	132.00924
(p ₁ ² -p ₂ ²)/Length	8.88E+12			(p ₁ ² -p ₂ ²)/Length	8.88E+12		
Permeability (mD)	2.26E-19			Permeability (mD)	1.87E-19		
Permeability (nD)	229			Permeability (nD)	189		
Effective Stress (psi)	200			Effective Stress (psi)	500		
ΔP_p (Upstream-Downstream)	120			ΔP_p (Upstream-Downstream)	120		

$\sigma_{\text{eff}}=1000$ psi				$\sigma_{\text{eff}}=1500$ psi			
Parameter	Values			Parameter	Values		
Area (m ²)	1.14E-03			Area (m ²)	1.14E-03		
Length (m)	0.0257			Length (m)	0.0257		
Viscosity μ_f (mPas)	0.0184			Viscosity μ_f (mPas)	0.0184		
Downstream Flow Rate (cc/day)	24.725			Downstream Flow Rate (cc/day)	20.554		
Downstream Flow Rate (m ³ /s)	2.86E-10	1.59E-13		Downstream Flow Rate (m ³ /s)	2.38E-10	1.59E-13	
	psi	Pa	atm		psi	Pa	atm
Upstream P _p	2060	14203700	140.17476	Upstream P _p	2120	14617400	144.25752
Downstream P _p	1940	13376300	132.00924	Downstream P _p	1880	12962600	127.92648
(p ₁ ² -p ₂ ²)/Length	8.88E+12			(p ₁ ² -p ₂ ²)/Length	1.78E+13		
Permeability (mD)	1.39E-19			Permeability (mD)	5.60E-20		
Permeability (nD)	141			Permeability (nD)	57		
Effective Stress (psi)	1000			Effective Stress (psi)	1500		
ΔP_p (Upstream-Downstream)	120			ΔP_p (Upstream-Downstream)	240		

$\sigma_{\text{eff}}=2000$ psi				$\sigma_{\text{eff}}=2500$ psi			
Parameter	Values			Parameter	Values		
Area (m ²)	1.14E-03			Area (m ²)	1.14E-03		
Length (m)	0.0257			Length (m)	0.0257		
Viscosity μ_f (mPas)	0.0184			Viscosity μ_f (mPas)	0.0184		
Downstream Flow Rate (cc/day)	17.725			Downstream Flow Rate (cc/day)	10.372		
Downstream Flow Rate (m ³ /s)	2.05E-10	1.59E-13		Downstream Flow Rate (m ³ /s)	1.20E-10	1.59E-13	
	psi	Pa	atm		psi	Pa	atm
Upstream P _p	2120	14617400	144.25752	Upstream P _p	2120	14617400	144.25752
Downstream P _p	1880	12962600	127.92648	Downstream P _p	1880	12962600	127.92648
(p ₁ ² -p ₂ ²)/Length	1.78E+13			(p ₁ ² -p ₂ ²)/Length	1.78E+13		
Permeability (mD)	4.83E-20			Permeability (mD)	2.83E-20		
Permeability (nD)	49			Permeability (nD)	29		
Effective Stress (psi)	2000			Effective Stress (psi)	2500		
ΔP_p (Upstream-Downstream)	240			ΔP_p (Upstream-Downstream)	240		

Figure 3.6: Results of the Upper Eagle Ford steady-state nitrogen permeability measurements at increasing effective stresses.

$\sigma_{\text{eff}}=3000 \text{ psi}$				$\sigma_{\text{eff}}=3500 \text{ psi}$			
Parameter	Values			Parameter	Values		
Area (m^2)	1.14E-03			Area (m^2)	1.14E-03		
Length (m)	0.0257			Length (m)	0.0257		
Viscosity μ_f (mPas)	0.0184			Viscosity μ_f (mPas)	0.0184		
Downstream Flow Rate (cc/day)	8.2793			Downstream Flow Rate (cc/day)	4.9467		
Downstream Flow Rate (m^3/s)	9.58E-11	1.59E-13		Downstream Flow Rate (m^3/s)	5.73E-11	1.59E-13	
	psi	Pa	atm		psi	Pa	atm
Upstream P_p	2120	14617400	144.25752	Upstream P_p	2120	14617400	144.25752
Downstream P_p	1880	12962600	127.92648	Downstream P_p	1880	12962600	127.92648
$(p_1^2 - p_2^2)/\text{Length}$	1.78E+13			$(p_1^2 - p_2^2)/\text{Length}$	1.78E+13		
Permeability (m^2)	2.26E-20			Permeability (m^2)	1.35E-20		
Permeability (nD)	23			Permeability (nD)	14		
Effective Stress (psi)	3000			Effective Stress (psi)	3500		
ΔP_p (Upstream-Downstream)	240			ΔP_p (Upstream-Downstream)	240		

$\sigma_{\text{eff}}=4000 \text{ psi}$				$\sigma_{\text{eff}}=5000 \text{ psi}$			
Parameter	Values			Parameter	Values		
Area (m^2)	1.14E-03			Area (m^2)	1.14E-03		
Length (m)	0.0257			Length (m)	0.0257		
Viscosity μ_f (mPas)	0.0184			Viscosity μ_f (mPas)	0.0184		
Downstream Flow Rate (cc/day)	5.7599			Downstream Flow Rate (cc/day)	3.7665		
Downstream Flow Rate (m^3/s)	6.67E-11	1.59E-13		Downstream Flow Rate (m^3/s)	4.36E-11	1.59E-13	
	psi	Pa	atm		psi	Pa	atm
Upstream P_p	2160	14893200	146.97936	Upstream P_p	2200	15169000	149.7012
Downstream P_p	1840	12686800	125.20464	Downstream P_p	1800	12411000	122.4828
$(p_1^2 - p_2^2)/\text{Length}$	2.37E+13			$(p_1^2 - p_2^2)/\text{Length}$	2.96E+13		
Permeability (m^2)	1.15E-20			Permeability (m^2)	5.90E-21		
Permeability (nD)	12			Permeability (nD)	6.0		
Effective Stress (psi)	4000			Effective Stress (psi)	5000		
ΔP_p (Upstream-Downstream)	320			ΔP_p (Upstream-Downstream)	400		

$\sigma_{\text{eff}}=6000 \text{ psi}$				$\sigma_{\text{eff}}=6000 \text{ psi}$			
Parameter	Values			Parameter	Values		
Area (m^2)	1.14E-03			Area (m^2)	1.14E-03		
Length (m)	0.0257	1.811024		Length (m)	0.0257	1.811024	
Viscosity μ_f (mPas)	0.0184			Viscosity μ_f (mPas)	0.0184		
Downstream Flow Rate (cc/day)	1.1418			Downstream Flow Rate (cc/day)	2.371		
Downstream Flow Rate (m^3/s)	1.32E-11	1.59E-13		Downstream Flow Rate (m^3/s)	2.74E-11	1.59E-13	
	psi	Pa	atm		psi	Pa	atm
Upstream P_p	1620	11169900	110.23452	Upstream P_p	1740	11997300	118.40004
Downstream P_p	1380	9515100	93.90348	Downstream P_p	1260	8687700	85.73796
$(p_1^2 - p_2^2)/\text{Length}$	1.33E+13			$(p_1^2 - p_2^2)/\text{Length}$	2.66E+13		
Permeability (m^2)	3.05E-21			Permeability (m^2)	2.89E-21		
Permeability (nD)	3.1			Permeability (nD)	2.9		
Effective Stress (psi)	6000			Effective Stress (psi)	6000		
ΔP_p (Upstream-Downstream)	240			ΔP_p (Upstream-Downstream)	480		

Figure 3.7: Continuation of the results for the Upper Eagle Ford steady-state nitrogen permeability measurements at increasing effective stresses.

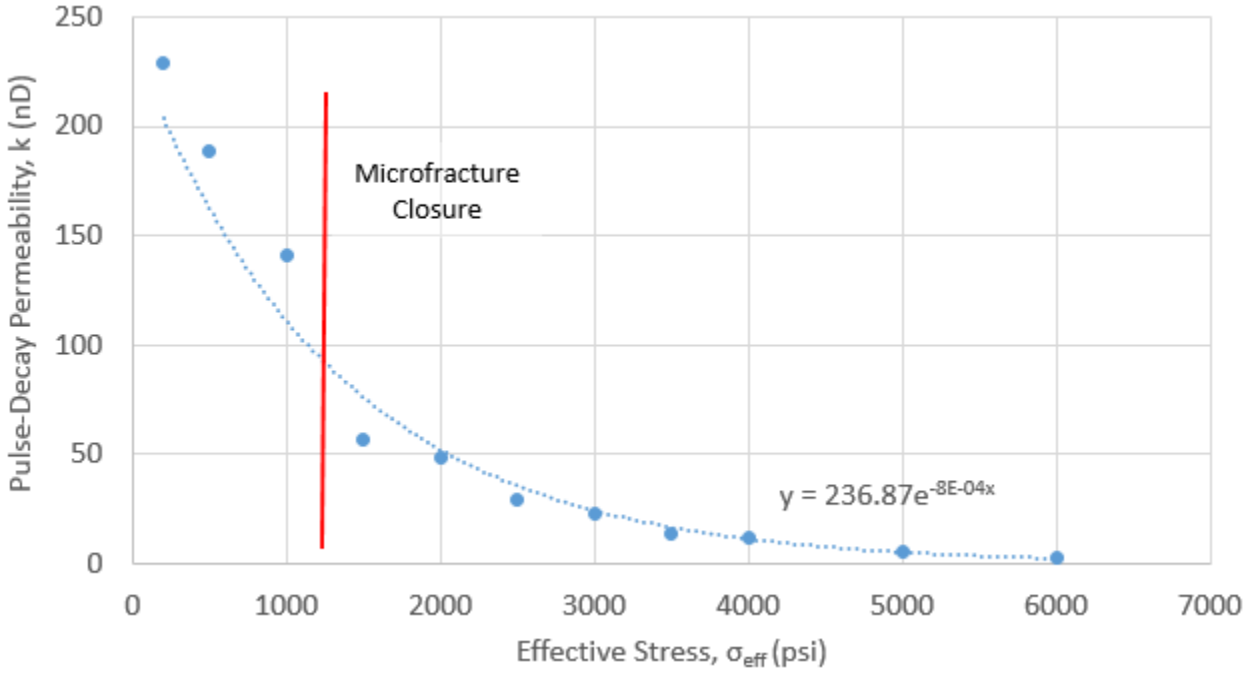


Figure 3.8: Dependence of steady-state determined permeability on effective stress of the sample.

3.2.3 Comparison of Pulse-Decay and Steady-State Permeability Measurements

Comparing the two methods of measuring permeability, pulse-decay and steady-state with increasing effective stress shows minimal difference between the results of permeability of the two methods. As illustrated in Figure 3.9, the exponential trendline for both methods are a close match, with the representative equations having little variance. Showing that the two methods produce equivalent results, it can be concluded for time saving capabilities that carefully performed pulse-decay measurements would be optimal in comparison to the steady-state method.

3.2.4 High Stress Directional Dependence of Gas Permeability

Kamath et al. (1992) studied super-low permeable rocks and the directional dependence of gas permeability in laboratory testing. During the permeability measurements of this study, the upstream and downstream reservoirs were switched as to see if the direction of

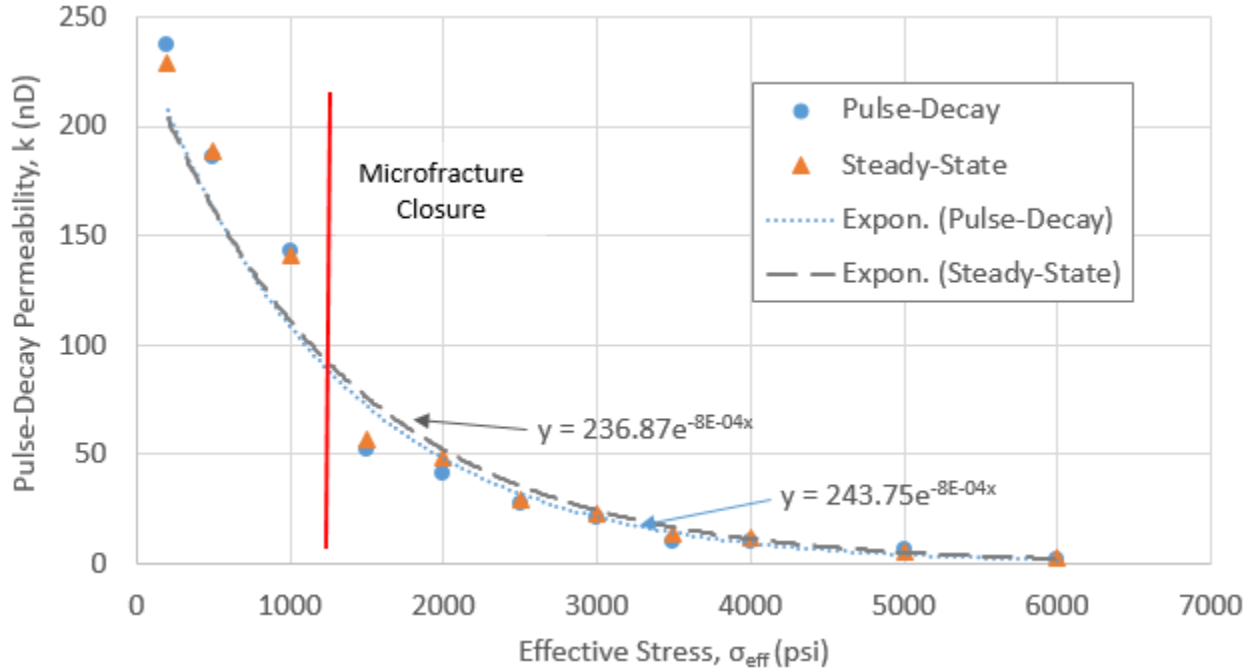


Figure 3.9: Comparison of the two methods of measuring permeability, pulse-decay and steady-state with increasing effective stress. There is minimal difference observed between the two methods of measurement, though it is concluded for an efficiency standpoint it is more effective to perform pulse-decay permeability measurements.

gas flow affects the resultant permeability. At an effective stress of 1,500 psi the steady-state method of permeability measurements were performed from the bottom to top of the sample, and the reverse from the top to bottom of the sample. Results from the Eagle Ford shale permeability measurements shows the differing permeability for the alternate flow directions is listed in Table 3.9. This results signifies a difference in the pore throat geometry and connectivity due to the direction of flow. Seeing that the electrical properties of rocks are dependent on the pore throat geometry and connectivity (Herrick 1988; Herrick et al. 2001; Kennedy and Herrick 2012; Suman and Knight 1997), one can conclude that also the electrical measurements would vary for the direction of flow.

3.3 Shale Resistivity Stress Dependence

The Eagle Ford shale sample GZ#6 was prepared for the pore pressure penetration test as described in Appendix A. Saturation of the core was initiated with an equivalent in situ brine

Table 3.9: Comparison of the directional dependent gas permeability results at an effective stress of 1,500 psi for the steady-state method of measurements. It is observed that varying results are obtained dependent on the upstream and downstream flow of gas.

	Bottom to Top Permeability (nD)	Top to Bottom Permeability (nD)
$\sigma_{eff} = 1500psi$	57.0	72.3

fluid, being 60,000ppm KCl. A process of bringing the core back to reservoir conditions takes a long time of slowly increasing axial (overburden) stress, confining stress, pore pressure, and saturation. Resistivity measurements were performed throughout these initial phases to monitor the electrical properties, and to determine if any correlations between these parameters exists. Of main concern in this section is examining the change in resistivity due to the stress state changes. First, the resistivity measurements during the consolidation period are observed for their dependence on the effective stress. A correlation can be made to look at the change in resistivity due to an effective stress state change, and then used to determine the resistivity change during the osmosis process due to the decrease in effective stress from pore pressure build up due to osmosis.

Resistivity results from the osmotic pressure test on the Eagle Ford core sample are represented in Figure 3.10. Initial resistivity values were obtained before placing the core sample into the triaxial testing cell. It is observed that the resistivity values measured between electrodes labeled zero and one represented in the core schematic in Figure 1.1, showed peaks and troughs which were inconsistent with the other electrode measurements. The measurements for this electrode before the initiation of the osmotic pressure tests are deemed invalid. The possible cause for the sporadic behavior may be due to electrical interference from an uninsulated triaxial cell piston, or electrical short in the wires. The data collected between electrodes 1, 2, and 3 is representative of what is expected after performing the Berea Sandstone trials performed under the similar stress state conditions.

Saturation of the core was initiated with a 60,000 ppm KCl solution and a significant decline in the resistivity values have observed at all electrodes. The initial steep decline

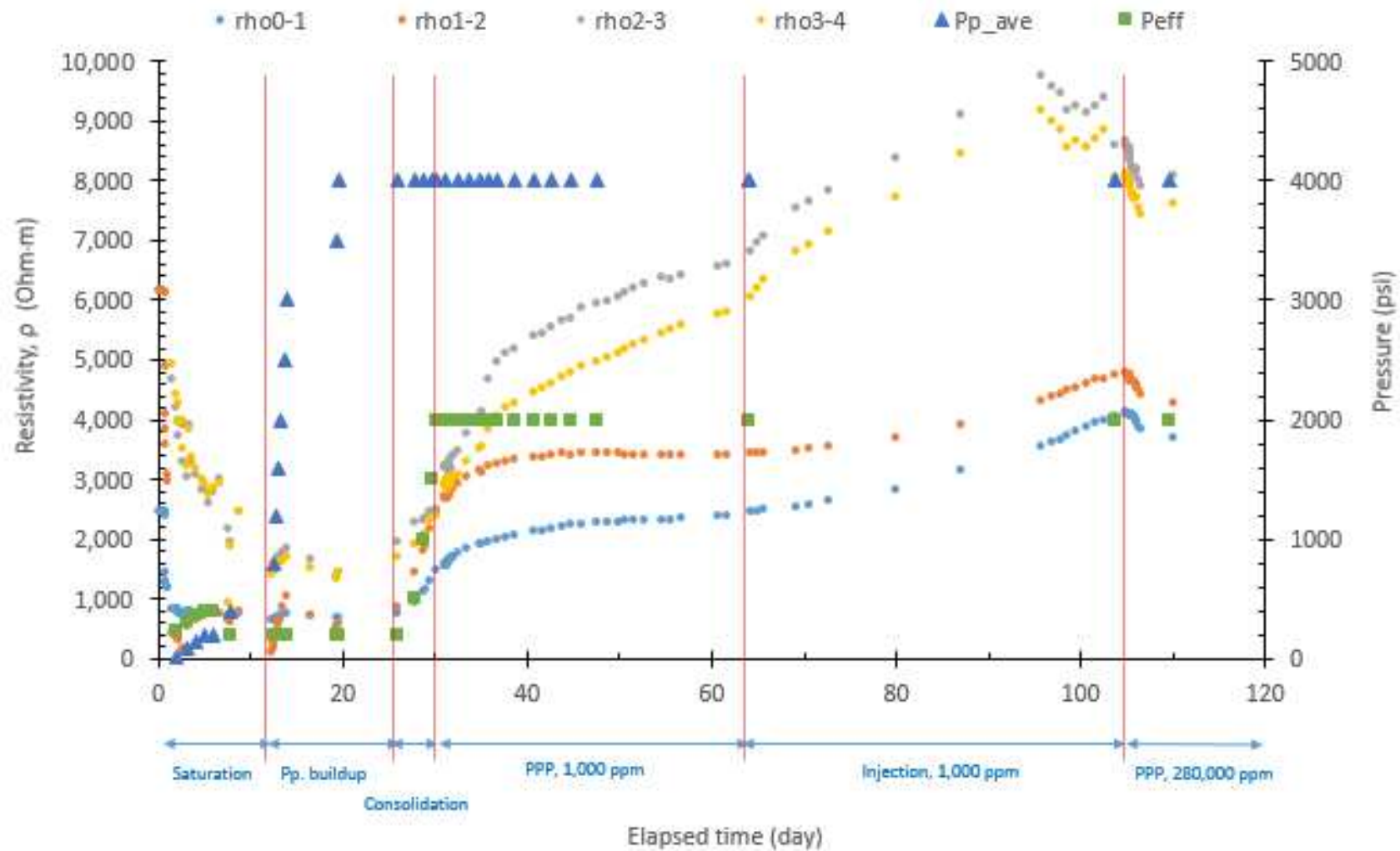


Figure 3.10: Results for resistivity measurements during pore pressure penetration on an Eagle Ford shale sample. Observed is the initial drop in resistivity due to the saturation of a 60,000 ppm KCl solution, then an increase in resistivity due to consolidation and injection of a 1,000 ppm KCl solution for the osmosis tests. Also, the corresponding P-wave velocity data is shown to increase with saturation as well as consolidation.

lasted about 10 days before a slower, gradual decline in resistivity occurred to about 25 days when the measurements leveled out and became relatively constant. Figure 3.11 shows a zoomed-in look at the initial saturation, pore pressure build up, and consolidation period and how the resistivity values are affected. The resistivity decrease from days 11 through to 25 could be due to further saturation of the core, but also from the increase in pore pressure. In future testing it is recommended to ensure complete saturation before pore pressure build up as to determine any effects of the pore pressure build up on resistivity, which would represent a pore geometry change within the rock due to increase in pressure or potentially due to rock-fluid interactions. Once the resistivity values reached the constant lower value around day 25, Skempton's b-coefficient was calculated to be 0.75. This high correlation between pore pressure change and the stress state change in the rock provides more evidence that saturation of the shale core sample has occurred. With saturation complete, consolidation of the core started with increases in the effective stress to bring the rock back to in situ stress conditions.

It can be observed from the resistivity and compressional wave velocity data shown in Figure 3.10 and Figure 3.11 that the resistivity measurements are stress dependent. A clear response from the measured resistivity value is observed around the 26 day mark, when a sharp increase is observed. This corresponds to an increase in the effective stress state of the rock through increased axial, confining, and pore pressure to in situ conditions. The effective stress is plotted on Figure 3.11 by the green squares. The clear increase in effective stress and increase in resistivity is observed. The increased effective stress closes micro-fractures, pore throats, and generally restricts flow. Looking back to the dependence of permeability on effective stress, a sharp decrease in permeability is observed between effective stresses of 1,000 psi to 1,500 psi. There is no such sharp increase observed for resistivity due to the increase in effective stress, rather a constant more linear increase.

Stress dependence of the resistivity is a valuable measurement and observation used to help hypothesize the changes in pore space size. As shown in Figure 3.12, when the effective

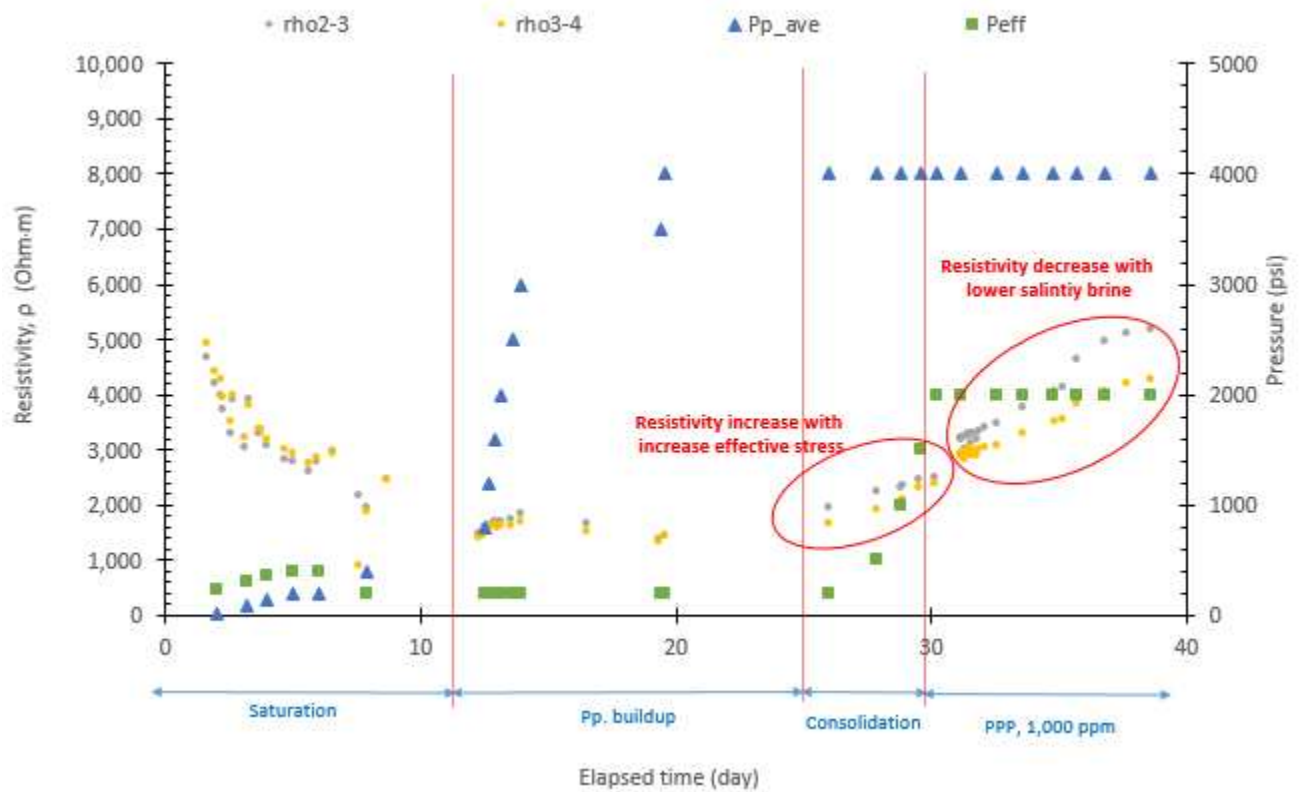


Figure 3.11: An observed increase in resistivity due to the increased effective stress state on the Eagle Ford shale sample, and a second increase in resistivity due to the introduction of a lower salinity fluid at the initiation of the osmotic pressure tests.

stress increases, there is a clear linear trend of resistivity increasing with the effective stress. This represents pore space decrease, yet it is more vital due to the compressional velocity being relatively constant value at effective stress values equal to or greater than 1,000 psi, as shown in Figure 3.13. Because P-wave velocity data remains constant after 1,000 psi effective stress, resistivity provides valuable insight on how the rock matrix is changing due to the increased stress state and the rock-fluid interactions taking place where the P-wave velocity is not capable of showing such subtle differences or changes. As the resistivity increases, it represents closure of the micro pore space with the dispersed pore fluids. The changing resistivity while P-wave velocity measurements stay constant shows that the rock geometry is still changing, and that resistivity is an accurate method to capture the changing structure of the rock. This resistivity variation is believed to reflect the inhomogeneity of microstructure

of the shale sample tested. The mechanism of increasing resistivity due to stress increase can be attributed to dehydration of shale sample due to increasing effective stress. The data agrees with the work by Kennedy and Herrick (2012) with the geometric factor, E_o .

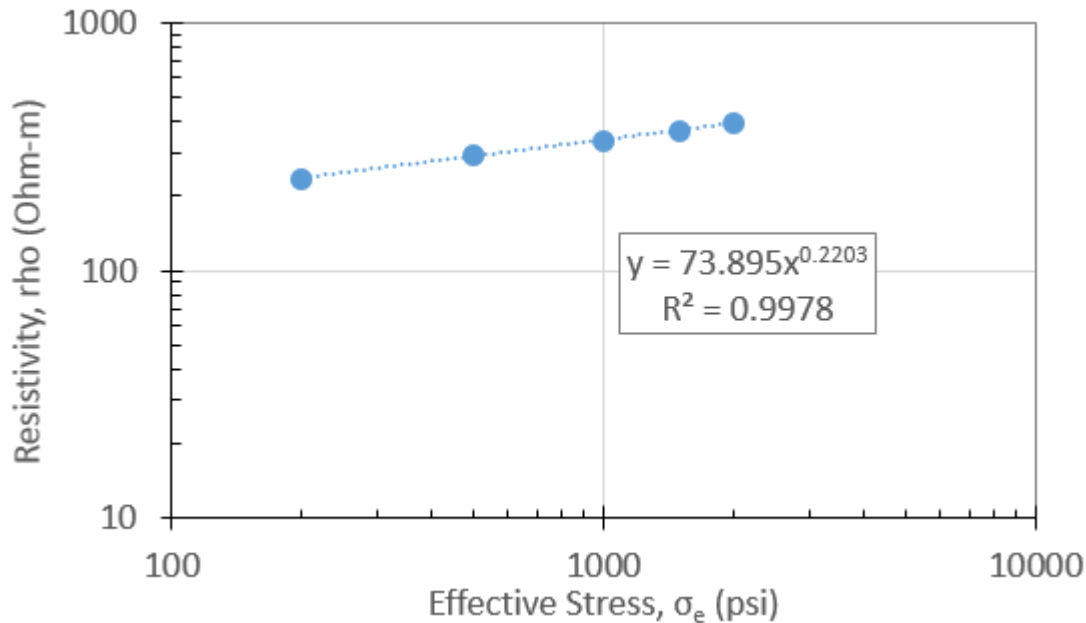


Figure 3.12: Measured resistivity as a function of effective stress in an Eagle Ford preserved shale core sample. A linear trend showing the increase of resistivity with increasing stress is displayed.

The relation between effective stress and resistivity is also important for better understanding the osmotic pressures. From this experimental work, it is shown that an increase in pore pressure is observed due to the diffusion of salt ions. The increase in pore pressure represents a decrease in the effective stress, which would then alter the measured resistivity. It is important to correctly account for the change in effective stress due to osmotic pressures when interpreting the resistivity measurements during the osmotic pressure stage of the work. Section 3.4 addresses this topic.

As thoroughly discussed in the previous section is the relation between effective stress and permeability. Here, we show the relation between permeability and resistivity. It is seen that as the permeability of the rock decreases the resistivity increases. This brings further evidence to the point that resistivity is highly dependent on the pore geometric changes in

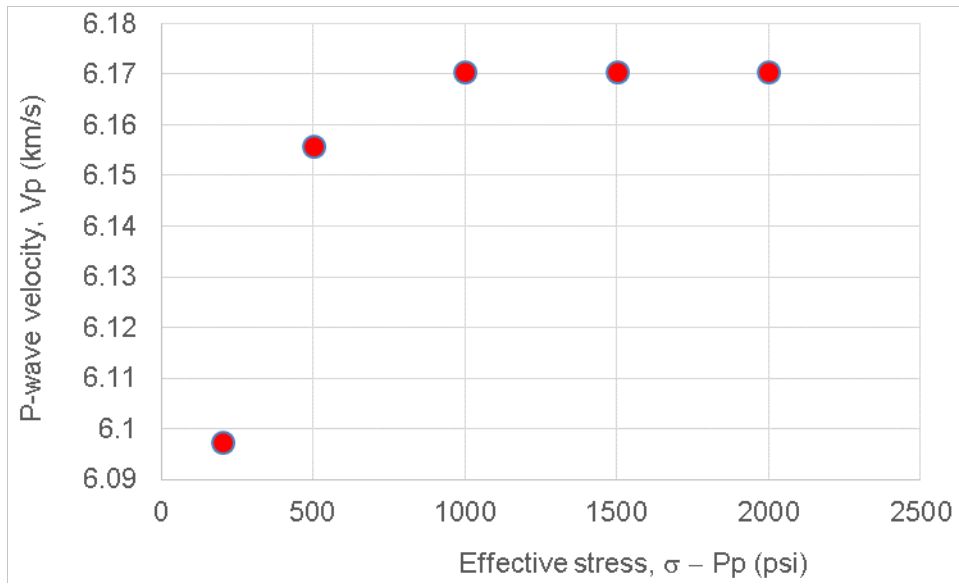


Figure 3.13: Compressional velocity as a function of effective stress in Eagle Ford preserved shale core sample measured in this study. The increased velocity reaches a plateau at 1,000 psi effective stress where in comparison to the resistivity data, the resistivity maintains a positive upward slope which signifies additional changes in the rock structure passed the effectiveness of the P-wave velocity measurements.

the rock, specifically at the pore throats. The decrease in permeability decreasing from 151 to 9.3 nD with increasing effective stress from 200 psi to 2,000 psi as seen in Figure 3.14, and is representative of the closure of natural fractures, nano pores and tightening of pore throats. This is directly related to resistivity as it has been shown in previous work that resistivity is dependent on the pore geometry (Herrick 1988; Herrick et al. 2001; Kennedy and Herrick 2012; Suman and Knight 1997). Also, one can observe in Table 3.9, if the permeability is direction dependent, it would also lead to resistivity being directionally dependent. The direct relation between resistivity and permeability is shown in Figure 3.15, presenting a decrease in permeability results in an increase in resistivity and is represented by a linear trend.

Applications of the data collected showing the dependency of effective stress on resistivity will strongly aid in explaining rock matrix changes effecting the resistivity values in addition to explaining rock-fluid interactions, such as in osmotic pressure tests. Other applications

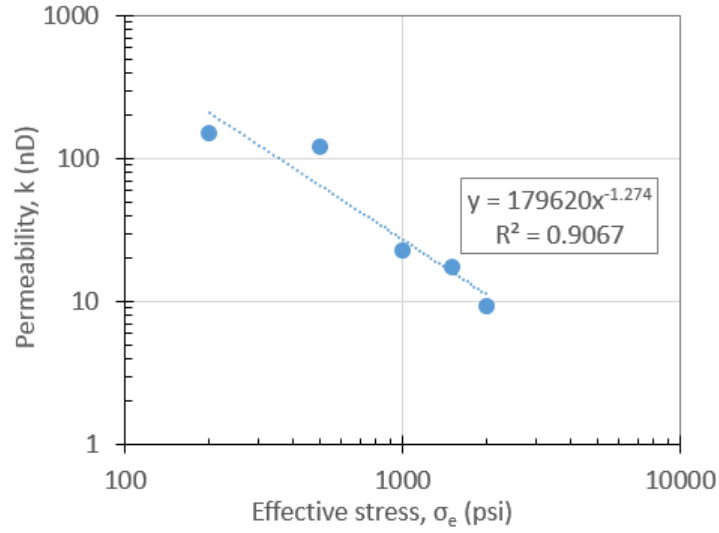


Figure 3.14: Stress dependency of permeability measurements of Eagle Ford shale sample. As the effective stress increases, this represents closure of the pore throats decreasing permeability of the rock .

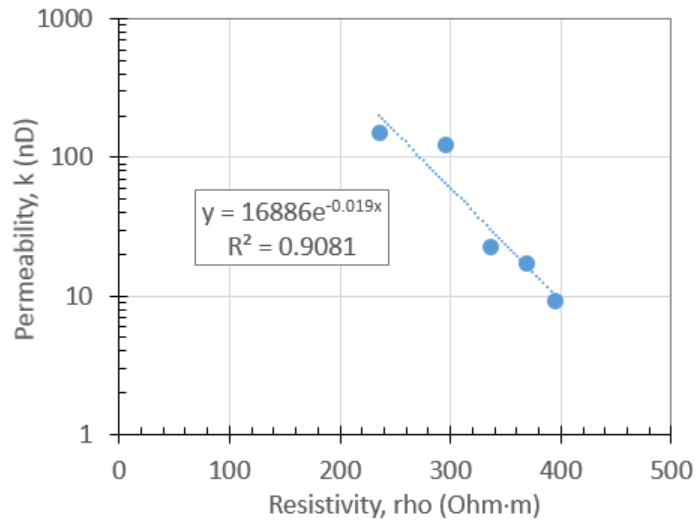


Figure 3.15: Relation between permeability and resistivity. As the permeability of the rock decreases due to closure of natural fractures, nano-pores and constriction of pore throats the resistivity also decreases from the reduction of the pore geometry.

of the stress dependent resistivity may be used in depleted reservoirs where compaction has occurred and increases in resistivity may be present. The compaction would lead to increased resistivity, which would need to be coupled with other logging tool measurements to show that the increase in resistivity is not due to the presence of hydrocarbons, but due to the increase of effective stress. Also, during drilling operations infiltration of drilling fluids into formations is noted as a decrease in shallow resistivity. Another explanation for the decrease in resistivity could be due to matrix changes, opening pore throats and increasing fracture networks from drilling operations and rock fluid interactions. This is especially true in shale formations where permeability is so low, infiltration should not so regularly occur; however chemical osmosis can occur in the shale and alter the resistivity measurements.

3.4 Effects of Osmotic Pressures on the Interpretation of Measured Resistivity

The overall goal of the larger experimental research project is to gain a better understanding of osmotic pressures in shale plays. Experimental testing to determine the effects of osmotic pressure are performed through pore pressure penetration tests. A triaxial testing cell exposes the 1.5 inch diameter by 1 inch in length shale core samples to in-situ, isotropic stress conditions; while a low-salinity brine is circulated at the base of the sample at reservoir pore pressures. As the low salinity brine circulates at the base of the core, it is imbibed vertically and a pressure difference is observed between the base and top of the core due to the effects of ion diffusion and the resultant osmotic pressure. Osmosis occurs when water molecules from the low-salinity fluid migrate to the high-salinity side to equilibrate the solution (Fakcharoenphol et al. 2014).

The Eagle Ford sample from GZ#6 is slowly saturated from the base of the sample up; first aided by applying vacuum on top side of the core and second by applying successive increases in pore pressure from the base. Saturation of the core is determined complete at almost 24 days. After achieving maximum water saturation, the core is subjected to a consolidation process in which the overburden and confining stresses were increased, but effective stress was maintained constant. Consolidation of the core brings the stress state

of the rock back to in situ conditions and causes the induced fractures to close. During this process, water permeability is measured step by step to help understand stress-related permeability changes coupled with resistivity. After consolidation is complete, the osmotic pore pressure penetration test starts, lasting for about 9 days. 1,000 ppm NaCl brine is circulated at the base of the sample and pressure buildup from zero is monitored at the top side of the sample. During the osmosis section of the test, pore pressure at the monitoring transducer increased until it equilibrated with the bottom circulating pressure then kept increasing gradually until equilibrating at roughly day 40. Graphical results from the osmosis test show the increase in pore pressure above the applied pore pressure at 4,000 psi as represented by the red line in Figure 3.16. It is observed that the pore pressure at the top reached a maximum of about 500psi pressure difference, which would decrease the effective stress by 500psi as Biot's coefficient is assumed to be equal to one.

The increase in pore pressure, resulting in a decrease in effective stress will alter the pore geometry of the rock, thus affecting the resistivity measurements. During consolidation of the core resistivity measurements were recorded for increasing effective stress as seen in Figure 3.12. Using the known trend of how the resistivity changes due to effective stress the difference in resistivity can be calculated due to the decrease in effective stress from increased pore pressures. Figure 3.17 shows the results of correcting the resistivity for the increased pore pressures due to osmosis, thus isolating out the effects of effective stress on resistivity. As can be observed the measured resistivity (orange dashed line) is higher than the corrected resistivity (gray solid line), because the effective stress is not accounted for in the interpretation of the resistivity data. The measured resistivity is still increasing due to the imbibition of the lower 1,000 ppm brine in comparison to the 60,000 ppm in situ brine, however, the decrease in effect of effective stress on resistivity can not be seen until the data has been corrected for. The increase in pore pressures due to osmosis decreases the effective stress, which would open up pore space and decrease resistivity. Also seen between the difference of the modeled resistivity and the measured is the sharp difference at the 34

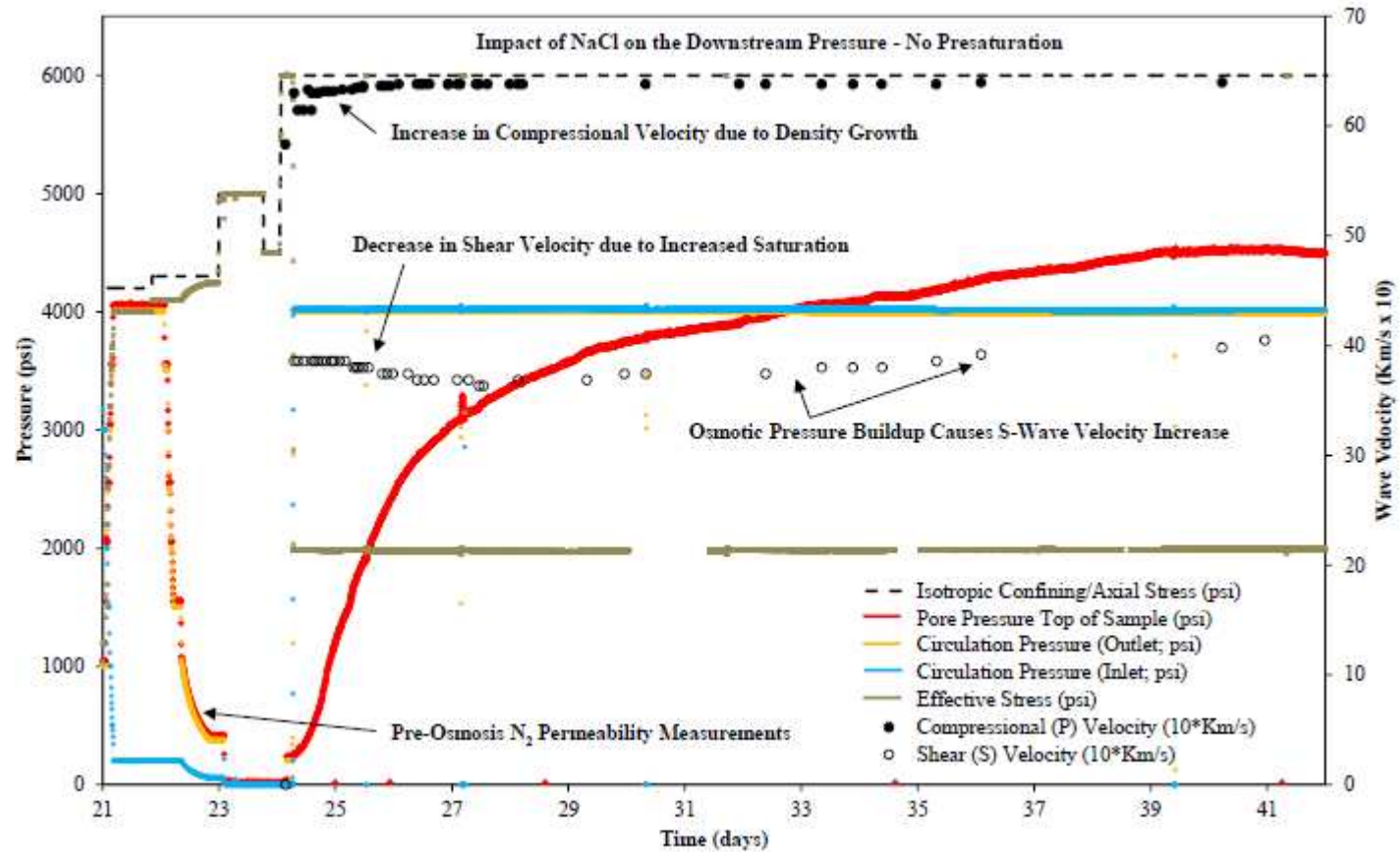


Figure 3.16: Osmosis experiment with low salinity (1,000ppm) NaCL brine solution. At day 33 the top side pore pressure passed the base pore pressure and gradually increased and reached a peak of an additional 500psi of pore pressure at the top of the sample.

day mark, which is when pore pressures increase above 4,000 psi. This difference could be due to the reaction time of the shale changing pore geometries. Just as shale takes time to relax when cores are taken from subsurface to surface, the pore geometry here did not react instantly to the change in effective stress, rather it made a slow change.

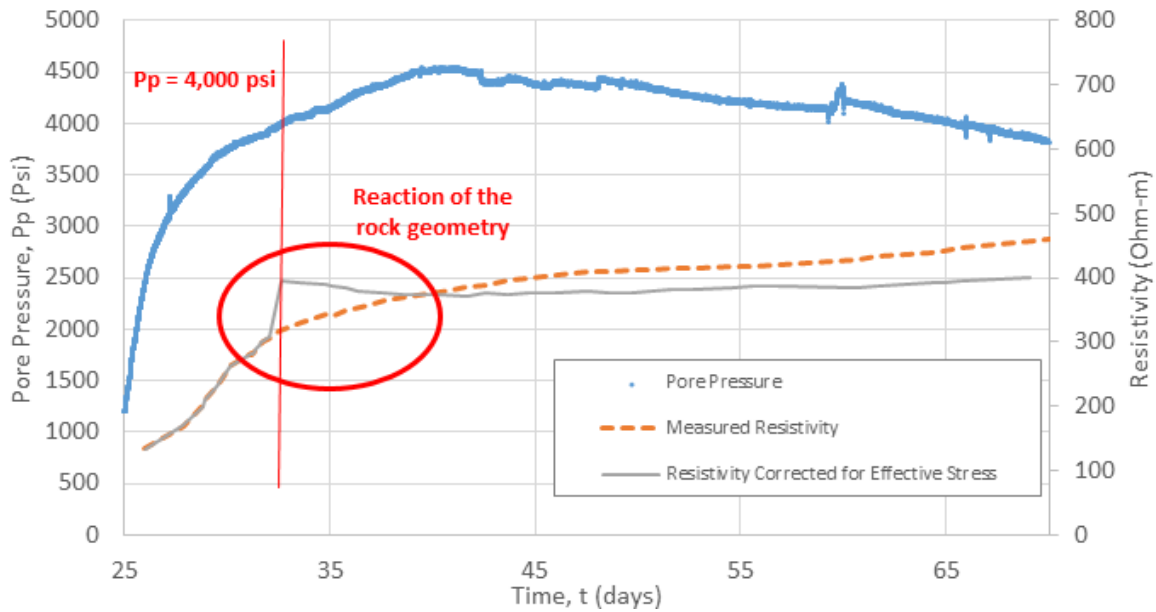


Figure 3.17: Correcting measured resistivity for effective stress due to the increase in pore pressure from osmosis shows a decrease in the actual resistivity of the rock if osmosis had not occurred. Also observed is a difference between the model and the measured resistivity at point which pore pressure passes the original 4,000 psi. This shows that there is a reaction time for the rock, that the deformation of the pore geometry is not instantaneous, rather slowly occurring.

Once correcting for the effective stress, it is evident that the resistivity of the formation is less than its true resistivity. This can greatly affect log interpretation, because the brine used during drilling operations will create the osmotic pressures as measured in this experimental work. For shallow reading resistivity logging tools where the effects of the osmotic pressure will be relevant, the greater pore pressures will cause lower readings of the resistivity. Calculations of water and hydrocarbon saturations will not be accurate due to the decreased measured resistivity, consequentially affecting hydrocarbon volumes as well as a result of the wrongly interpreted resistivity logs.

CHAPTER 4

TRACKING BRINE IMBIBITION WITH RESISTIVITY MEASUREMENTS

The relation of pore geometry and stress state exhibited on the rock is a simple one; increased effective stress squeezes the rock and decreases the pore sizes. It has also been shown that constrictions in the connectivity and pore structure of a porous rock matrix influences the measured resistivity of the saturated rock. It has been observed in experimental work that as the stress state on the rock increases, representative of a decrease in connectivity, produces an increase in resistivity. (Brace et al. 1965; Dobrynin 1962; Winsauer et al. 1952). Archie's Equation accounts for the pore geometry through the use of empirically derived exponents (a), (m), and (n) representing tortuosity, cementation, and wettability. It has been proven by many researchers that these Archie exponents are not accurately accounted for or measured (Herrick 1988). Here a comparison of Archie's methods of determining electrical properties is compared with that of the electrical efficiency as detailed by Herrick et al. (2001). What has not be studied is the ability of resistivity measurements in tracking ion diffusion in rock samples. This sections proposes and shows the results to experimental efforts to track a low salt concentration fluid front as it is imbibed vertically through a core sample. These results are then compared to a model of the change of concentration over time.

4.1 Sandstone Resistivity

The first test performed with the triaxial cell was on a one inch long by one-and-a-half inch diameter Berea Sandstone plug. The sample was setup with electrodes and assembled in the triaxial cell in accordance to the procedures outline in Appendix A. Pressures were increased in step changes until the final test conditions were reached, i.e.: $P_a = 4500\text{psi}$, $P_c = 4500\text{psi}$, and $P_p = 4000\text{psi}$. An 18 wt.% NaCl solution was circulated at the base of the core while the resistivity measurements were recorded between electrodes 0, 1, 2, 3, and

4. Figure 4.1 displays the results and trend observed that formation factor decreases with increasing saturation, as well as a P-wave velocity increases with increasing saturation. It is observed that the lower limit of the formation factor curve reaches a resistivity of about 8 ohm-m, which is deemed to represent full saturation of the sandstone sample. To check saturation, Skempton's b-Value is also calculated. Results of which showed a consistent b-value at varied stress state of 0.83-0.85, from which it can be assumed that full saturation has occurred. Archie (1942) first used the formation factor to relate the effect of brine resistivity on the rock. From which if formation factor is plotted against varying brine resistivity the rock type, for a clean sandstone or shaly sand, then it can be determined from the variation in the slope of the line. A constant value of formation factor represents a clean sandstone, while if there is a decreasing trend in the formation factor with increased brine resistivities this would represent a shaly sand. The effect on formation factor is dependent on the type, amount and distribution of the clay within the sandstone as discussed by Tiab and Donaldson, (2012). Due to the injection of only an 18 wt.% solution this graphical correlation was not made to determine how clean the sandstone sample is.

Brine resistivity (R_w) is calculated chemically to be 0.35 Ohm-m, which remained constant throughout the laboratory procedure and an experimental value of formation factor of 13.03 has been used from the literature (Mahmood et al. 1991) from a similar porosity Berea sandstones. From this work, the Archie factors to solve for water saturation being a, m, and n are also determined to have values of 2, 1.75, and 1.667, respectively. A comparison of the two methods of calculating the water saturation, electrical efficiency and Archie's Method have been examined. The electrical efficiency for the Berea sandstone sample is calculated when 100% saturation is determined from Skempton's b-value and at the lowest values of measured resistivity, as displayed in Equation 4.1. An electrical efficiency value of 0.3515 is determined from the experimental data which matches well with the expected estimated value from the relation of formation factor (F_r), porosity (ϕ), and electrical efficiency (E_o) as displayed in Equation 4.2 (Herrick and Kennedy, 1993), which produces an electrical

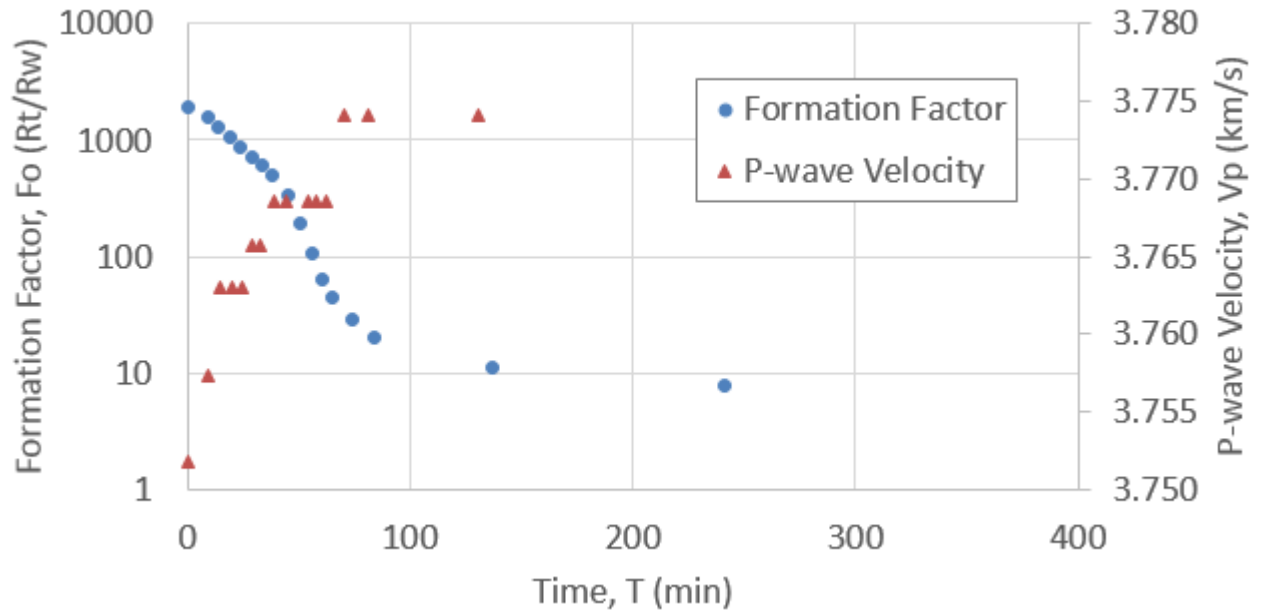


Figure 4.1: Formation Factor (F_r) throughout the saturation period. It is observed that (F_r) decreases with the time of which the sample is exposed to 18 wt.% NaCl solution. Also displayed is the P-wave velocity data recorded throughout the saturation which is seen to increase with decreasing formation factor.

efficiency of 0.3799 from the given formation factor of 13.03 and porosity of 0.202.

$$E = \frac{C_t}{C_w S_w \phi} \quad (4.1)$$

$$\frac{1}{F_r} = E_o \phi \quad (4.2)$$

From the measured resistivity and determined electrical properties, the initial water saturation of the sandstone core was calculated to compare both the Archie Method and the Electrical Efficiency. Figure 4.2 presents the difference between the two methods of determining the water saturation. As it is evident, Archie's Method has a higher water saturation when compared to the electrical efficiency. The difference does get smaller when getting fully brine saturated state is approached, however, at lower saturations, there is a large difference between the calculated values from the two methodologies. The difference is largely due to the representation of the geometric effects on the resistivity, and how they are accounted for in each equation. As it has been stated earlier in Chapter Two, (a) and

(m) are derived from graphical analysis, manipulating the base equation to try and fit the experimental data. Patnode and Wyllie (1950) showed that the calculated formation factor is less than the true formation factor when conductive solids are present within cores. Further work was performed by Winsauer et al. (1952) which studied how tortuosity and porosity determines the resistivity factor and found that the Archie model did not fit their data. Also wettability (n) does not account for the microanisotropic changes from saturation of the core. Rock-fluid interaction alters the physical pore geometry, thus, affecting the currents path and ultimately varying resistivity (Herrick et al. 2001). Determining water saturation utilizing the Electrical Efficiency theory equates water saturation from the electrical properties of the rock and groups the effects of pore geometry into the term (E) as presented in Equation 1.16(Herrick et al. 2001). The electrical efficiency is separate from that of porosity and water saturation, however, is still empirically related to the two factors.

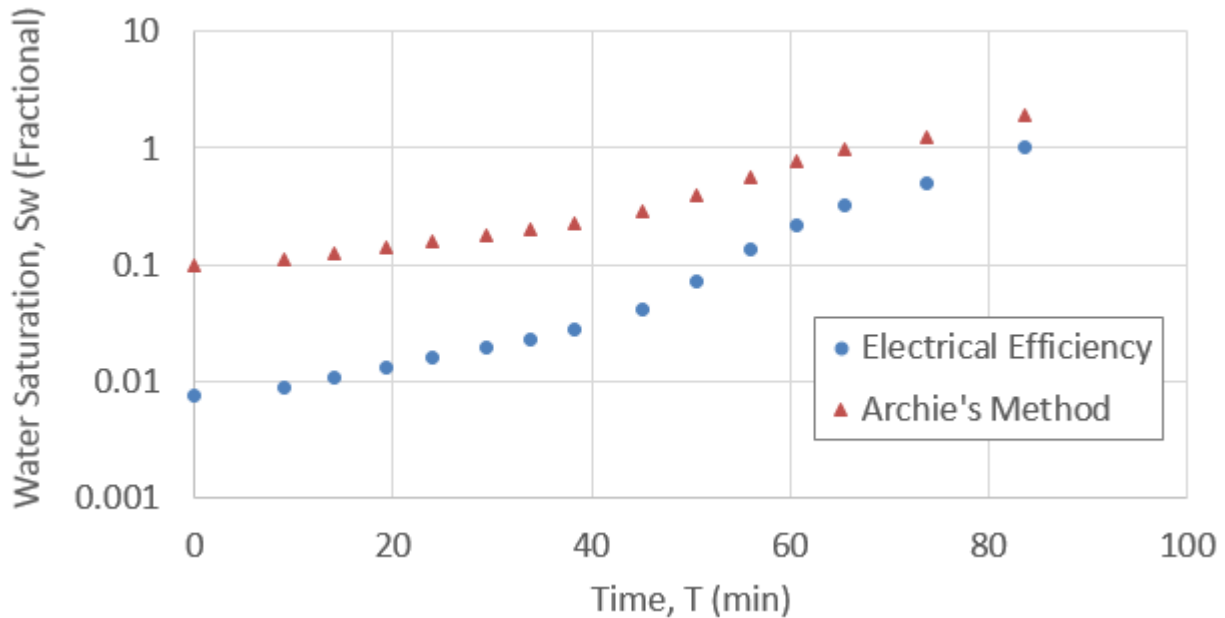


Figure 4.2: Comparison of water saturation calculation using Archie's Method and the method of Electrical Efficiency as presented by Herrick and Kennedy, (1993). As it is observed there is a strong difference in the calculated water saturation between the two methods.

4.2 Tracking Fluid Migration Using Resistivity

Key to the osmotic pressure experimental work is understanding the location of the fluid front as it imbibes through the core. Coupling the measured resistivity with the work of a PhD. student at CSM, Binh Bui, a basic model using the continuity equation is developed to show the relation of the brine fluid front moving through the core with the change in resistivity due to the concentration of the brine solution. From the data gathered a relationship between the brine fluid front via the concentration, and resistivity is derived. First, a plot of the measured resistivity of known concentration NaCl solutions is plotted as seen in Figure 4.3. This plot and the fitted trendline equation provides a relationship of the brine resistivity to its NaCl concentration in parts per million (ppm). Having this relationship shows that if the brine resistivity (R_w) is known, the concentration (C_{NaCl}) can be solved for, as shown in Equation 4.3 which has taken the equation for the trendline in Figure 4.3 for the concentration of NaCl.

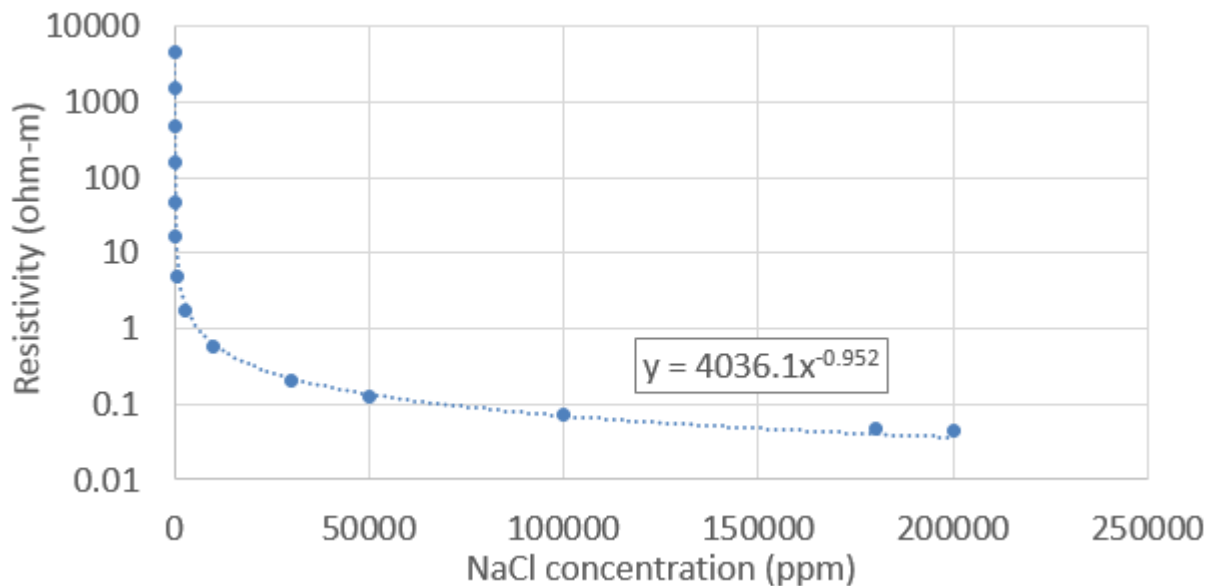


Figure 4.3: Resistivity of varying brine concentrations. A power function relates the two resistivity of the varying concentrations of NaCl which is then used to determine the brine concentration from the measured total resistivity during triaxial tests.

The calculated brine concentration from the brine resistivity must then be correlated to the measured total resistivity of the core during testing. Brine resistivity (R_w) can be solved for using Herrick and Kennedy's electrical efficiency equation assuming the core is fully saturated ($S_w = 1$) and that the electrical efficiency (E_o) does not change due to rock-fluid interaction as shown in Equation 4.4. For the sandstone sample tested, it is safe to assume that there will be minimal change to the pore geometry, representing no change in (E_o). The electrical efficiency is solved for once the core is fully saturated as described in section 4.1, which is also confirmed by both sonic measurements and Skempton's b-value. Substituting Equation 4.4 into 4.3, a relation for the measured total resistivity (R_t) to the brine concentration is determined as shown in the resultant Equation 4.5.

$$C_{NaCl} = \left(\frac{R_w}{4036.1} \right)^{\frac{-1}{0.952}} \quad (4.3)$$

$$R_w = E_o R_t S_w \phi \quad (4.4)$$

$$C_{NaCl} = \left(\frac{(E_o R_t S_w \phi)}{4036.1} \right)^{\frac{-1}{0.952}} \quad (4.5)$$

Having a direct relation between the measured total resistivity (R_t) and the concentration of NaCl (C_{NaCl}) as the brine is imbibed vertically enables a simple model to be created and matched to the experimental data. As the resistivity of the samples changes it can be represented as a change in the concentration of the brine solution, which show the migration of the salt through the core. Detailed extensively in the PhD. dissertation by Binh Bui (2016) is the mathematical model utilized to represent the osmosis process and how the brine solution is imbibed vertically through the core. The following transport equations are solved for pressure and concentration. Detailed analysis of the formulas is out of the scope for this work, though a general explanation is shown:

For water phase:

$$\nabla \cdot \left[\rho_w \frac{\mathbf{k}_{wm}}{\mu_w} \nabla (p_{wm} - \gamma_w D_m) - \rho_w \frac{\mathbf{k}_{wm}}{\mu_w} \omega \frac{RT_m}{V_w} \nabla c_{sm} \right] + \rho_w \hat{q}_{wm} = \frac{\partial}{\partial t} (\rho_w \phi_m) \quad (4.6)$$

and solute:

$$\nabla \cdot \left\{ c_{sm} \rho_s \frac{\mathbf{k}_{wm}}{\mu_w} \left(\frac{\rho_w}{\rho_s} \frac{c_{sm}}{1 - c_{sm}} - \omega \right) \left[\nabla (p_{wm} - \gamma_w D_m) - \frac{\omega R T_m}{V_w} \nabla c_{sm} \right] + \phi_m \rho_s D^{eff} \nabla c_{sm} \right\} + \rho_s \hat{q}_{sm} = \frac{\partial}{\partial t} (\rho_s \phi_m c_{sm}) \quad (4.7)$$

This following equations presents the finite difference solution of the mass transport equation for the core sample. From the matrix total pressure Equation 4.6, the algebraic equation to obtain the pressure along the core can be solved for as,

$$M_{xb} p_{wm_{i-1,j,k}}^{n+1} + M_{xm} p_{wm_{i,j,k}}^{n+1} + M_{xf} p_{wm_{i+1,j,k}}^{n+1} = M_{xR} \quad (4.8)$$

where:

$$M_{xb} = \frac{1}{\Delta x_{i,j,k}} \left(\frac{\mathbf{k}_{wm}}{\mu_w \Delta x} \right)_{i-\frac{1}{2},j,k}^n \quad (4.9)$$

$$M_{xf} = \frac{1}{\Delta x_{i,j,k}} \left(\frac{\mathbf{k}_{wm}}{\mu_w \Delta x} \right)_{i+\frac{1}{2},j,k}^n \quad (4.10)$$

$$M_{xm} = - \left\{ M_{xb} + M_{xf} + \frac{1}{\Delta t_m} [\phi_m c_{tm}]_{i,j,k}^n \right\} \quad (4.11)$$

$$M_{xR} = \frac{1}{\Delta x_{i,j,k}} \left\{ \left(\frac{\mathbf{k}_{wm}}{\mu_w \Delta x} \right)_{i+\frac{1}{2},j,k}^n [\gamma_{w_{i,j,k}} (D_{i+1,j,k} - D_{i,j,k})] - \left(\frac{\mathbf{k}_{wm}}{\mu_w \Delta x} \right)_{i-\frac{1}{2},j,k}^n [\gamma_{w_{i,j,k}} (D_{i,j,k} - D_{i-1,j,k})] \right\} +$$

$$\frac{\omega R T_m}{\Delta x_{i,j,k}} \left[\left(\frac{\mathbf{k}_{wm}}{\mu_w \Delta x} \right)_{i+\frac{1}{2},j,k}^n \left(c_{sm_{i+1,j,k}}^n - c_{sm_{i,j,k}}^n \right) - \left(\frac{\mathbf{k}_{wm}}{\mu_w \Delta x} \right)_{i-\frac{1}{2},j,k}^n \left(c_{sm_{i,j,k}}^n - c_{sm_{i-1,j,k}}^n \right) \right] - [\hat{q}_{wm}]_{i,j,k}^n - [\phi_m c_{t,m}]_{i,j,k}^n \frac{p_{wm}^n}{\Delta t_m} \quad (4.12)$$

The solute concentration in rock matrix is calculated from continuity equation for solute in matrix from Equation 4.7 as,

$$c_{sm_k}^{n+1} = \frac{\Delta t}{(1 - \epsilon_{vm})_k^{n+1} \phi_m V_k} q_{sm} + \frac{[(1 - \epsilon_{vm}) S_{w,m} c_{sm}]_k^n}{(1 - \epsilon_{vm})_k^{n+1}} + \frac{\Delta t}{(1 - \epsilon_{vm})_k^{n+1} \phi_m \Delta z_k} * \left\{ \begin{aligned} & \left[c_{sm} \frac{\mathbf{k}_{wm}}{\mu_w \Delta z} \left(\omega + \frac{\rho_w}{\rho_s} \frac{c_{sm}}{1 - c_{sm}} \right) \right]_{k+\frac{1}{2}}^n \left[p_{wm_{k+1}}^{n+1} - p_{wm_k}^{n+1} - \gamma_w (D_{k+1} - D_k) \right] \\ & - \left[c_{sm} \frac{\mathbf{k}_{wm}}{\mu_w \Delta z} \left(\omega + \frac{\rho_w}{\rho_s} \frac{c_{sm}}{1 - c_{sm}} \right) \right]_{k-\frac{1}{2}}^n \left[p_{wm_k}^{n+1} - p_{wm_{k-1}}^{n+1} - \gamma_w (D_{k+1} - D_k) \right] \\ & - \left[\frac{\omega RT_m}{V_w} \nabla c_{sm} \right]_{k+\frac{1}{2}}^n \frac{c_{s_{k+1}}^n - c_{s_k}^n}{\Delta z_{k+\frac{1}{2}}} + \left[\frac{\omega RT_m}{V_w} \nabla c_{sm} \right]_{k+\frac{1}{2}}^n \frac{c_{s_k}^n - c_{s_{k-1}}^n}{\Delta z_{k-\frac{1}{2}}} \\ & - \phi_m D^{eff} \left(\frac{c_{s_{k+1}}^n - c_{s_k}^n}{\Delta z_{k+\frac{1}{2}}} - \frac{c_{s_k}^n - c_{s_{k-1}}^n}{\Delta z_{k-\frac{1}{2}}} \right) \end{aligned} \right\} \quad (4.13)$$

From the mathematical model, the concentration of the pore fluid as it imbibes vertically through the core due to osmotic diffusion is determined. The model has the same parameters of the triaxial cell test, in that the core is initially saturated with deionized water, then an 18 wt. % NaCl solution is introduced at the base of the core. The properties of the rock including the dimensions, porosity, permeability, and stress state are entered into the model. Results from the model agree with a portion of the measured resistivity data, though discrepancies from the measured resistivity are believed to have error as they were a previous iteration of design to the newest resistivity setup, being the two probe method instead of the four probe method. Previous work has shown that four probe measurement produce lower measured total resistivity in comparison to that of the two probe method and are not affected by probe or contact resistance (Mahmood et al. 1991; Sharma et al. 1991). A comparison of the model to the measured data is presented in Figure 4.4 where the solid lines represent the models predicted concentration over time, and the dotted points are the experimentally measured data. As it can be seen, the simulation of the concentration of NaCl between probes 0 and 1 closely match the measured data. This shows a strong result and promotes the use of resistivity measurements to track the brine solutions imbibition through the core. Tracking the brine concentration enables a better understanding of the osmotic pressure and how the brine flows through the core.

The measurements between electrodes 1 to 2 and 2 to 3 do not match as closely to the predicted data. The almost instantaneous increase in the concentration from Probe 1-2

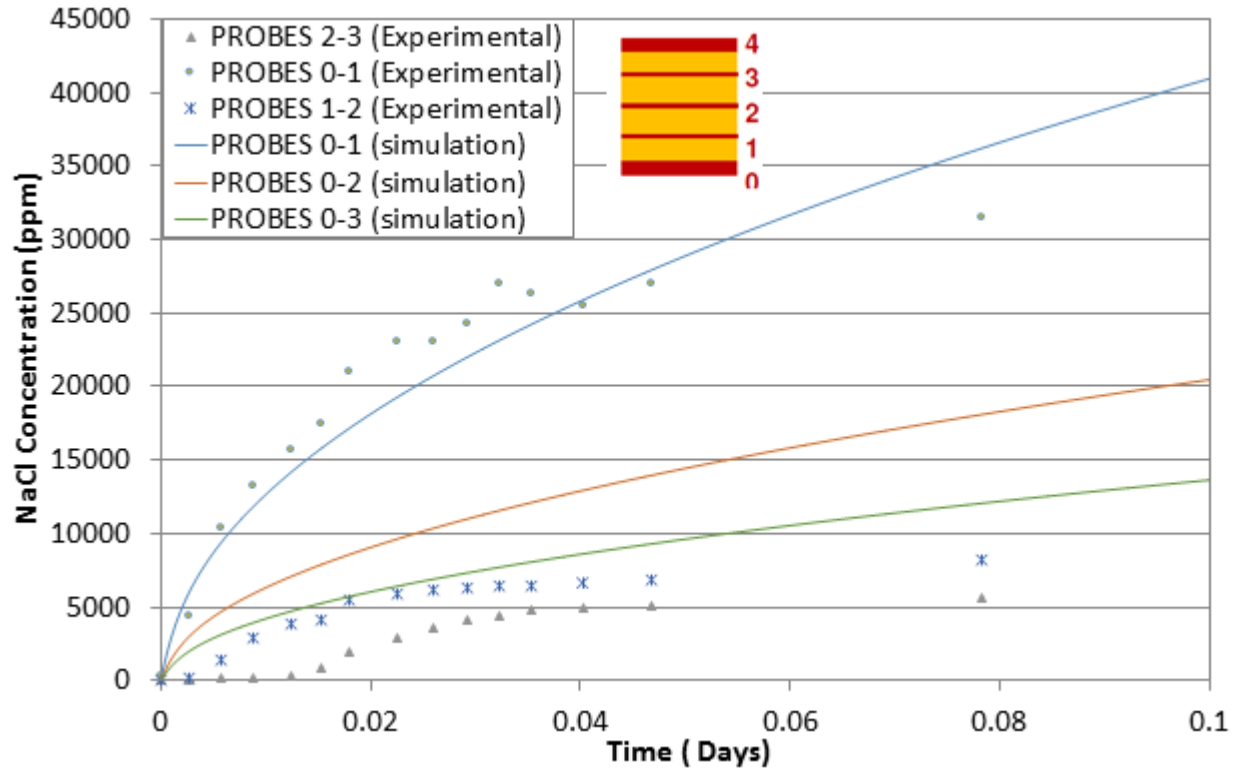


Figure 4.4: Results from the model showing the concentration of NaCl brine moving through the core in comparison to the calculated concentration due to measured resistivity. It is seen that the electrodes 0 and 1 show a strong relation with the model, where as the results for 1-2 and 2-3 vary from the models prediction.

shows that a leak in the seal, or fracture is present. If the measured results matched that of the model, the conductivity of Probe 1-2 would not decrease immediately with the initiation of the 18wt.% brine; rather, a time period of zero concentration would exist until the brine reaches the height of Probe 1. This same trend would occur for the other electrode probe intervals that the concentration of the solute would not increase immediately, but would be delayed as the distance from the point of injection increases. This delayed response is exhibited in the measurements of Probe 2-3, where the concentration is almost zero until a definitive increase at roughly 0.015 day time. The determined concentrations are also low for Probes 1-2 and 2-3. This may be due to the inherent issue with two probe resistivity recording greater values of resistivity than that of the four probe setup. If the four probe setup was used, it is likely that the measured resistivity would be lower and more representative of the

pore fluid. A decrease in measured resistivity would correspond to greater concentrations of NaCl, bringing the measured data closer to alignment with the predicted concentrations.

4.3 Difficulties Tracking Brine Concentration Flow in Shales

Implementing resistivity measurements for shale samples is simple to perform, but very challenging to interpret. There are many more factors which can drastically affect the measured resistivity being presence of conductive minerals, complex pore structure, bedding angle, anisotropy, rock-fluid interaction, and more. The same method to track the concentration of the brine fluid moving through a core as shown in 4.2 was attempted to be implemented for shales; however, there were drastic errors between the model and experimental data. There are a multitude of factors which affect the resistivity measurements which could have created the large difference between the measured and predicted concentrations. First, it is the way which shales are deposited and during the maturation process, as well as the mineral diagenesis consumes most of the sea water saturating the rock matrix until irreducible saturation occurs, with the possibility of sub-irreducible saturation to occur. This leaves minimal conductive water for electrical current to flow, increasing the measured resistivity (Wang et al. 2009). Coupling the large volumes of pyrobitumen, limits the pore space available for water storage. These effects cause increased resistivity values in shales disregarding the effects of hydrocarbon presence in the pore space.

Looking at the resistivity results from the shale tests it is observed that there are two distinct trends, a higher set of resistivity measurements from the higher electrodes and a lower set of values from the lower electrodes. Figure 4.5 shows the results that resistivity measurements taken with electrodes 3 and 4 show a much greater value of resistivity in comparison to the measured resistivity from electrodes 1 and 2. This may be due to the precipitation of salts within the base of the core from the high concentration (60,000ppm) brine initial saturation. Found in the research of Padin (2016), FE-SEM images after the osmosis shale tests showed precipitated NaCl crystals within fractures that surround calcite grains as shown in Figure 4.6. These images, and the precipitation of the salt leads to better understanding

of the flow of water throughout the pore structure of the shale. These deposits and flow path show the complexity of the resistivity measurements. The precipitation of the salts occurring at the base of the sample does make sense, yet understanding how the precipitate affects the measured resistivity is very challenging. As the conductive salts are deposited throughout the rock pore structure not only do they alter the pore geometry, effectively decreasing resistivity. The deposits of the conductive salts also increase the conductivity. These opposing affects are almost impossible to determine how each individually affects the resistivity measurements over time as more salts precipitate out through the duration of the osmosis test, which causes a continuously changing pore geometry and slowly increase the volume of the precipitated salt. Couple this with the compounding effects of the altering stress state due to the osmotic pressure build up and the change in effective stress places many factors which influence the measured resistivity.

When attempting to create a correlation between the measured resistivity and the concentration of the brine solution as it imbibes through the core, results were not consistent with the model, or even close. This is vastly due to the complexity of the interpretation and adjustment of the resistivity for shales. Calculating the electrical efficiency factor (Equation 4.1) as in the method of Herrick and Kennedy, is nearly impossible due to the complexity of the shales as described. Without an accurate rock electrical efficiency, a correlation between the measured resistivity and the conductance of the brine imbibing through the core is not possible. Determining exact values for wettability, the complex pore structure, and rock fluid interaction would take much more in depth and challenging experimental work which was initially out of the scope for this project. Only estimates of these parameters were made to try and determine the electrical efficiency, and create the resistivity to concentration relation. On top of this, with the shale samples there are the effects of osmotic pressure which increases the pore pressure, decreasing effective stress. As calculated earlier in Section 3.4, the effect of osmotic pressure on resistivity measurements is analyzed and shown that the increases in pore pressure creates lower resistivity measurements.

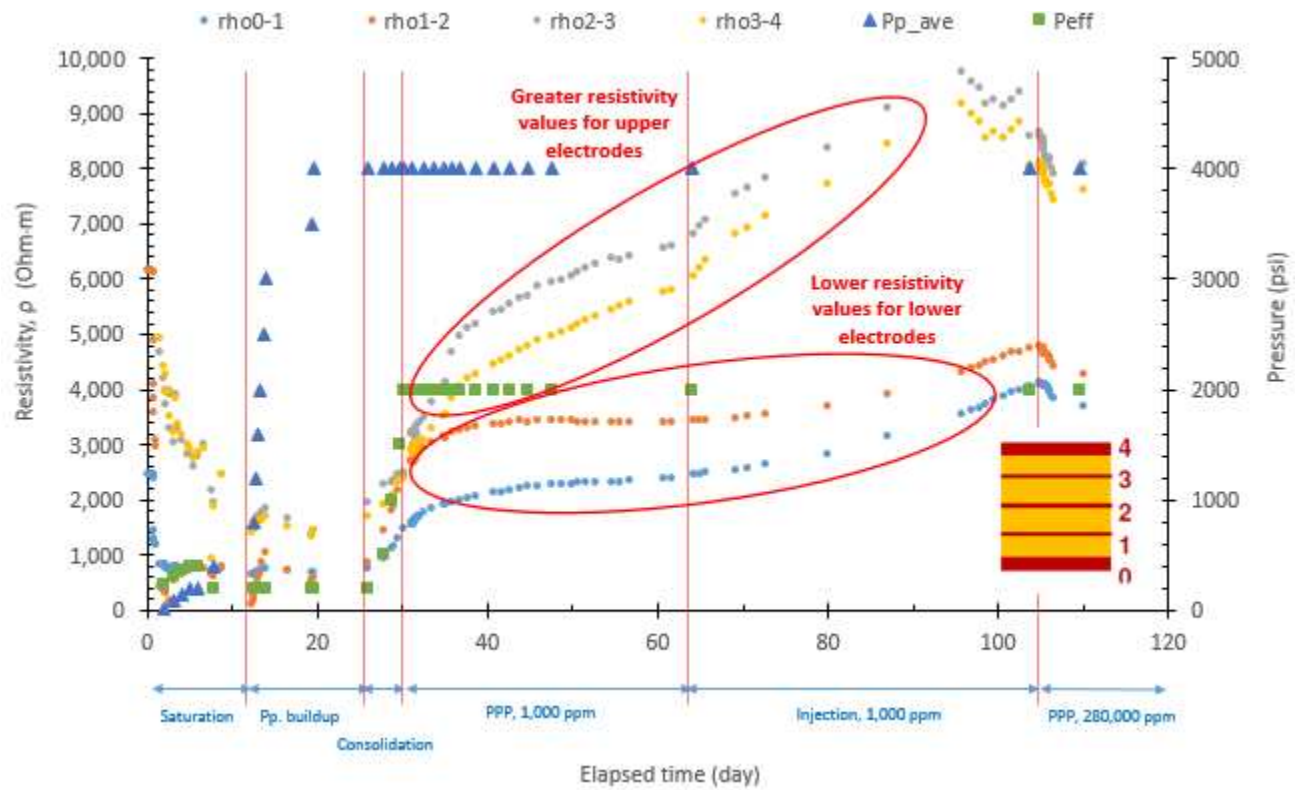


Figure 4.5: Results of the Eagle Ford shale resistivity osmosis test show that the upper electrodes 3 and 4 show much greater resistivity in comparison to the lower electrodes 1 and 2 which show much lower resistivity results. This could be due to salt precipitation within the pore space, increasing the volume of conductive minerals, thus decreasing the resistivity.

Overall, when examining the results for shale measurements and attempting to create a model showing the location of the different brine concentration front moving through the core, the measured resistivity is too complicated to correctly interpret for shales. There are several factors attributing to the electrical properties of the rock and not all could be effectively or accurately solved for.

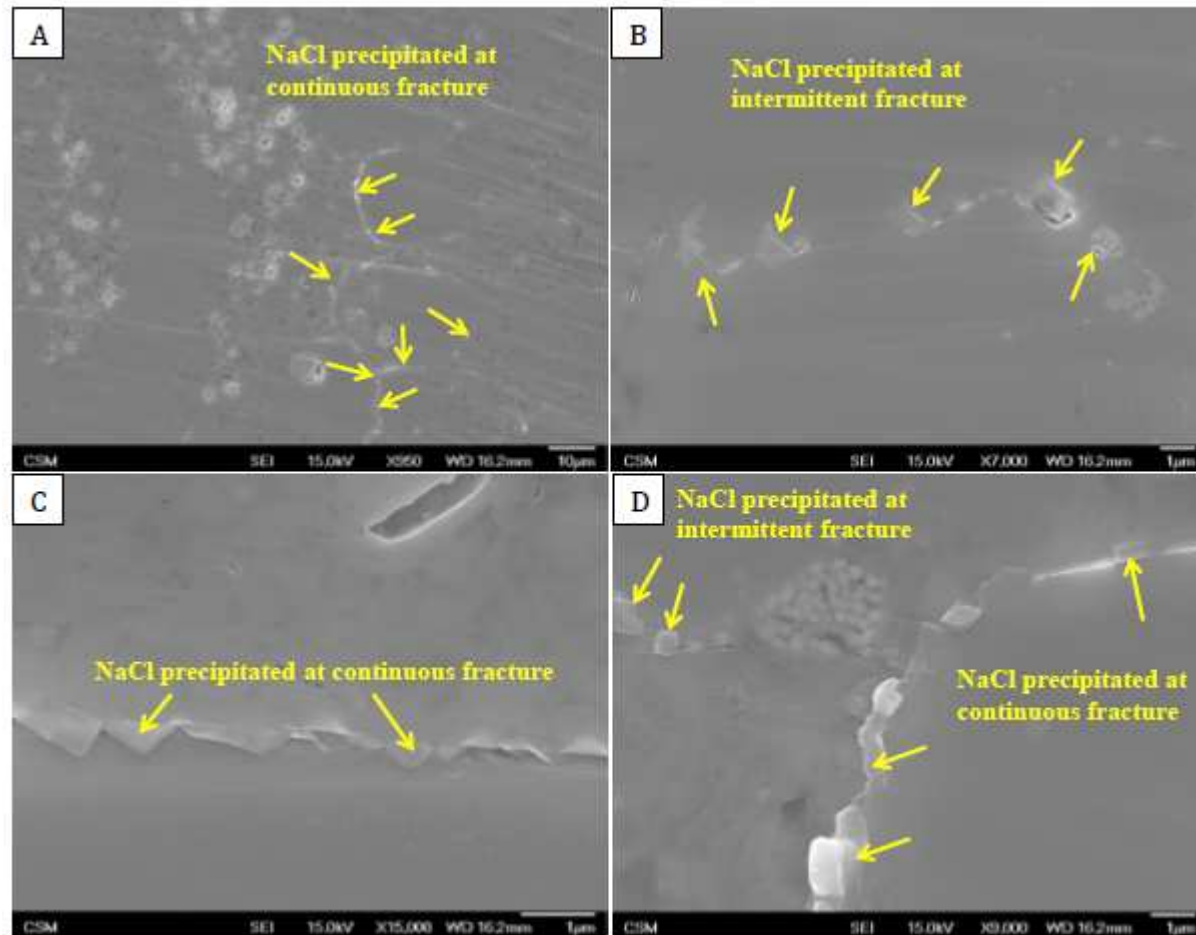


Figure 4.6: FE-SEM images showing the precipitation of salt taken after the completion of pore pressure penetration tests. (A) NaCl precipitation throughout a continuous fracture. (B) precipitation of NaCl in open spaces of an intermittent fracture. (C) and (D) other examples of NaCl precipitation (Padin 2016).

CHAPTER 5

LIMITATIONS AND APPLICATIONS OF THE RESEARCH RESULTS

In this chapter, the limitations of the experimental research study are discussed and conclusions are presented. Moreover, the conventional and unconventional implementation areas for the field applications are introduced. The research performed and detailed in this study is fundamental in nature and has been conducted under controlled laboratory conditions. Direct application of the findings determined from this study would not be true to the understanding of this fundamental work. Explained in this section are the conditions for the experimental study and the conclusions which can be drawn from them.

5.1 Limitations

The limitations of this research study for direct field applications have been covered in detail in this section. Due to the controlled laboratory conditions which this experimental study is undertaken, the findings from this study cannot be directly implemented in the field. For example, the test samples used were CT scanned for imaging the sample conditions and checked for fracture presence before each test and after the experiment is completed. In hydrocarbon bearing formations, it is evident that large natural fracture networks are abundant throughout the formations. The presence of fractures would greatly decrease resistivity measurements and skew the interpretation. Because of these fractures and other factors affecting the electrical properties of the hydrocarbon bearing formations discussed here, the findings of this study must be expanded to incorporate to also capture field application and use in the reservoir models.

5.1.1 Controlled Experimental Conditions

The tests performed in this experimental study were conducted at in situ stress state with each sample carefully prepared and checked for how intact they are before use, and the

conditions has been monitored throughout the duration of the experiment. For the sandstone sample used in the study, the sample was used due to its cleanliness, i.e. low clay composition, to track fluid migration. The core sample was cleaned using toluene to hydrocarbons from the pore space. Significant care was taken for precise preparation of both the sandstone and the shale samples used in the osmosis tests to prevent any shale swelling, or any effects of the electrical properties of the rock due to conductive mineralogy or interference from the presence of the hydrocarbons. In field applications, clays and conductive mineralogy are present; clay not only swell resulting a change in the pore geometry, but also decreases resistivity due to the conductive characteristics of the clay minerals. For the fundamental experimental study presented in this thesis, it is essential to investigate one parameter at a time in order to eliminate several factors simultaneously affecting the electrical properties and isolating the specific affects one at a time. The stress conditions, axial, confining and pore pressures, were controlled using computerized high precision syringe pumps, and the fluids injected were maintained at a constant salinity.

If multiple factors controlling the electrical properties, it is not possible to accurately determine the effects of the single factor in question in one experiment. This changing of one factor at a time is highly challenging in shale samples. The shale core samples drilled and preserved from the Eagle Ford, Bakken, and Pierre were not cleaned, have a volume of clay which swells, and an unknown volume of conductive mineralogy. Not only do the volumes of conductive mineralogy affect the resistivity measurements, but the distribution of these minerals throughout the complex pore system will be another factor impacting the measurements. The number of unknown factors affecting the electrical properties of shale samples makes it very challenging to correctly interpret the results from the resistivity measurements during the osmosis tests as multiple parameters affect the electrical properties of measurements.

Compounding the effects on the electrical properties of the shale samples in laboratory conditions is the fact that in field conditions there is another level of unknowns. Shale forma-

tions do not have constant mineralogy, water saturation, hydrocarbon saturation, stress, and other factors which further complicate the understanding of the results of the resistivity. It is not possible to accurately predict or model field conditions for the electrical properties of the rocks undergoing osmosis until further experiments are performed to isolate the different factors affecting shale samples.

5.1.2 Utilizing Resistivity for Tracking Injection Well Fluid Flow

To gain a better understanding on the practical results of the results of the experimental study, the findings should be implemented into a full scale reservoir model. The experimental results of this research study are utilized as accurate input parameters at other modeling research studies, in particular the multiscale, multiphysics numerical simulator incorporating the rock-fluid interactions and swelling as part of the driving mechanisms for EOR applications in shale reservoirs that was developed by Bui (2016) at Mines UNGI group for to investigate the use of low-salt concentration brines in enhancing the oil recovery. When injecting low-salinity brine into a reservoir with an in situ high-salt concentration will overtime increase resistivity measurements due to the low-salinity brine distributing throughout the reservoir, driving in situ fluids towards production wells. Performing logging tool runs at initial conditions, then periodically performing additional logging runs will add the fourth dimension (time) to the resistivity.. Examining how the reservoir electrical properties change over time will show the spread or flow of the injection fluid throughout the reservoir. However, there are many other factors which would influence the electrical properties change over time which were not investigated or fully interpreted in this research study for shales. During production and injection operations, there would be clay swelling, changing the pore geometry; alterations in the stress state due to compaction, depletion, and pore pressure draw down; generation or closure of fractures due to production and injection; production of hydrocarbons and in situ fluids changing the fluid type and consequently the fluid conductivity; change in conductive mineralogy due to either salt precipitation or dissolving in situ salts.

The factors which affect the electrical properties, as just previously explained, are challenging to interpret in field analysis and have not been emphasized in this experimental study for shales. The relation between resistivity and effective stress, permeability, and brine salt concentration in sandstones has been emphasized in this study instead. These relations are shown while maintaining constant properties to observe these specific relations. For further field application of this research study, further experimental studies will be required to isolate the effects of clay swelling, pore pressure depletion, production of hydrocarbons, compaction, fracturing, and changes in the conductive mineralogy.

5.1.3 Sensitivities Affecting Resistivity

The electrical properties of rock are very sensitive to changes in salinity or potential natural fractures present in the formation. Natural fractures are abundant throughout hydrocarbon bearing reservoirs and the boom in shale production introduces hydraulic fracturing to aid in hydrocarbon recovery. Similar to the effects of fractures on permeability, measured resistivity is highly affected from fractures creating a super-highway for current to pass through. Running resistivity well logs are affected greatly by the fractures within the rock formations surrounding the wellbore. Much lower values of resistivity would be observed due to the presence of fractures. Within the experimental setup for this research study, each sample was examined for fractures as the fracture would skew the results for the osmotic pressure tests, as well as resistivity. Specific samples were selected which did not have large fractures, while the micro fractures were closed during consolidation as seen in the stress dependent permeability section, (3.2). Further work to examine the effects of fracturing on resistivity would be very useful for the interpretation of field logs, potential use of resistivity to identify fracturing, and for application into computer based modeling efforts.

The sensitivity of resistivity measurements in field logs makes interpretation very challenging. One such example is utilizing resistivity for determining reservoir pore pressures. Due to in situ fluid salt concentrations greatly varying from formation to formation, or

even within the same formation, a vast array of pore pressures would be interpreted due to the changes in the electrical properties. These erroneous interpretations would show sharp changes in the pore pressure, where in truth the pore pressure is constant but other factors affecting the electrical properties are changing. Normally, sonic log data is used to determine such properties as pore pressures, mechanical properties, and for fracture analysis due to the more reliable dependence on the rock type, stress state and structure. Under laboratory conditions, due to the precise and constant conditions, the resistivity measurements do not fluctuate as significantly as in field measurements.

Formation damage during drilling, workover, and fracture operations can highly affect the measured resistivity through the use of logging tools. The reading depth of logging tools may not suffice the required depth to overcome the damages to the formation. Fractures occurring from these operations will greatly lower the measured resistivity, or conversely the resistivity will increase if the mudcake is very thick and impermeable. Even the deepest reading logging tools account for the electrical properties, or formation damage, at the wellbore. Highly fracture formations due to drilling or any operations will greatly affect the measured resistivity, and consequently affect the interpretation of the log data.

CHAPTER 6

CONCLUSIONS AND RECOMMENDATIONS

The goal of the experimental study presented here was to investigate the stress dependence of the electrical properties in rocks, and to develop a system in which an injected brine solution could be tracked as it is imbibed through the core. The research detailed in the preceding chapters can be summarized into the following conclusions with the limitations in mind as previously explained.

- It was observed that resistivity measurements are affected by very subtle geometric differences due to increased effective stress or rock-fluid interactions compared to the P-wave velocity measurements as described in Section 3.3 of this thesis study. At effective stresses greater than 1,000 psi, it is observed that the P-wave velocities do not present significant changes while the resistivity measurements showed increases in resistivity at the same increased effective stress level. The increase in resistivity signifies changes in the pore structure of the rock with the increased stresses, which would not have been observed if only P-wave measurements were used. This observation of the electrical resistivity being more sensitive in comparison to the P-wave velocity data should be stated that this is only true for precise experimental stress state applied. Such a relation may not be apparent for field log interpretation for resistivity due to the complexities of the electrical properties of rocks as described in the limitations section (5.1).

- Resistivity could be direction dependent or hysteretic due to the strong dependence and correlation between resistivity and permeability. During permeability measurements, the direction of gas flow is reversed to determine if the permeability is directionally dependent. As shown in Section 3.2.4, there is a clear difference between the permeability measured with flow occurring from the bottom to top, and from the top to bottom. The direction of flow would alter the fines migration, producing different pore geometry. The change in the

pore geometry and distribution of potentially conductive minerals within the pore structure will alter the electrical properties of the rock formation. The directional dependence of resistivity is apparent due to the deposition of the clay particles (1.3.4) due to the natural flow of electrical current being parallel to the clay platelets. In laboratory work, the bedding planes of the shale samples is controlled in conjunction to the direction of flow. Within field conditions bedding planes can intersect the wellbore at varying angles due to geologic conditions, as well as the curvature of the wellbore. Real world field conditions will further complicate the interpretation of the measurements as the electrical properties are further affected by the angle between the bedding and logging tool (1.3.6).

- Resistivity measurements must be adjusted for interpretation of the effective stress effect. As is clearly shown in this research study and in the literature, resistivity is highly dependent on the effective stress state of the rock (1.3.1). During osmotic pressure tests, the pore pressure increases due to ion diffusion, which alters the effective stress state and consequently affects the measured resistivity. As discussed in detail in Section 3.4, the resistivity must be adjusted due to the effects of the rock-fluid interactions creating decreased effective stress. If not, erroneously calculated estimates of the water saturation, hydrocarbon saturation, porosity and other electrical properties will be determined.

Also presented in this study is the delay in response of the resistivity measurements to the changing rock stress in comparison to the predicted model. This delay represents the reaction which the rock has to change in stress, and that it is not instantaneous, but rather a slightly slower process. Understanding the effects of effective stress is also required for log interpretation for field logs. The effective stress does not only change due to osmotic pressure as described here. Depletion of the reservoir, depending on the drive mechanisms, will decrease pore pressures; thus, increasing effective stress and compacting the reservoir potentially. This would further affect the electrical properties of the rock, not only changing the effective stress state on the formation but also changing the fluid type within the reservoir.

During drilling operations invasion of the mud into the formation through natural fractures or drilling induced fractures will also cause clay swelling. The swelling of clay particles will change the pore geometry of the rock, altering the measured resistivity; another factor which must be accounted for.

- Resistivity measurements can be used to track a fluid front moving through a sandstone core. A relation between the measured brine resistivity and the concentration of a given salt must first be determined. Knowing the relation for brine concentration and resistivity a correlation between the total or bulk resistivity can be formed with the concentration as shown in Equation 6.1. Calculating the electrical efficiency of the rock, and knowing the porosity and saturation, the concentration of the brine from the measured resistivity is determined. As ion diffusion occurs the concentration of the pore fluid will slowly change to the saturating fluid. Measuring the concentration with differently spaced electrodes will enable to the tracking of the fluid front as it moves through the core. Experimental data is matched with a mathematical model which calculates the diffusion of salt through a specified porous rock structure, and shows a strong resemblance to the observed experimental efforts. Further work must be performed for a similar correlation to be determined for shale reservoir formations; however, the complexities of the electrical properties of shale are very challenging and will require extensive interpretation of the measured total resistivity to isolate the changes in the resistivity due to only the concentration change of a brine.

$$C_{NaCl} = \left(\frac{(E_o R_t S_w \phi)}{4036.1} \right)^{\frac{-1}{0.952}} \quad (6.1)$$

For field implementation of utilizing osmosis for EOR purposes through injection wells, resistivity may be used to aid in tracking the fluid migration through the reservoir as fluids are produced through production wells. However, due to the changes of the electrical properties of the rock from depletion, pore pressure draw down, fines migration, change in salt concentrations, and many other factors it would be impractical to utilize this fundamental understanding in shale reservoirs due to the lack of understanding of the effects of the listed

factors on the electrical resistivity log.

- The NaCl brine injected into the shale cores precipitated into NaCl crystals along the flow paths of the pore channels. This salt precipitation increases the volume of the conductive minerals within the shale while also decreasing the cross sectional area to flow. Both of these factors affect the measured resistivity measurements. What is more challenging is that the precipitation cannot be measured throughout the test, unless the cell is placed within an imaging device which is capable of capturing the fine, nano-scale precipitates.

- During hydraulic fracturing operations the formation surface area in contact with fracturing fluids within a formation is increased due to the increased length, width, and number of fractures created in result of the fracturing operations. It is important to understand that the rock fluid interaction will have a greater effect due to the increased contact area with a higher density fracture network. All the effects on the electrical properties as discussed in these conclusions will be compounded due to the greater contact area with the rock formation.

Future work to further the experiments and results in this thesis research study should include the full use of four probe resistivity measurements in shale cores to measure the change in resistivity due to changes in salt concentration. The base knowledge and model have been setup in this study; however, the complexities of the electrical properties of shale formations are very challenging and require extensive research to be able to isolate how the change in salt concentration affects the resistivity. Accurately characterizing the tortuosity, wettability, cementation, volumes of conductive minerals, and anisotropy is essential to then accurately determine the concentration of the brine solution. Also, the precipitation of salts throughout the osmosis tests leads to an unknown factor of the conductive material increasing in volume within the pore space. An understanding of the volume of precipitate over time, where it occurs, and how it effects the measured resistivity would be required for more accurate understanding of the resistivity concentration correlation for shales.

REFERENCES CITED

- Ahr, W. 2011. Geology of carbonate reservoirs: the identification, description and characterization of hydrocarbon reservoirs in carbonate rocks. *John Wiley and Sons*.
- Archie, G. 1942. The electrical resistivity log as an aid in determining some reservoir characteristics. *SPE Journal*, **146**(01): 54–62. URL <http://dx.doi.org/http://dx.doi.org/10.2118/942054-G>.
- Bittar, M. and Rodney, P. 1996. The effects of rock anisotropy on mwd electromagnetic wave resistivity sensors. *The Log Analyst*, **37**(01): 20–30.
- Brace, W., Orange, A., and Madden, T. 1965. The effect of pressure on the electrical resistivity of water-saturated crystalline rocks. *Journal of Geophysical Research*, **70**(22): 5669–5678.
- Clavaud, J. 2008. Intrinsic electrical anisotropy of shale: The effect of compaction. *Society of Petrophysicists*, **49**(03): 243–260.
- Clavaud, J., Nelson, R., and Wang, H. 2005. Field example least of enhanced hydrocarbon estimation in thinly laminated formation with a triaxial array induction tool: A laminated sand-shale analysis with anisotropic shale. In *SPWLA 46th Annual Logging Symposium*. New Orleans, Louisiana, U.S.A.
- Clavier, C., Coates, G., and Dumanoir, J. 1984. Theoretical and experimental bases for the dual-water model for interpretation of shaly sands. *Society of Petroleum Engineers*, **24**(02): 153–168.
- Davies, J. and Holditch, S. 1998. Stress dependent permeability in low permeability gas reservoirs: Travis peak formation, east texas. In *SPE Rocky Mountain Regional/Low-Permeability Reservoirs Symposium*.
- Dobrynin, V. 1962. Effect of overburden pressure on some properties of sandstones. *Society of Petroleum Engineers*, **2**(04): 360–366.
- Fakcharoenphol, P., Kurtoglu, B., Kazemi, H., Charoenwongsa, S., and Wu, Y. 2014. The effect of osmotic pressure on improve oil recovery from fractured shale formations. Paper SPE-168998-MS presented at SPE Unconventional Resources Conference, The Woodlands, Texas, USA. URL <http://dx.doi.org/http://dx.doi.org/10.2118/168998-MS>.

- Farrokhrouz. 2007. Rock mechanic characterization of shale formations based on wellbore drilling log data. *Petroleum University of Technology, Tehran, Iran*.
- Flugel, E. 2010. Carbonate depositional environments in microfacies of carbonate rocks. *Springer Berlin Heidelberg*, 7–52.
- Glanville, C. 1959. Laboratory study indicates significant effect of pressure on resistivity of reservoir rocks. *Journal of Petroleum Technology*, **11**(04): 20–26.
- Gupta, K., Gupta, P., Singh, G., Kumar, S., Singh, R., and Srivastava, R. 2013. Changes in electrical properties of bones as a diagnostic tool for measurement of fracture healing. *Hard Tissue*, **2**(1).
- Herrick, D. 1988. Conductivity models, pore geometry, and conduction mechanisms. SPWLA 29th Annual Logging Symposium.
- Herrick, D. and Kennedy, D. 1993. Electrical efficiency: A pore geometric model for the electrical properties of rocks. Paper at SPWLA 34th Annual Logging Symposium, Calgary, Alberta.
- Herrick, D., Kennedy, D., and Yao, T. 2001. Calculating water saturation in electrically anisotropic media. *Society of Petrophysicists and Well-Log Analysts*, **42**(02): 118–136.
- Hsieh, P., Tracy, J., Neuzil, C., Bredehoeft, J., and Silliman, S. 1981. A transient laboratory method for determining the hydraulic properties of 'tight' rocks-i. theory. *International Journal of Rock Mechanics and Mining Sciences*, **18**(3): 245–252.
- Javalagi, M., Morriss, S., and Chenevert, M. 1991. Time lapse resistivity and water-content changes in shale. Paper SPWLA-1991-AAA presented at SPWLA 32nd Annual Logging Symposium, Midland, Texas.
- Josh, M., Esteban, L., Piane, C., Sarout, J., Dewhurst, D., and Clennell, M. 2012. Laboratory characteristics of shale properties. *Journal of Petroleum Science & Engineering*, (88): 107–124.
- Kamath, J., Boyer, R., and Nakagawa, F. 1992. Characterization of core scale heterogeneities using laboratory pressure transients. *SPE Formation Evaluation*, **7**(03): 219–227. SPE-20575-PA.
- Kennedy, D. 2006. The porosity-water saturation-conductivity relationship: An alternative to archie's model. 47th Annual Logging Symposium, Veracruz, Mexico.
- Kennedy, D. and Herrick, D. 2012. Conductivity models for archie rocks. *Geophysics*, **77**(03): 109–128.

- King, H., Eberle, A., Walters, C., Kliewer, C., Ertas, D., and Huyng, C. 2015. Pore architecture and connectivity in gas shale. *Energy and Fuels*, **29**(3): 1375–1390.
- Klein, J. 1996. Saturation effects on electrical anisotropy. *The Log Analyst*, **37**(01): 47–49.
- Klein, J., Martin, P., and Allen, D. 1997. The petrophysics of electrically anisotropic reservoirs. *The Log Analyst*, **38**(03): 25–36.
- Kuila, U. 2013. *Measurement and Interpretation of Porosity and Pore-Size Distribution in Mudrocks: The Hole Story of Shales*. Ph.D. thesis, Colorado School of Mines.
- Kunz, K. and Moran, J. 1958. Some effects of formation anisotropy on resistivity measurements in boreholes. *Journal of Geophysics*, **23**(4): 770–794.
- Longeron, D., Argaud, M., and Feraud, J. 1989. Effect of overburden pressure and the nature and microscopic distribution of fluids on electrical properties of rock samples. *SPE Formation Evaluation*, **4**(02): 194–202.
- Loucks, R., Reed, R., Ruppel, S., and Hammes, U. 2012. Spectrum of pore types and network in mudrocks and a descriptive classification for matrix-related mudrock pores. *AAPG Bulletin*, **96**(6): 1071–1098.
- Mahmood, S., Maerefat, N., and Chang, M.-M. 1991. Laboratory measurements of electrical resistivity at reservoir conditions. *Society of Petroleum Engineers Formation Evaluation*, **6**(03): 291–300.
- Mese, A. 2008. Clay-water interaction, intermolecular forces and acoustic velocity. In *SEG Annual Meeting*. Society of Exploration Geophysicists.
- Moran, J. and Gianzero, S. 1979. Effects of formation anisotropy on resistivity-logging measurements. *Journal of Geophysics*, **44**(7): 1266–1286.
- Padin, A. 2016. *Experimental and Theoretical Study of Water and Solute Transport Mechanisms in Organic-Rich Carbonate Mudrocks*. Ph.D. thesis, Colorado School of Mines.
- Patnode, H. and Wyllie, M. 1950. The presence of conductive solids in reservoir rocks as a factor in electric log interpretation. *Society of Petroleum Engineers Journal of Petroleum Technology*, **2**(02): 47–52.
- Redmond, J. 1962. *Effect of Simulated Overburden Pressure on Some Selected Sandstones*. Ph.d., Pennsylvania State University.

- Rine, J., Dorsey, W., Floyd, M., and Lasswell, P. 2010. A comparative sem study of pore types and porosity distribution in high to low porosity samples from selected gas-shale formations. *AAPG Search and Discovery*.
- Schlumberger, C., Schlumberger, M., and Leonardon, E. 1934. Some observations concerning electrical measurements in anisotropic media, and their interpretation. *Transactions AIME*, **110**: 159–182.
- Sharma, M., Garrouch, A., and Dunlap, H. 1991. Effect of wettability, pore geometry, and stress on electrical conduction in fluid-saturated rocks. *The Log Analyst*, **32**(05): 511–525.
- Suman, R. and Knight, R. 1997. Effect of pore structure and wettability on the electrical resistivity of partially saturated rocks-a network study. *Geophysics*, **62**(4): 1151–1162.
- Taylor, S. and Barker, R. 2002. Resistivity of partially saturated triassic sandstone. *Geophysical Prospecting*, **50**(6): 603–613.
- Tiab, D. and Donaldson, E. 2012. *Petrophysics*. Elsevier, 3rd edition.
- Wang, Z., Gelius, L., and Kong, F. 2009. Simultaneous core sample measurements of elastic properties and resistivity at reservoir conditions employing a modified triaxial cell. *European Association of Geoscientists & Engineers Geophysical Prospecting*, **57**(06): 1009–1026.
- Winsauer, W., Shearin, J., Masson, P., and Williams, M. 1952. Resistivity of brine-saturated sands in relation to pore geometry. *AAPG Bulletin*, **36**: 253–277.
- Woodruff, W., Revil, A., and Torres-Verdin, C. 2014. Laboratory determination of the complex conductivity tensor of unconventional anisotropic shales. *Geophysics*, **79**(05): E183–E200.
- Worthington, P. 1982. The influence of shale effect upon the electrical resistivity of reservoir rocks. *Geophysical Prospecting*, **30**(5): 673–687.
- Wyble, D. 1958. Effect of applied pressure on the conductivity, porosity and permeability of sandstones. *Journal of Petroleum Technology*, **10**(11): 57–59.
- Wyllie, M. and Rose, W. 1950. Some the considerations related to the quantitative evaluation of the physical characteristics of reservoir rock from electrical log data. *Journal of Petroleum Technology*, **2**(04): 105–118.

APPENDIX A - MATERIALS, METHODS AND LABORATORY PROCEDURES UTILIZED TO STUDY THE DEPENDENCE OF RESISTIVITY ON STRESS

The objective of Appendix A is to detail the techniques utilized to better understand the stress dependency of the resistivity measurements under in situ stress conditions. A multitude of additional measurements were taken to aid in the understanding of the resistivity measurements and osmotic pressure tests. Explained in this Appendix will be bulk density, porosity, pore size distribution, Field Emission Scanning Electron Microscope, resistivity and triaxial pore pressure penetration tests.

A.1 Porosity

Understanding and determining porosity aids in the characterization of the samples utilized in this work. Porosity influences not only storage volume but also rock elasticity, strength, electrical properties and other rock properties. It has been found in previous experimental work that the strength of shale decreases with a non-linear trend with increasing porosity (Farrokhrouz 2007). For this work we relate the pore geometry to the electrical resistivity.

A.1.1 Absolute Porosity

Porosity is challenging to measure in shales as the fine grains are easily blown away, or not maintained for weight measurements. For this precision scales must be used. The absolute porosity is calculated as follows; where ρ_{bulk} is the bulk density of the shale sample and ρ_{solids} is the density of the solid grains once the sample is crushed.

$$\phi = 1 - \frac{\rho_{bulk}}{\rho_{solids}} \quad (A.1)$$

A.1.1.1 Bulk Density

Bulk density is determined by following the procedure: Initial sample weight is measured, in this work a Sartorius Precision Balance with an error $\pm 0.001 \text{ grams}$; the sample then needs to be cleaned utilizing the Dean-Stark distillation extraction method as described by the Gas Research Institute, 1996 with pure liquid toluene for 72 hours due to the extremely low permeability of the shale sample. Toluene is a neuro toxin so special care must be taken when using this chemical. Cleaning the sample with toluene extracts any hydrocarbon or water which could be trapped in the pore spaces. Measuring the sample weight before and after cleaning can find the weight percentage of liquids in the core as well. Below in Figure A.1 are images depicting the scale and cleaning process.

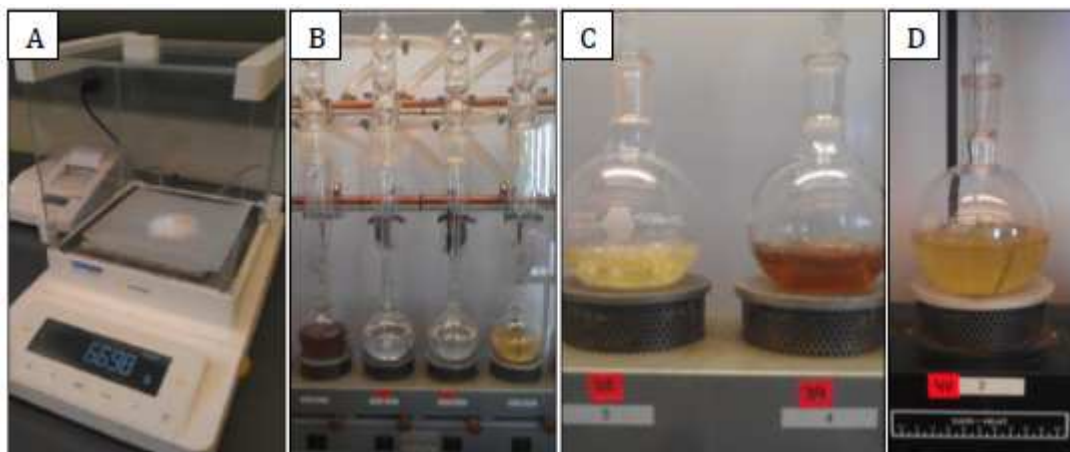


Figure A.1: (A) The Sartorius Precision Balance with an error ± 0.001 grams. (B, C, D) Images showing stages of the Dean-Stark cleaning process (Padin 2016).

After completion of the initial weight, cleaning and secondary weight measurements, the bulk density can be determined. The sample, after weighed, is immersed in mercury to determine the bulk volume. The mercury lab at Colorado School of Mines contains a precision apparatus, as seen in Figure A.2. The bulk volume is measured, then using the weight of the grains the density is calculated as the following, A.1.1.1.

$$\rho_{bulk} = \frac{Weight}{Volume}$$

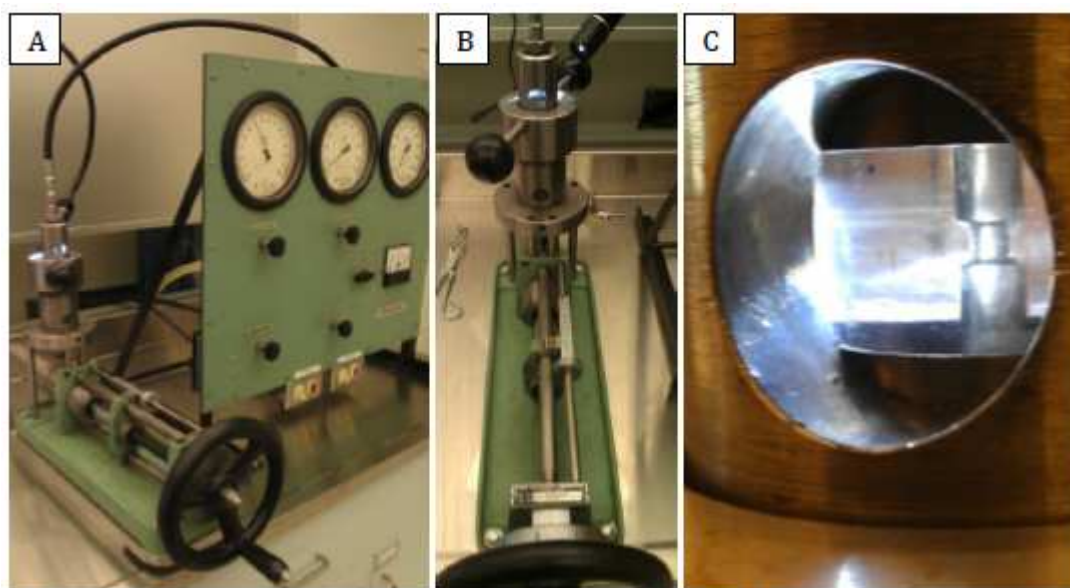


Figure A.2: The bulk density measurement setup within the mercury lab at CSM with an error of $\pm 0.1\text{cc}$. (A) A general view of the machine. (B) The calibrated mercury volume chamber. (C) The sample chamber calibration point (Padin 2016).

A.1.1.2 Pycnometer Grain Density

To determine absolute porosity, the final variable required is the grain density. For this the sample is tested using a water pycnometer originally designed for use in soils. The rock sample is crushed and passed through a $150\text{-}\mu\text{m}$ sieve, instead of the called for 4.75mm sieve due to the smaller particles of shale. The volume of the crushed sample is found with the pycnometer. The following procedures were used to determine the specific gravity of the solids.

- 3 pycnometer measurements are performed per sample, at each core depth, for consistency. Each sample is dried in an oven maintained at 165°C for 3 days to properly dry the sample.
- Each sample is crushed using a mortar and pestle. The crushed sample is then sieved using a $150\text{-}\mu\text{m}$ mesh (No. 100) sieve. Some larger pieces which were not totally crushed did not go through the sieve, but these small unbroken pieces were then crushed until all passed through the sieve.

- The solids which passed through the No. 100 sieve were then fed into a funnel which is placed into the pycnometer.

- Water is added until the water level rises up to $\frac{1}{3}$ of the depth of the chamber within the pycnometer. The water-solids mix is then agitated until a uniform slurry is formed. Any powder stuck to the pycnometer is rinsed down into the slurry.

- A vacuum is then pulled over the sample to de-air the slurry mixture. To ensure all the air is removed the pycnometer is continually agitated under vacuum for 2 hours. After the 2 hour period the vacuum is maintained for 48 hours to ensure the samples are free of air.

- Filling the pycnometer with the de-aired water is performed using a small-diameter flexible pipette. The pipettes outlet is kept just below the surface of the slurry in the pycnometer so that no air is introduced into the slurry. The mass of pycnometer, soil, and water is measured to the nearest 0.01g. The temperature setting is set to the ambient conditions within the room for proper calibration.

The output of the pycnometer reading is the volume of the grains (V_p), which is determined using A.2:

$$V_p = \frac{(M_{pw,c} - M_p)}{\rho_{w,c}} \quad (\text{A.2})$$

where ($M_{pw,c}$) is the mass of the pycnometer at the prescribed calibration temperature in grams, (M_p) is the average of the dry pycnometer in grams, and ($\rho_{w,c}$) is the density of water at the specified temperature in (g/ml).

The specific gravity of the crushed solid is calculated by the following Equation A.3:

$$G_t = \frac{\rho_s}{\rho_{w,t}} = \frac{M_s}{(M_{\rho_{wt}} - (M_{\rho_{ws,t}} - M_s))} \quad (\text{A.3})$$

where (ρ_s) is the bulk density of the solids in (g/cc), ($\rho_{w,t}$) is the density of the water at the prescribed test conditions in (g/cc), (M_s) is the mass of the dried crushed sample in grams and ($M_{\rho_{ws,t}}$) is the mass of the combination of the pycnometer, water and solids at the prescribed temperature in grams.

A.1.2 Scanning Electron Microscope

Scanning Electron Microscope images are used due to the very fine grain size being less than $62\mu m$, conventional optical microscopy cannot be used for such fine details. The greater magnification capabilities of the electron microscopes enables better image quality and consequently better analysis of these images for shales. From these images texture, composition and porosity can be seen to within nanometer scale. Scanning electron microscopy produces images by recording and analyzing signals from the interactions of an electron beam with the chosen sample. The physics behind the measurements are out of the scope of this work, however the procedure is described.

There are four types of emitted electrons which the SEM use to create images.

- Type I secondary electrons (SE1) emit with a high angle at a close proximity from the impact point and thus carry high-resolution, surface-sensitive (topographic) information of the sample.
- Type II secondary electrons (SE2), on the other hand are generated from a deeper and wider volume than the SE1 and reflect at a lower angle, therefore carrying intrinsically lower-resolution topographical information.
- Single scattered backscattered electrons (BSE1) tend to emit at a high angle and are closely linked to compositional contrast.
- Multiple scattered BSE (BSE2) take off at a lower angle and are used to characterize composition and crystalline structures of a sample.

Two types of analysis are applied to understand the microstructural characteristics of shale samples. The instruments used for the analysis are a conventional SEM and an FEI Quanta-600i Environmental Scanning Electron Microscope. The conventional SEM can be used with various types and shapes of samples and has magnification capabilities ranging from 15x to 20,000x. Three types of images can be produced, SE1, BSE1, and BSE2 as described above. Simultaneous elemental analysis is also possible due to a PGT Spirit Energy Dispersive Spectrometer which detects and plots X-rays which are emitted from

the sample. The second tool, the FE-SEM is used in conjunction with tungsten cathode and PGT Energy Dispersive Spectrometer. The combination of these tools work under low vacuum conditions. Because of this ability this tool is convenient for its use with organic rich rocks that expel gas when exposed to the atmosphere.

To prepare the sample for testing exacting precision must be taken to create a smooth surface. To ensure a smooth surface, an Ion-milling tool is utilized. First a JOELIB-19500 Cross Section Polisher is used to polish the surface which is parallel to bedding. The shale sample used is a hand cut 5x8x2.5mm sample, so rather small. The polisher uses an argon beam to mill and polish the exposed cross section. The polishing beam is coupled with a optical microscope to ensure a perfect positioning of the surface and consequently polishing the surface. To prevent any scoring of the surface from the beam the sample is rocked back and forth. Milling took 10 hours per sample. With the sample prepared, the shale can then be placed into the JOEL JSM-7000F Field Emission Scanning Electron Microscope for imagery to be taken.

A.2 Triaxial Cell Pore Pressure Penetration Tests

To perform a successful test to determine the interaction of fluids with the matrix and the transport mechanisms that dominate water and oil flow in mudrock formations as required for the osmotic pressure tests, key to the success is the correct design and implementation of a methodical set of tests. The following section explains, the materials and methods used for the pore pressure penetration tests. Most influential on the accurate and consistent results is the design, construction and calibration of the different components of the testing apparatus. The test setup took over two years to correctly bring together the required tools, instruments, knowledge and equipment for coupled measurements.

A.2.1 Sample Preparation

It is a known standard that core plugs used in conventional geomechanical testing typically have a height to diameter ratio of 1-2.5" (Fjaer et al 2008), yet in our experiments

shorter length samples (1.0”) were used due to the very low permeability of our samples. A valid concern in experimental work is the validity of the sample investigated to be representative of real in situ conditions at the experimental conditions. For example, for unconventional reservoirs, there is a large natural fracture network which contributes to the surface contact of the matrix with the injected fluid. It is known that stress release has the greatest effect on a rocks geomechanical properties (Fjaer et al 2008), and our tests must represent accurate stress, and accurate geomechanical properties. The relevant properties for accurate representation of the reservoir rock are those with fractured rock mass; thus, it would be ideal if samples containing fractures be used for the representation pore pressure penetration tests. Due to the goal to study the physics behind transport phenomena, intact samples were preferred. Though, all shale contain nano-fractures, which are still present throughout the intact cores. Common failures within a sample can be seen below in Figure A.3.

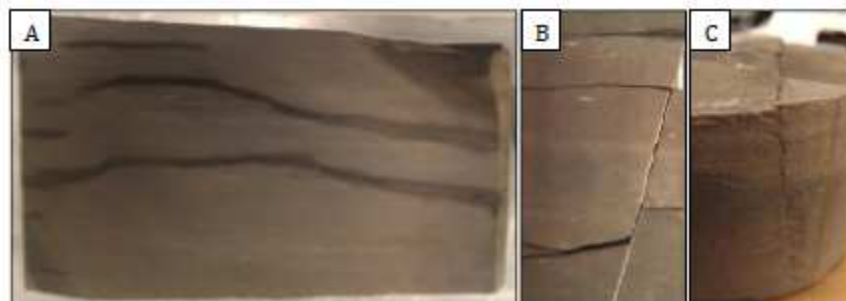


Figure A.3: (A) Preserved 1-foot core sample (B) A vertical and horizontal fracture which are common throughout the cores and must be avoided (C) A vertical fracture which propagated while trying to create parallel edges (Padin 2016).

The samples utilized in this experimental work are obtained using cores from two Eagle Ford wells (GZ and LS), from Gonzales and La Salle Counties, Texas, USA, respectively and one core from a Bakken well in North Dakota. To minimize natural fluid loss and prevent any damage from atmospheric exposure, the 1-foot long samples were immediately sealed by the outfit drilling the cores as soon as they came to surface. Each core was wrapped in a plastic film and then again wrapped in aluminum sheets, finally the cores were covered in wax. It is important to maintain the in situ fluids and before testing bring the sample back

to in situ conditions with fluids and stresses. The pore pressure penetration tests require rock sample cylinders of 1.5 inch diameter and lengths varying between 0.5 to 1.5 inches. The smaller plugs must be drilled out of the preserved core sections. An image of the process is seen in Figure A.4.

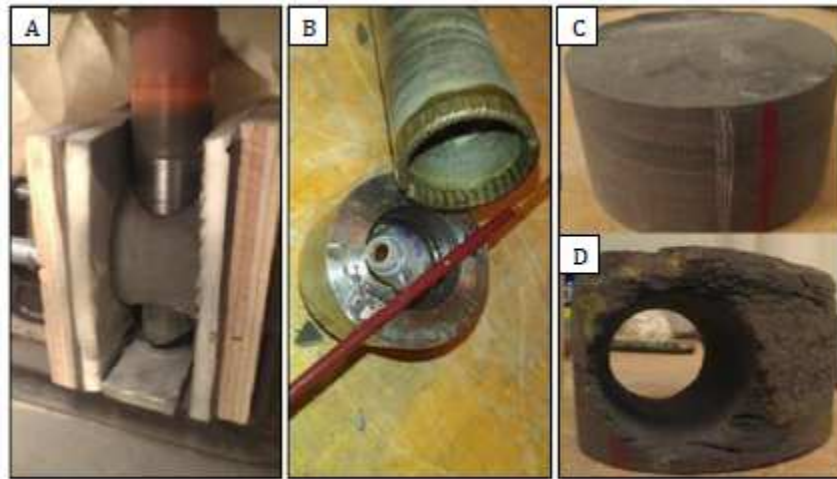


Figure A.4: Example of the core being drilled and plugs taken. (A) A core being held in place for a plug to be drilled. (B) A diamond tipped drill. (C) A preserved core sample. (D) A drilled core sample (Padin 2016).

To obtain the plugs from the larger cores they must be drilled very carefully and cut with a diamond saw as not damage them. The use of a soft rubber sheet is to protect the sides of the core will clamping it down for the plug to be drilled. A diamond bit coring drill is used to cut the plug out. No fluids can be used while drilling, this creates a lot of dust so proper PPE must be worn. Once a long section of the plug is drilled the plug is then cut to appropriate length. Each core is cut with a diamond edge cutting blade at a slow rotational speed which does not surpass 500RPM. Once cut to length the core must be sanded down to achieve perfectly parallel end surfaces. If the ends are not parallel concentrated stress will form at the raised edges and negatively affect the results of the experiment, or create fractures through the rock. To create the parallel top and base a lathe is used to trim the piece perfectly. As a final measure sand paper is used to sand down small imperfections. Images from sample preparation are presented in Figure A.5.

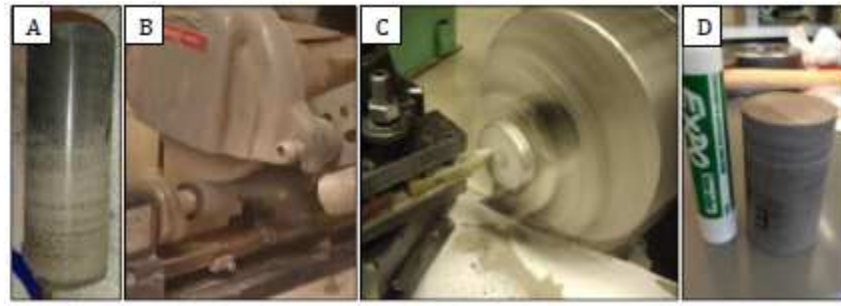


Figure A.5: (A) A dilled plug from a core. (B) Cutting the core to length. (C) Using a lathe to ensure the edges are perfectly parallel. (D) A finished core sample ready for the resistivity measurements to be applied (Padin 2016).

This preparation process is long and very challenging. At many points a sample can fracture and be ruined for the purpose of the osmotic pressure tests. It takes about eight hours to correctly prepare a sample. Each step should not be rushed as it will increase the chances of breaking a sample.

A.2.2 Resistivity Measurements

For the resistivity measurements, the samples had to be carefully prepared as to not use too much conductive epoxy and to not damage the sample. If any electrical short cuts are created during the setup then the whole test will produce pore results. As previously mentioned there are two and four probe measurements taken throughout this work. A description of each method of setup is described in this section. Also, the efforts taken to isolate the sample are detailed.

A.2.2.1 Two Probe Resistivity Setup

The experimental setup for two probe resistivity measurements for a one inch sandstone sample consists of three conductive epoxy electrode rings which circle the sample and are spaced at equal intervals along the sample length. The schematic electrode setup as well as the sandstone sample used in the calibration are shown in Figure A.6. It should be noted that the two porous metal filters which are placed between the brass electrodes and the core

are not seen in this picture. Two probe measurements are performed by sending an electrical current between any two electrodes; for example: zero to one, zero to two, etc. The known source current is then compared to the measured, the difference being the drop in voltage or resistance. For the osmotic pressure tests performed in this work the two probe resistivity measurement method is implemented for initial tests, though is deemed inaccurate after performing two shale tests and changed for the optimal four probe measurement.

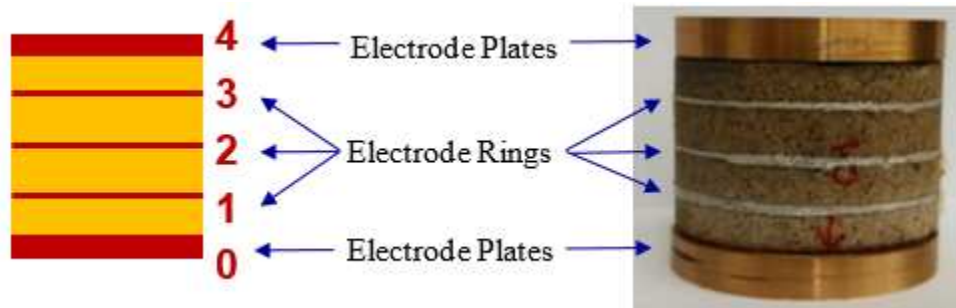


Figure A.6: Designed and actual electrode setup for two probe resistivity sample used in the pore pressure penetration tests.

Modifications were required to the neoprene sleeve covering the core sample during the triaxial tests to isolate the core from the confining pressure fluid invasion. Wires are connected to the electrodes and passed through the neoprene sleeve via small openings. Multiple methods to effectively seal the wire openings were tested. The most consistent sealing method at high pressures was found to be using a combination of two epoxy adhesives to seal a hole just large enough for a wire to pass through. An automotive adhesive, Seal-All, is applied to the small openings made in the neoprene sleeve. Once the first layer epoxy is cured (approximately one hour), a second adhesive layering is applied, 3M Marine Adhesive Sealant, in two layers. The marine adhesive is then cured for twenty-four hours before assembling the triaxial cell. There are a total of five perforations required for the two probe measurements; two perforations for the brass plates, and three for the electrode rings which all need the described sealing procedure prior to the resistivity tests.

After a perfectly cylindrical and parallel sample has been obtained, an electrode setup is attached for measuring resistivity. The resistivity electrodes can then be attached to the outer surface of the core sample. To attach the electrodes for the resistivity measurements the following steps are performed: (in Figure A.7, a few of the steps are presented)

- Cut four pieces of blue painters tape 0.235 in. wide and 5.0 in. in length and apply them evenly along the length of the core. There should be three 0.03 in. spaces between each piece of tape.

- Apply conductive epoxy to the sample over the open areas, creating three rings of conductive epoxy.

- Attach a single wire strand to each epoxy ring (total of three), ensuring to cover the wire strand with additional conductive epoxy if required.

- Remove the blue painters tape from the core.

- Place the core into a sealed container to allow for the conductive epoxy to cure for one hour.

- Remove the core from the container and attach a 16 gauge wire lead to each electrode ring using conductive epoxy.

- Place the core into a sealed container to allow for the conductive epoxy to cure for four hours.

- Sand the neoprene sleeve around the areas where slots have been cut to match the wire leads attached to the core.

- Feed the wire leads through the slots in the neoprene sleeve from the inside out.

- Carefully push the core up into the neoprene sleeve, making sure to keep the wire leads aligned with their respective slots.

- Sandwich the core with two porous metal filters placed into the neoprene sleeve from either end.

- Feed the brass electrode wire lead through the respective slot on the top side of the neoprene sleeve, and carefully push the brass electrode into position above the top porous

metal filter.

- Apply gasket sealant to the triaxial cell base piston shaft which the sample will be placed onto.

- Feed the wire lead attached to the piston brass plate through the respective slot on the bottom side of the neoprene sleeve, and carefully slide the neoprene sleeve with core assembly onto the piston.

- Directly apply automotive epoxy to the contact surface between the neoprene slots and wire protrusions.

- Wait one hour for the automotive epoxy to cure.

- Apply a thin layer of 3M Marine Grade Epoxy Sealant to the area surrounding each wire protrusion.

- Wait six hours for the epoxy sealant to cure.

- Apply a second thin layer of 3M Marine Grade Epoxy Sealant above the first layer

- Wait twenty-four hours for the epoxy sealant to cure.

- The testing cell can then be assembled.

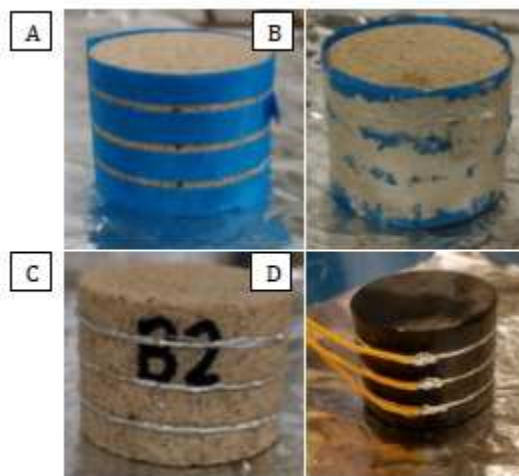


Figure A.7: (A) Sandstone sample with blue taped to mark off the location for the conductive epoxy. (B) Conductive epoxy applied to the sample. (C) Conductive epoxy applied and tapped removed from the sandstone sample. (D) A shale sample with the epoxy applied and wire connected for readings.

A.2.2.2 Four Probe Resistivity Setup

The experimental setup for four probe resistivity measurements consists of two source silver-silver chloride sintered electrodes and two identical potential electrodes. Two potential electrodes are embedded into the side of the sample at equal spacing, as illustrated in Figure A.8. The two source electrodes are embedded in a similar manner, however they are embedded into the two parallel ends. The four probe measurements are performed by sending current through the two source electrodes, and the voltage measured between probes one and two. The difference in the known supplied current and the measured current in the sample is the resistance. This can then be used to determine the resistivity knowing the cross-sectional area of the sample and spacing distance between the electrodes.

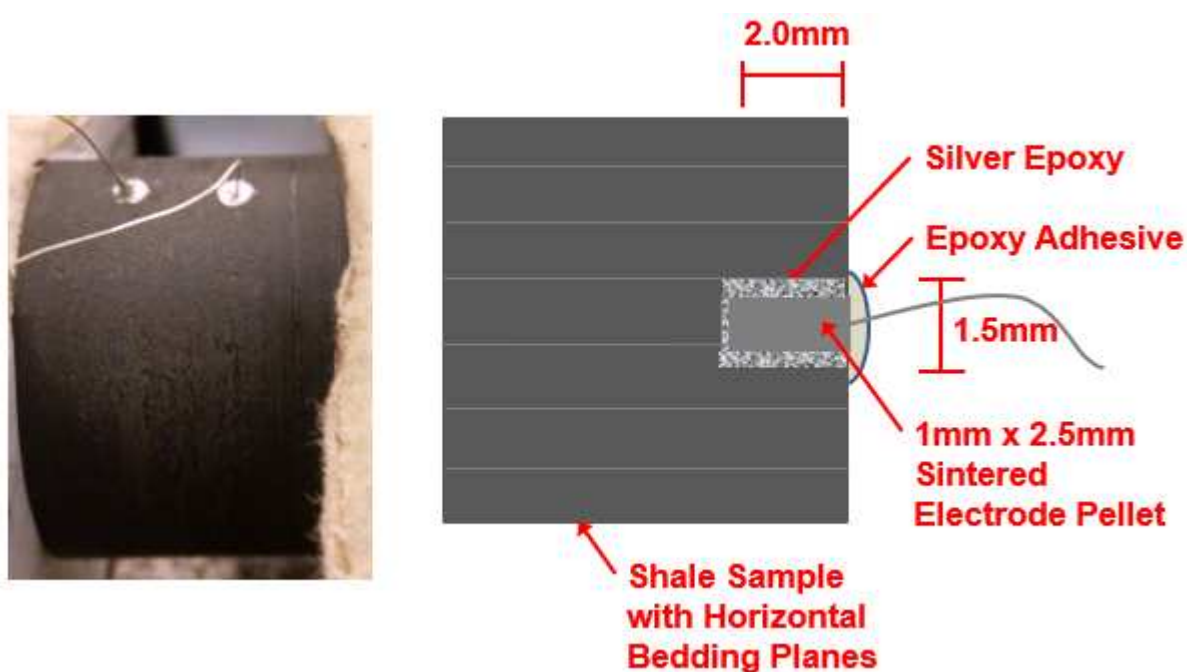


Figure A.8: Four probe setup of a shale sample showing the two potential electrodes embedded into the sample (left), schematic of the imbedded potential electrode to show depth of embedment and orientation to bedding lines (right).

Unlike the two probe setup, there is no need to perforate the neoprene sleeve confining the shale sample. The hair like silver wires extending from the electrodes are run vertically down the shale sample under the neoprene sleeve and exits at the base. This minimizes

potential leak paths for the high pressure confining fluids to enter the shale sample and contaminate the sample. A visual explanation of the four probe setup in the triaxial cell is depicted in Figure 2.5.

After a perfectly cylindrical and parallel sample has been obtained, an electrode setup is attached for measuring resistivity. The resistivity electrodes can then be attached to the outer surface of the core sample. To attach the electrodes for the resistivity measurements the following steps are performed:

- Measure out and mark on the sample every third of the sample length.
- Drill two 1.5 mm diameter x 2.0 mm long holes into the sample utilizing a drillpress.
- Take the two silver-silver chloride electrodes and coat them in a special silver-silver chloride conductive epoxy.
- Place the two electrodes into the two predrilled holes and ensure the conductive epoxy is cleaned around the edges.
- Place the core into a sealed container to allow for the conductive epoxy to cure for four hours.
- Sand the neoprene sleeve around the areas where slots have been cut to match the wire leads attached to the core.
- Feed the wire leads through the slots in the neoprene sleeve from the inside out.
- Carefully push the core up into the neoprene sleeve, making sure to keep the wire leads aligned with their respective slots.
- Sandwich the core with two porous metal filters placed into the neoprene sleeve from either end.
- Feed the brass electrode wire lead through the respective slot on the top side of the neoprene sleeve, and carefully push the brass electrode into position above the top porous metal filter.
- Apply gasket sealant to the triaxial cell base piston shaft which the sample will be placed onto.

- Feed the wire lead attached to the piston brass plate through the respective slot on the bottom side of the neoprene sleeve, and carefully slide the neoprene sleeve with core assembly onto the piston.

- Directly apply automotive epoxy to the contact surface between the neoprene slots and wire protrusions.

- Wait one hour for the automotive epoxy to cure.

- Apply a thin layer of 3M Marine Grade Epoxy Sealant to the area surrounding each wire protrusion.

- Wait six hours for the epoxy sealant to cure.

- Apply a second thin layer of 3M Marine Grade Epoxy Sealant above the first layer

- Wait twenty-four hours for the epoxy sealant to cure.

- The testing cell can then be assembled.

A.2.2.3 Assembling the Triaxial cell for Resistivity Measurements

Once the sample has been prepared and the electrodes attached the triaxial cell can then be setup. First, the impermeable neoprene tube used to isolate the sample from the confining fluids has to be measured and perforated for the resistivity wires to pass through it. The wires from the core are then fed through the new perforations and the sample is carefully placed into the neoprene sleeved and pushed into position. Second, two porous metal filters are placed into the sleeve sandwiching the core. Third, a copper plate with attached wire is placed into the sleeve on the top side. With the neoprene sleeve setup an application of vacuum sealing grease is applied to the end of the axial piston, then finally the core and equipment can then be placed onto the axial piston.

With the core in place the electrical wires can be attached to the cable outputs on the base of the triaxial cell. The setup of the core on the axial piston is seen in Figure A.9. With the wires attached the whole setup must be covered in an epoxy sealant as to prevent any leakage from occurring. At the perforations a two step process has been used with a chemical adhesive applied to the neoprene and wires to strongly seal the perforation. Next the sleeve

and wires are covered in the epoxy sealant. Two layers are applied, the first is applied then left to cure for 24 hours then a second coat applied and left to dry again for 24 hours. Once this step is complete the cell can then be assembled.

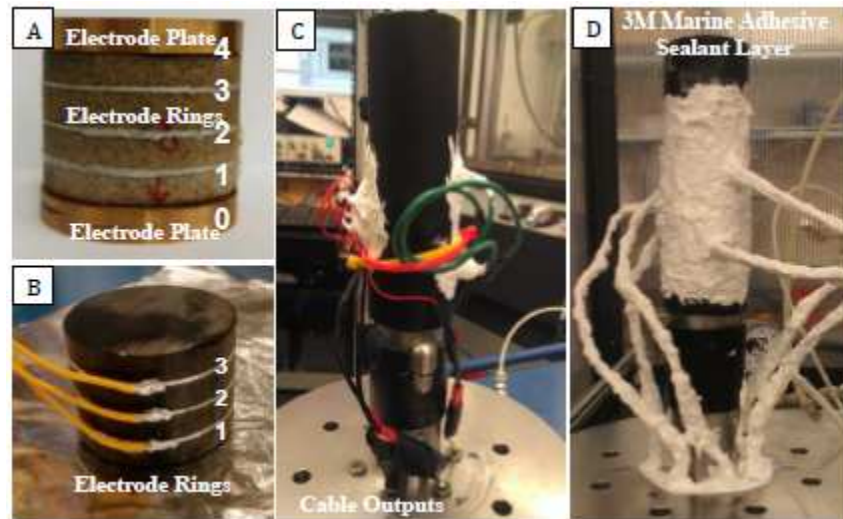


Figure A.9: (A) Sandstone sample with electrodes and sandwiching electrode plates. It should be noted that the porous metal filters go between the electrode plates and the sample. (B) A shale sample with electrodes and wires attached. (C) The axial piston setup and wires connected to the electrical outputs. (D) The entire setup with epoxy sealant to ensure no leakage (Padin 2016).

APPENDIX B - TRIAXIAL CELL ASSEMBLY

With the resistivity measurements portion assembled the entire testing cell can then be assembled. A graphical depiction of the cell and its parts is seen in Figure B.1. The actual cell is seen in Figure B.2 with the internal piston and the cell chamber shown. The key components are displayed as well. This cell is equipped with multiple measurement devices. In the ends of each axial piston sits a sonic measurement transducer. Also, horizontal transducers can be attached to the exterior of the cell chamber; however, during interpretation of the waves it was very difficult to determine the response from the sample from the response of the cell wall and fluid. Attached to the upper piston is a LVDT which measures the vertical strain of the sample. The pressure is measured through a DPT located in the pore pressure system.

Proper maintenance of the cell is required for the long, high-stress testing environment. The O-rings used for the cell must be kept in good working order as they provide the sealing capabilities of the two chambers, confining and vertical stress. Also, there are two O-rings which seal the two ends caps. Aerospace industry grade O-rings are implemented into our test setup being Vitron rubber. When assembling the triaxial cell each O-ring has vacuum seal grease applied to it to aid in its sealing abilities.

To assemble the triaxial cell for testing a set of procedures must be followed as described below:

- Before assembly all tubing, fluid paths, pistons and the interior of the cell must be cleaned with detergent and water then rinsed with distilled water. This ensures that there is no oil or brine left in the tubulars which would contaminate the results. After the distilled water rinse all flow paths should be dried by applying pressurized air.
- Adjustment of the axial piston length should be made to be slightly longer (5-10 mm) than the required length so that it contacts the sample when bolted in place.

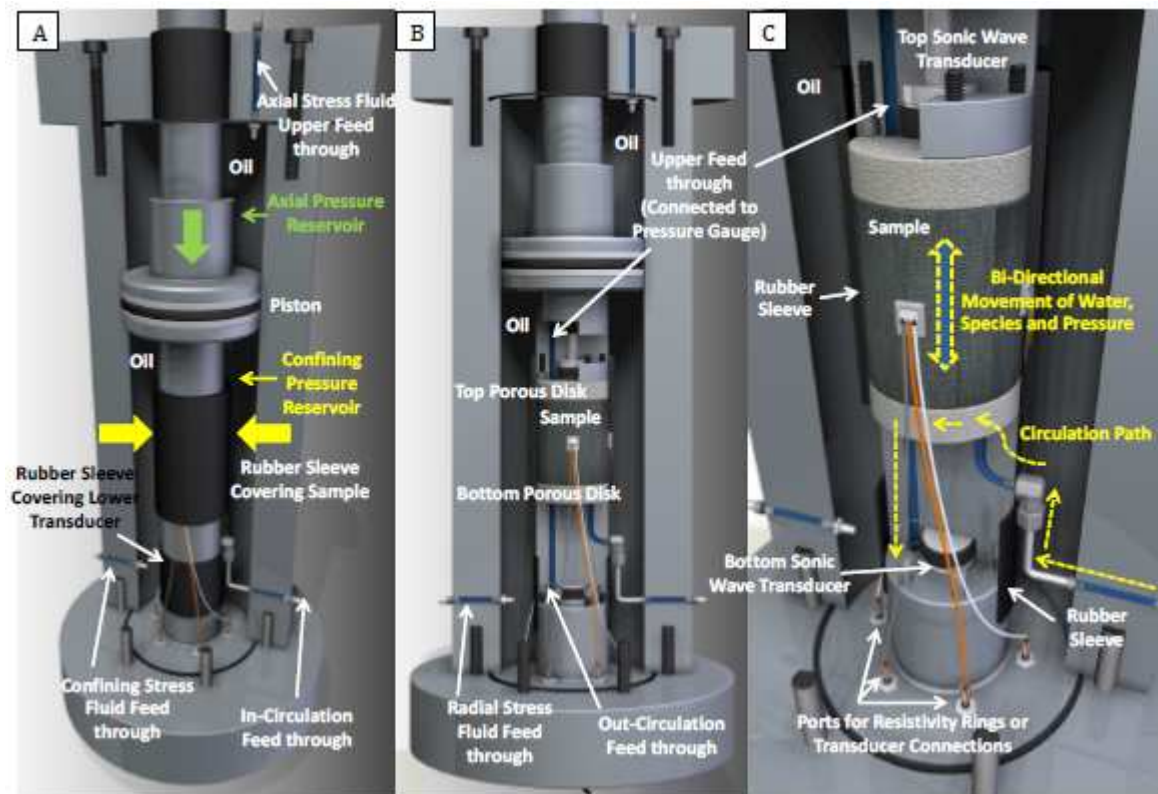


Figure B.1: Solidworks 3D cross section of the triaxial cell with the main components labeled (Padin 2016).

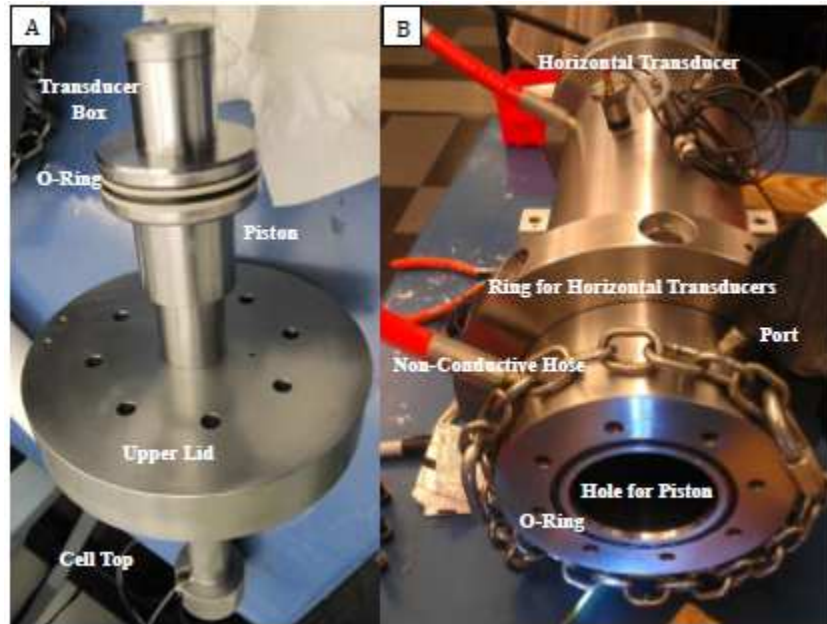


Figure B.2: (A) Internal piston of the triaxial cell which creates the chamber for axial stress and the area where the confining pressure is applied. (B) The main confining chamber which the sample is placed into (Padin 2016).

- With the base axial piston assembled as described in the previous resistivity section, align the base with the triaxial cell and connect the inner base pore pressure line to the input line. Then bolt the base onto the triaxial cell chamber.
- Align the top piston with the correct sonic transducer direction, then slowly insert the piston into the top of the neoprene sleeve. With the piston inserted into the sleeve then slowly push the piston down till it contacts the sample and bolt the upper plate to the cell chamber.
- Fill the upper and lower chambers with hydraulic fluid and cap these ports. The cell can then be hoisted into the temperature controlled cabinet.
- Connect up all the pore pressure, axial pressure and confining pressure lines to the cell.
- Apply vacuum to the top and bottom pore fluid ports and plumb in a vacuum gauge to determine if a vacuum can be held across the sample. If vacuum is maintained when the vacuum pump is turned off then no leaks are present within the sample chamber. If vacuum pressure decreases with absence of a vacuum then a leak is present. If a leak is present the

cell must be disassembled, and more sealant epoxy applied to the neoprene sleeve to prevent leakage.

- Ensuring all connections are tightened down let the testing cell sit in the temperature control cabinet until the required temperature of 40 degrees C stabilizes.
- Apply an axial stress of 133 psi and confining stress of 100 psi. Ensure to first pressurize the axial stress to ensure there is no pinching of the neoprene sleeve if confining stress were to be pressured first.

To pressurize the cell to the desired pressures a series of pumps are used. Two pumps control the pore pressure injection, while three pumps control the hydraulic pressures for vertical and confining stress. The pumps are enclosed within a temperature controlled cabinet with the triaxial cell and all the pipe network as depicted in Figure B.3. There are a set of controllers kept outside of the temperature controlled cabinet to control the pumps and set pump rates, pressures, flow, and a multitude of other control parameters. All the testing equipment have Plexiglas backing plates between the mounts and the frame as to prevent any source current flowing into the cabinet frame which would influence the electrical measurement systems.

To control the flow of fluids, both pore and hydraulic, a simple pipe and valve network was developed. The pipework system allows for complete control and isolation of the sample from pore fluids and hydraulic fluid. Built into the system is a DPT to determine the differential pressure between the upper and lower pore pressures, as seen in the schematic in Figure B.4. The pipes and valves are sourced from Swagelok high pressure equipment. It is also possible to enter a vacuum line into the system as to vacuum any section of the pore pressure lines to de-air the brine solutions.

B.1 Tubing and Valve Specifications

The tubing and valves used in the laboratory setup are sourced from Swagelok due to their quality offerings of high pressure connections, unions, fittings, tubing, and other parts. The majority of the tubing used for this work is 1/8" or 1/16" diameter medium pressure

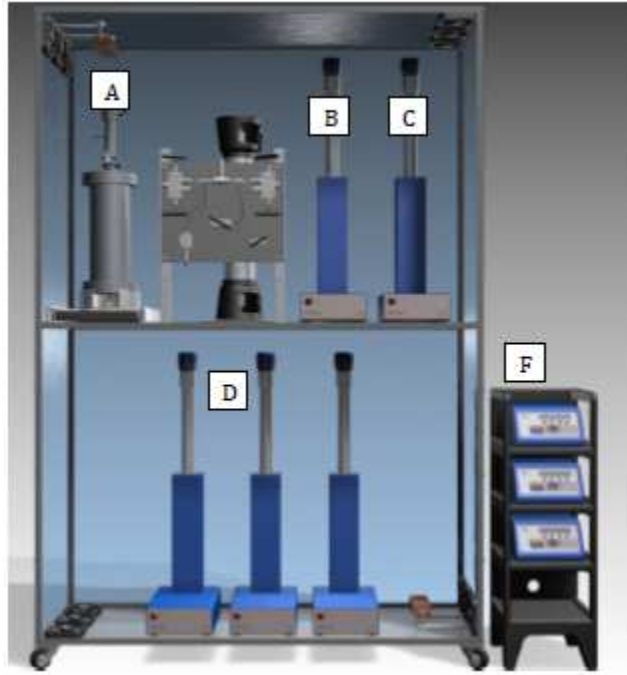


Figure B.3: A graphical representation of the test setup, (A) Is the testing cell, (B and C) are the pore pressure pumps, (D) are the hydraulic pumps and (F) is the electrical pump control units (Padin 2016).

Swagelok FK series stainless steel pipe work. These pipes and fittings can maintain pressures up to 20,000 psi and due to the stainless steel material will avoid any rust and minimize chemical reactions, though for the brine solution used no chemical reaction will occur during this experimental work. The valves used throughout the system are the Swagelok Sno-Trik need valves which can withstand fluid pressures up to 45,000 psi and are also made of 316L seamless stainless steel.

Additionally four non-conductive high-pressure hoses were added into the system to prevent electrical current passing through the stainless steel pipework. The non-conductive hoses are placed between valves 11 and 12, 15 and 9, between the cell confining pressure port and 22, and between the cell axial pressure port and 20. The non-conductive hoses cannot be used with gas, rather only fluid. For the gas permeability measurements these sections of pipe work were replaced with stainless steel equivalents as to prevent the non-conductive hoses from bursting. An image of the non-conductive hoses is seen in Figure B.5.

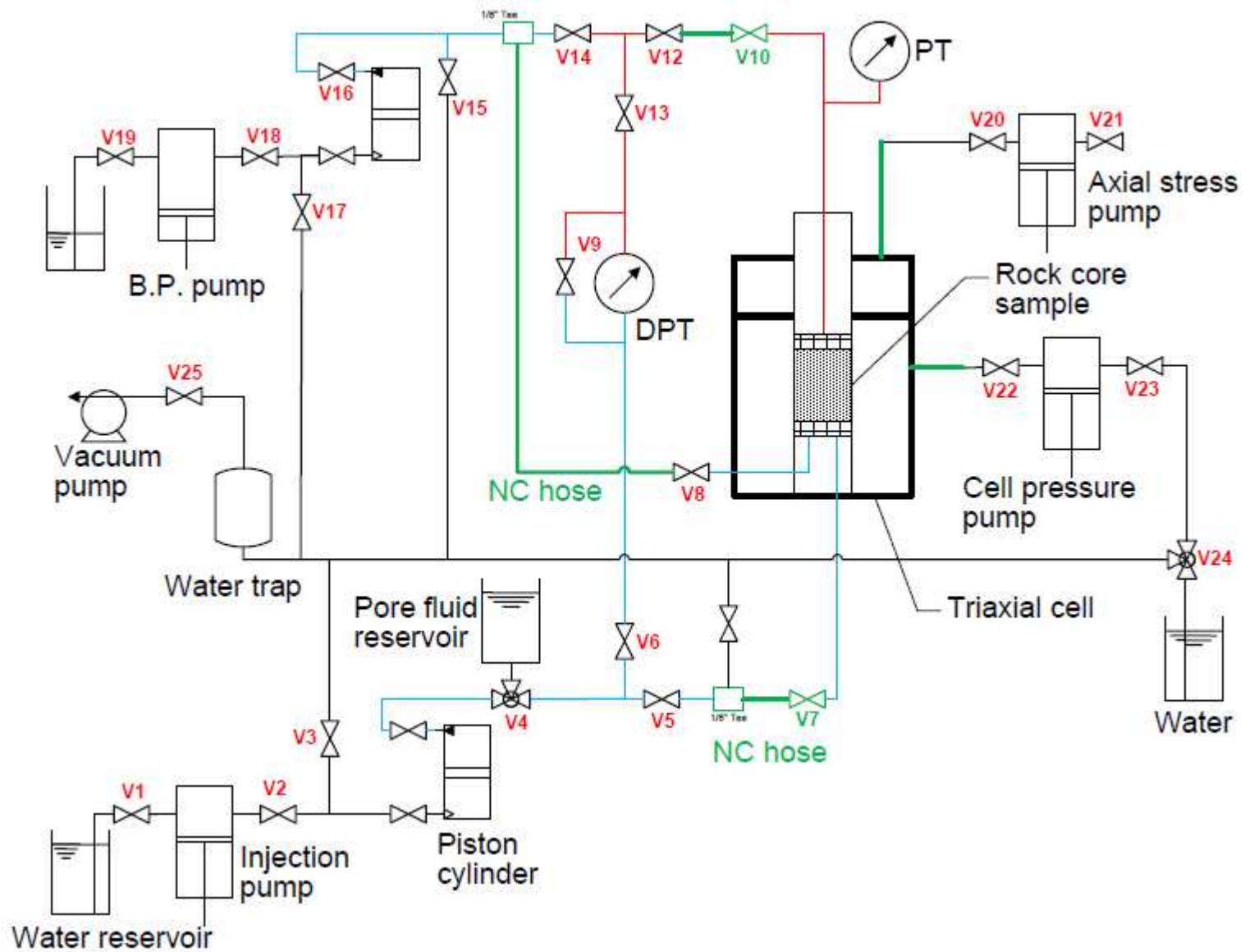


Figure B.4: Schematic representation of the pipe system to control the flow of fluids for the triaxial cell.

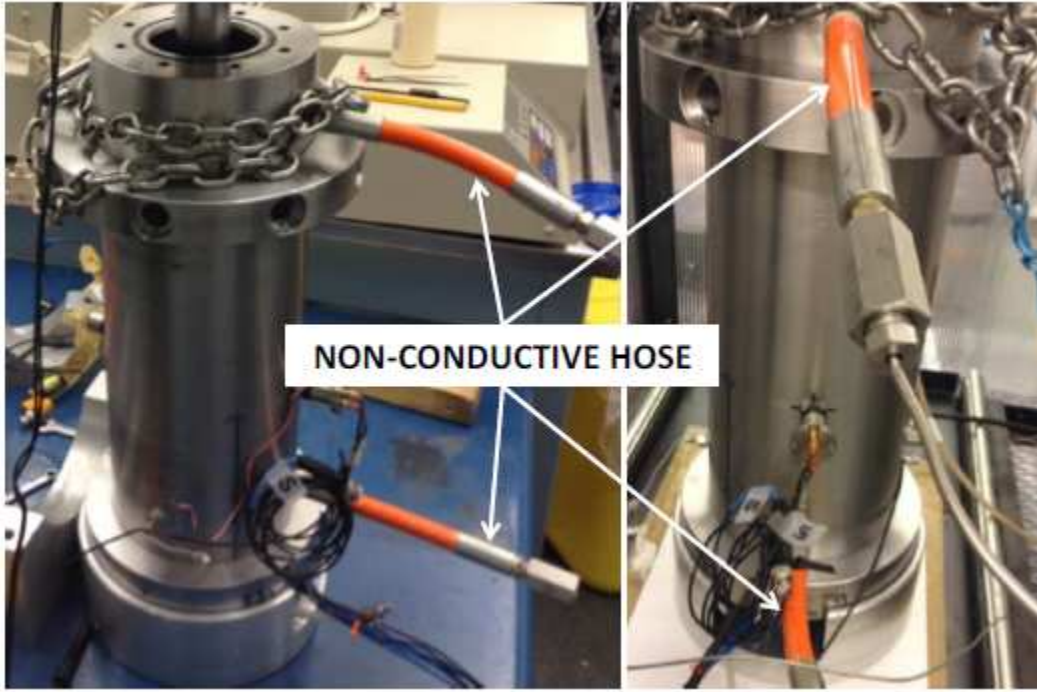


Figure B.5: Connection of non conductive hoses to the triaxial cell confining and axial pressure ports (Padin 2016).

B.2 Axial and Confining Stress Control

It should be first noted that the cell used in this work can only achieve isotropic conditions, meaning the cell can apply an axial stress and singular confining stress. Both stress are applied using hydraulic fluid. The axial piston is drive downward to create axial stress on the sample by pressurizing an upper axial chamber. The confining stress is applied simply by pressurizing the area surrounding the core sample with a hydraulic fluid. To determine the required axial force and corresponding pressures for the desired stress the following Equation B.1 used where F_a is the force applied by the pressures, P_a is the axial pressure, P_c is the confining pressure, A_c is the area using the inside diameter of the cell, and A_s is the area of the piston which is equal to the area of the sample. The representation of the areas and forces is seen in Figure B.6. The axial stress is simply calculated as the axial force divided by the area of the sample.

$$F_a = P_a(A_c - A_s) - P_c(A_c - A_s) = \sigma_a A_s \quad (\text{B.1})$$

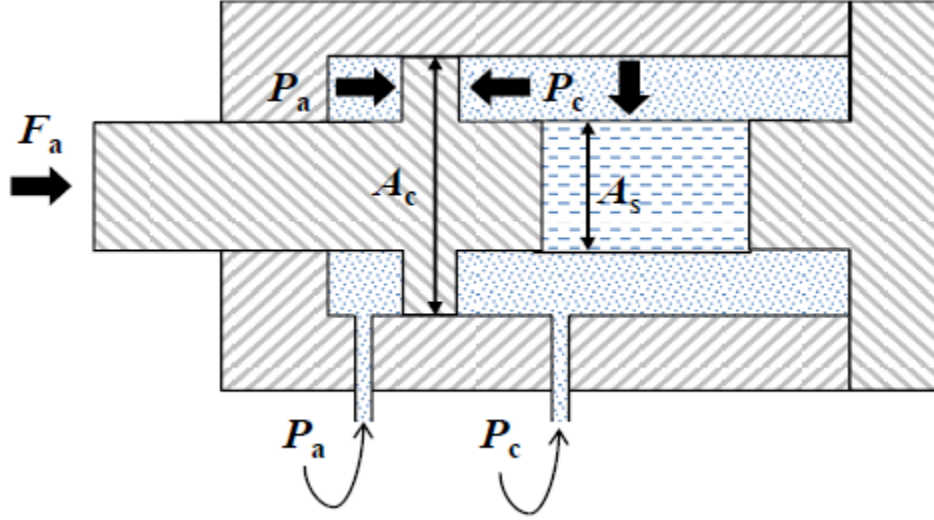


Figure B.6: Schematic of the forces applied and the variables required to determine the stress exhibited on the rock sample (Padin 2016).

Determination of the effective stress (σ_e) is performed understanding how the pore pressure (P_p) contributes to the strength of the formation, as displayed in Equation B.2. Biot's coefficient (α) accounts for the difference, or ability for the force to be transferred between the rock and fluid within the formation. Biot's coefficient is always equal to or less than one, and for this work it is assumed to be equal to one. Biot's coefficient is also directional dependent and can be formed into a tensor for a more accurate representation of the true conditions. A table displaying the pressure step ups with the respective effective stress is seen below in Table B.1.

$$\sigma_e = \sigma_a - \alpha P_p \quad (\text{B.2})$$

B.3 Pore Pressure Control System

The pore pressure system is controlled by two syringe ISCO pumps which are rated to a maximum pressure of 10,000 psi. The syringe pumps are controlled from a computer manually

Table B.1: Required pump pressures for the pressure step ups while maintaining constant effective stress.

Target Axial and Confining Stress		Required Pump Pressures		Effective Stress	Required Circulating Pressure	
σ_{axial}	σ_{radial}	P_a	P_r	σ_e	P_{pin}	P_{pout}
0	0	0	0	-	-	-
500	500	667	500	-	-	-
1000	1000	1333	1000	-	-	-
1500	1500	2000	1500	-	-	-
2000	2000	2667	2000	2000	0	0
2500	2500	3333	2500	2000	500	500
3000	3000	4000	3000	2000	1000	1000
3500	3500	4667	3500	2000	1500	1500
4000	4000	5333	4000	2000	2000	2000
4500	4500	6000	4500	2000	2500	2500
5000	5000	6667	5000	2000	3000	3000
5500	5500	7333	5500	2000	3500	3500
6000	6000	8000	6000	2000	4000	4000

due to the safety concerns of the high pressures. When changing the pressure it must be performed carefully as an abrupt change in pressure in the middle of an experiment could potentially ruin the work performed. The specifications for the syringe pumps are seen in Figure B.7. These pumps have the ability to pump a variety of fluids through the use of a storage cylinder. The cylinder keeps the pore fluid separate from the pumps fluid as to prevent any damage to the pumps precision seals. For the permeability tests nitrogen is utilized as pore fluid. For these tests a nitrogen tank is plumbed into the system with a regulator maintaining pressures at 3,500 psi. For the osmotic pressure tests NaCl and KCl brine solutions are utilized. The fluid in the pumps is deionized water which drives the cylinders to then pump the brine solution though the sample.

B.4 Data Acquisition System

The collection and storage of the data is essential for efficient and effective data analysis. Due to the length of the experiments the system must be capable of storing millions of points of data, making manual record of the data impossible. To control and record the pressures

100HLX Technical Specifications		
POWER REQUIREMENTS	<div> <div>117 ± 12 Vac, 1.5 A maximum</div> <div>234 ± 23 Vac, 0.75 A maximum</div> </div> } Factory Set	
LINE FREQUENCY	50 or 60 Hz	
LINE VOLTAGE NOISE TOLERANCE	1.7 × nominal rms line voltage, 10 µsecond pulses, any phase angle, random or repetitive	
DIMENSIONS	PUMP	CONTROLLER
	Width: 27.18 cm	27.18 cm
	Depth: 46.74 cm	30.48 cm
	Height: 101.09 cm	13.59 cm
WEIGHT	PUMP	CONTROLLER
	32.8 kg	2.96 kg
FLOW RATE RANGE	0.01 µl/min to 25 ml/min (for any pressure up to 689.5 bar)	
FLOW RATE ACCURACY ^a	± 0.3% (maximum 0.25 µl/min seal leakage)	
FLOW RATE DISPLAY RESOLUTION	0.01 µl/min (1.0 µl/min in Constant Pressure Mode)	
ANALOG OUTPUT ACCURACY ^b	± 1% of selected range	
DISPLACEMENT RESOLUTION	1.93 nl	
REFILL TIME	2.1 minutes	
REFILL OR DEPRESSURIZATION RATE	0.01 µl/min to 18 ml/min at any pressure from 0 to 689.5 bar	
PRESSURE RANGE	0.6895 to 689.5 bar	
PRESSURE ACCURACY	± 0.5% of full scale at constant temperature	
PRESSURE REPEATABILITY ^c	± 0.5% of full scale within 48 hours at constant temperature	
ZERO PRESSURE DRIFT	± 0.25% of full scale within 48 hours at constant temperature	
PRESSURE DISPLAY RESOLUTION	6.895 kPa	
AMBIENT TEMPERATURE RANGE	5 to 40°C	
TEMPERATURE DRIFT	± 0.12% of full scale/°C	
HUMIDITY	95% maximum	
CYLINDER CAPACITY	102.93 ml	
DEAD (HEADSPACE) VOLUME ^d	1.30 ± 0.020 ml	
POLLUTION DEGREE	2	
INSTALLATION CATEGORY	II	
MAXIMUM ALTITUDE	2000 m	

a. Using water at 137.9 bar and a temperature controlled environment at 30°C.

b. The analog output is an optional accessory.

c. Pressure repeatability specification is based upon re-zeroing pressure transducer every 48 hours.

d. Volume in and above the piston seal, head clearance at automatic shutoff, and inlet and outlet ports to the fittings.

Figure B.7: ISCO Syringe Pump specification sheet.

an automated system was developed. The system controls three ISCO syringe pumps and controllers, a LVDT, pressure transducer, temperature control, and sonic measurements.

The system has chosen is a National Instruments panel with eight channels of analog single-end input (14-bit, 48 KS/s), four channels of differential input and two analog outputs (12-bit, 150 S/s; 12 digital I/O, 32-bit counter). The panel fits the requirements of our test setup data acquisition system and is low cost.

Labview software is used as the interface on the computer to control the systems. The program allows for both visual and text-based programming to setup the system to collect the desired data. This is a very user friendly system and was one of the key reasons for the selection of this software. With the software, we are able to monitor and control the syringe pumps, the recordings from the LVDT due to axial strain, temperature and the sonic measurements. The rate of sampling from each tool can also be changed to meet our desired parameters. The viewed control interface of both the pumps and LVDT are shown in Figure B.8. The computer interface of the sonic measurements is shown in Figure B.9.

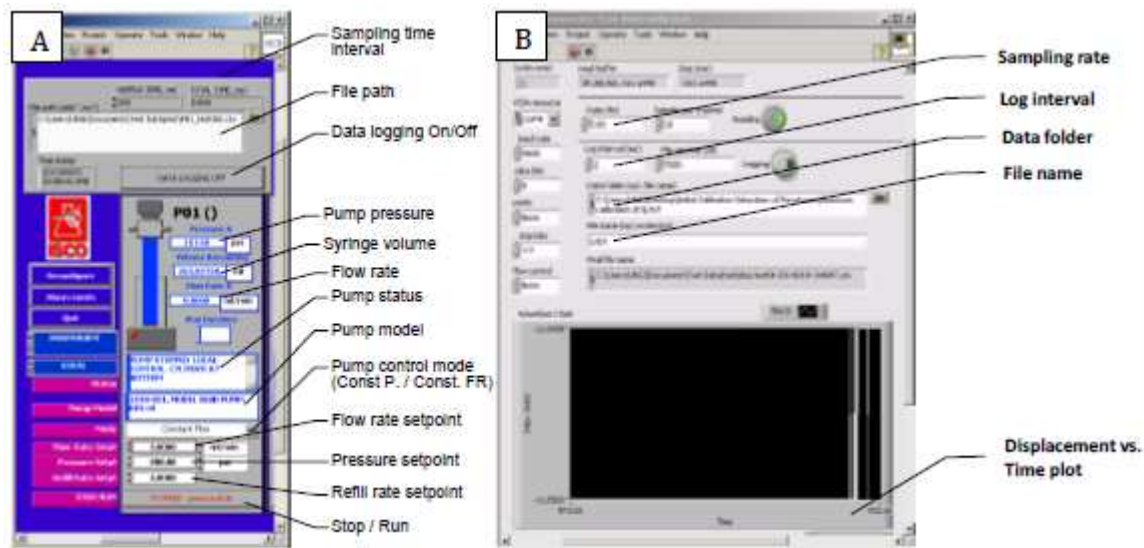


Figure B.8: (A) The interface control of the syringe pumps with labeled readings. (B) The interface control of the LVDT with labeled readings (Padin 2016).

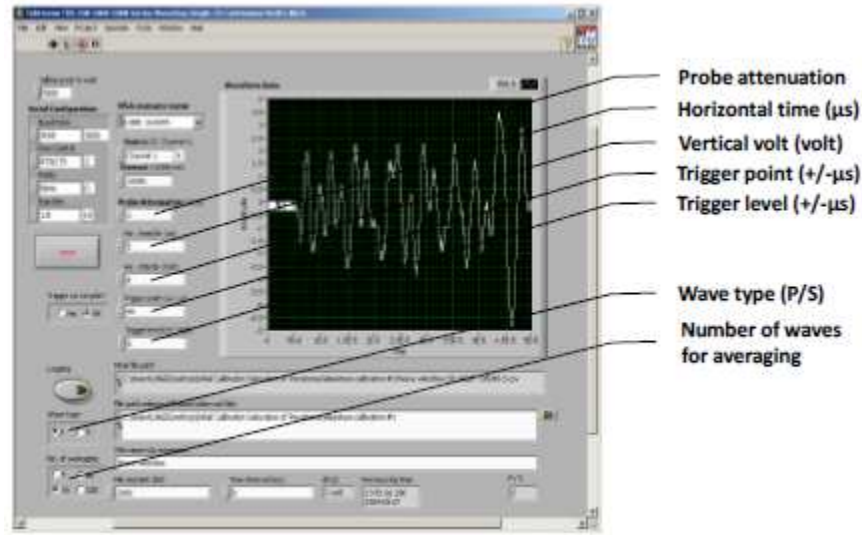


Figure B.9: Computer interface of sonic measurements with labeled readings (Padin 2016).

B.5 Pore Pressure Control System

Essential to monitoring the whole systems stress state is to measure the pore pressure. This is done using the injection pumps, downstream pumps and the DPT on the downstream (top) side of the sample. The pressure at the pumps is measured through the use of a high precision bi-directional Omegadyne pressure transducer with accuracy of $\pm 0.25\%$ FS BSL at the set calibration temperature of 25 degrees C. The DPT errors account for linearity, hysteresis, thermal hysteresis, thermal errors and repeatability. The DPT is a Stellar Technology transducer with a pressure error of 0.25% at the prescribed calibration conditions. Both transducers are shown in Figure B.10.

While calibrating our test setup with a shale sample it was determined that due to the restricted flow from both the brass electrode disks and the porous metal filters the pressure had to be slightly greater than what is required. It was determined that to achieve a pore pressure of 4000 psi across the sample a pump pressure of 4040psi at the injection (bottom) side of the sample is required. Once increasing the injection pressure, measured pressure on the downstream side was shown to be equal to the desired pressures of 4000 psi.

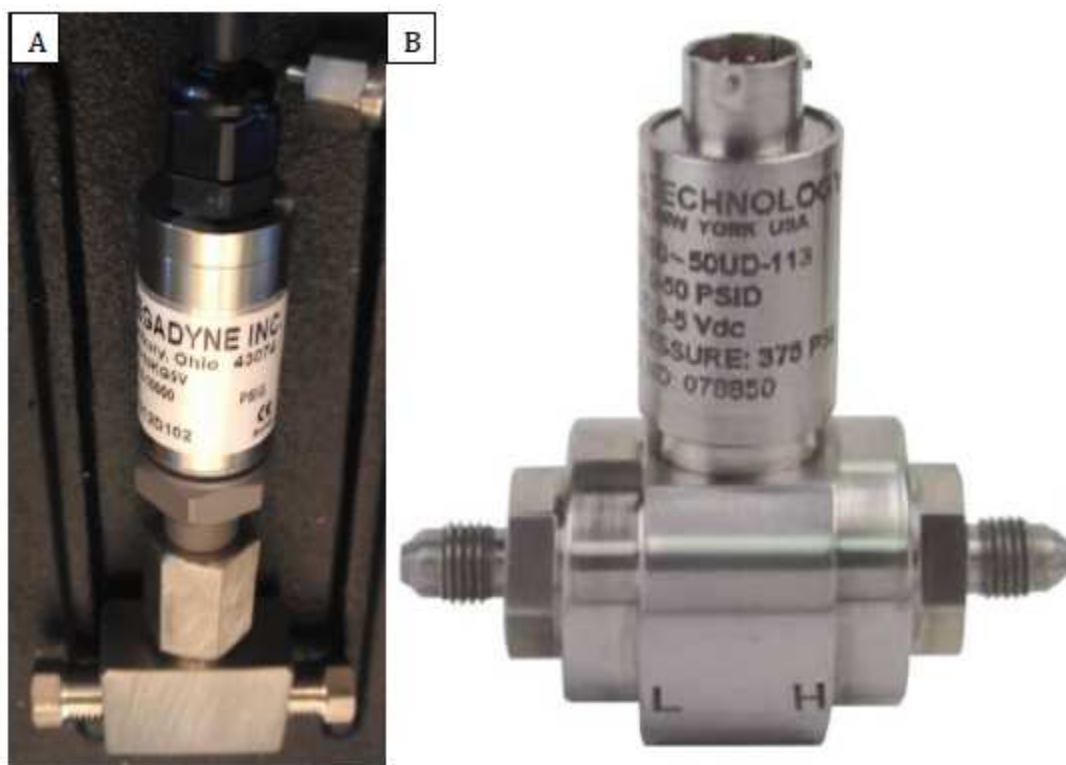


Figure B.10: (A) Pressure transducer used in coordination with the syringe pumps. (B) Pressure transducer used for the DPT (Padin 2016).

The pressure is measured as a change in voltage due to the dead volume and sent to the data acquisition system which interprets the voltage change and displays the appropriate pressure. Due to the voltage readings it is essential to calibrate the transducers to ensure they are accurately recording the observed pressures. Tests were performed to calibrate the transducers to pressures which would be used during the experiment, and up to the maximum output of the syringe pumps of 10,000 psi.

B.6 Linear Deformation Measurement System

Axial deformation of the sample is measured through the use of a linear variable differential transformer (LVDT) capable of measuring small deformations due to nano pores closing under stress. When the core sample is taken from the wellbore and brought to surface the sample decompresses and expands. For our tests the sample is brought back to in situ stress conditions in the consolidation stage and compresses back to in situ sizes. The deformation or strain back to down to size is measured with the LVDT. Also, more complex structure changes occur during the osmotic tests as pore pressures rise within the rock matrix. Increase in pore pressure decreases the effective stress on the rock and will open pore space. Any strain due to increased pore pressures can be measured by the LVDT too.

The LVDT is mounted to the top of the axial piston, as the piston moves the LVDT will recorded that movement. An image of the mounting can be seen in Figure B.11, along with the extensometer, digital readout, and calibration sample. The movement of this piston is directly related to the vertical strain of the core, the piston itself, the porous metal filters, and the electrode endcaps. Calibration of the strain was performed to determine the strain of the test materials as to isolate the strain of only the core.

B.7 Temperature Control System

The accuracy and reliability of the temperature control system is paramount to the success and accuracy of the pressure measurements. Temperature is well known to be a strong influence on pressure. This relation is compounded due to the small volume of liquids

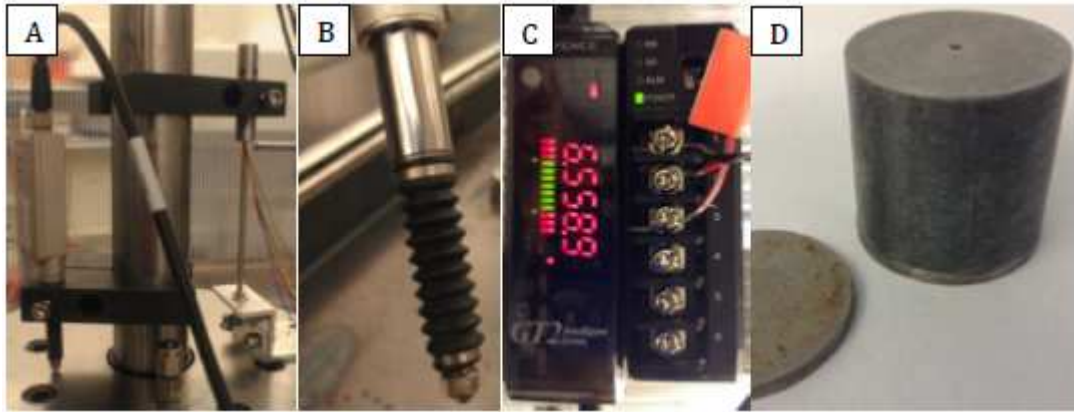


Figure B.11: (A) mounting the LVDT to the top axial piston. (B) The extensometer portion of the LVDT. (C) The digital readout and connection to the data acquisition system. (D) An aluminum plug used for calibration (Padin 2016).

flowing in the small diameter pipes. Due to the small volumes the influx of temperature can drastically change the pressure and not represent the true experimental affects. These same affects are compounded even greater for gas, as used in the permeability tests. To counter the temperature variance, a testing cabinet is built to hold all the equipment with a constant circulation of temperature controlled air at 40 degrees C.

Two heating elements combined each with circulating fans are attached to the corners of the testing cabinet. To control the temperature two sensors are used to both measure the testing cabinet interior temperature and adjust the heat output of the heating elements to match the desired set temperature. An image of the control system, the heating elements with fans, as well as fuse to cut off the electrical supply to the heater if the heat increase too much are seen in Figure B.12. The location of the heater and fans is displayed in Figure B.13.

B.8 Sonic Measurement System

The ultrasonic velocity measurement system utilizes piezoelectric transducers of 1 MHz central frequency. Both compressional and shear waves can be formed and sent through the sample for measurements. The wave is created by applying a high voltage, short time duration, electrical pulse to one of the transducers using an Oscilloscope. The Oscilloscope

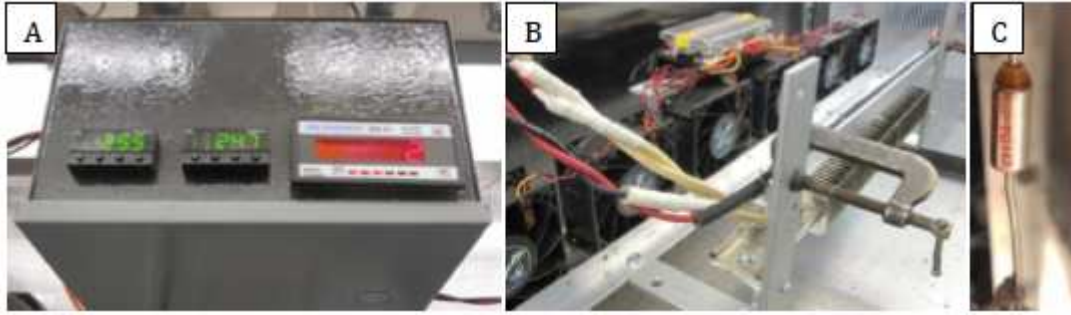


Figure B.12: (A) The temperature control system with interface to set the desired temperatures. (B) The heating element with fins and the fans used to circulate the air throughout the cabinet. (C) The fuse which if the heating element over heats will break the electrical source to shut off the heating element (Padin 2016).

used is an Olympus 5058PR designed for ultrasonic testing and measurements, used in attenuating mediums. The voltage used during testing does not exceed 400 volts.

The transducers are epoxied in place in the ends of the axial pistons of the triaxial cell. Covering the end caps are two additional aluminum disks to prevent deformation of the endcap and damage to the transducer. Wires run through the axial piston and out to two switch boxes which control the transmission of the wave to either the primary or shear wave. An image of the setup is seen in Figure B.14, which shows the removable endcap and transducer location. The transducers are connected to manual switches to change between Primary (P) waves and Secondary Shear (S) waves. The waves forms are sent and reviewed through a pulser/receiver and displayed on the oscilloscope. The oscilloscope can have the image screen adjusted to show the start time of the wave form and amplitude. This system is linked back to the data acquisition software LabVIEW to display and record the results on the computer.

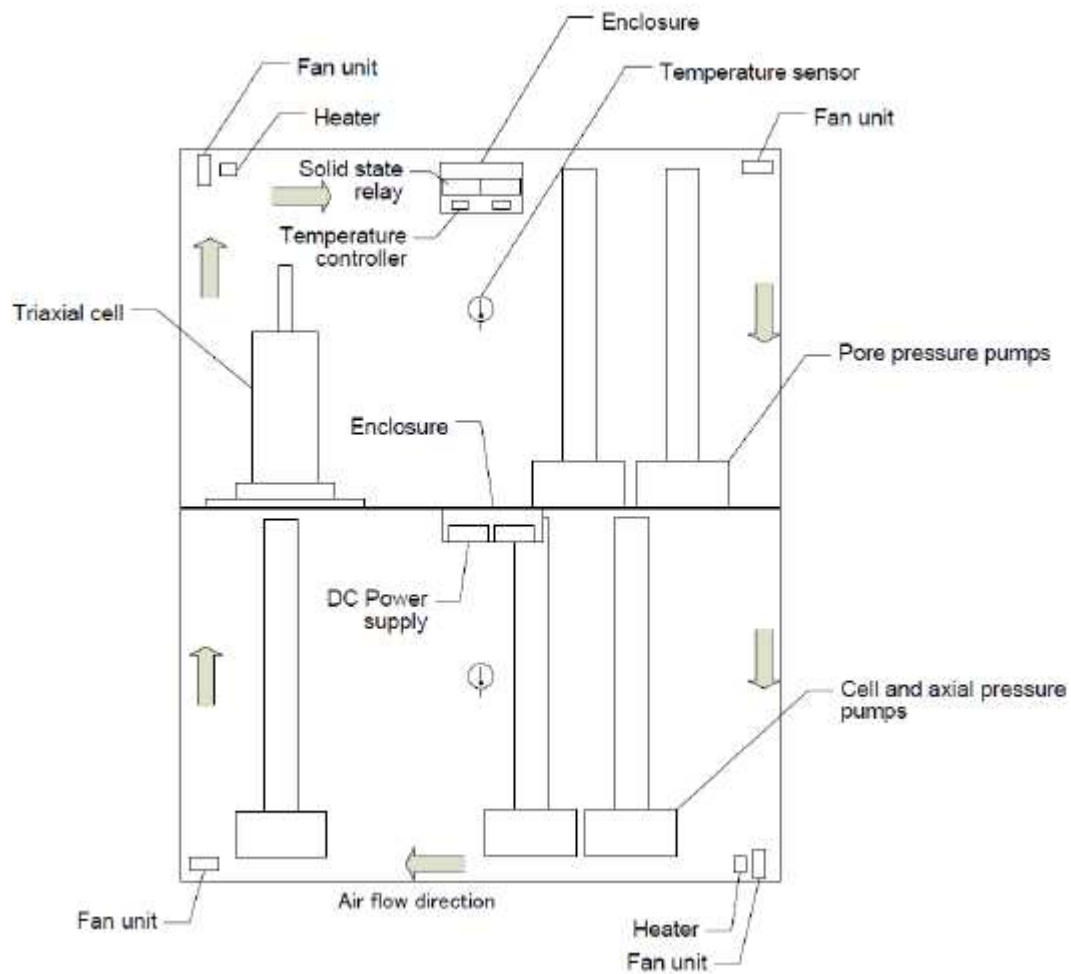


Figure B.13: Diagram of the location of the heating system and the circulation of the air within the temperature controlled cabinet.

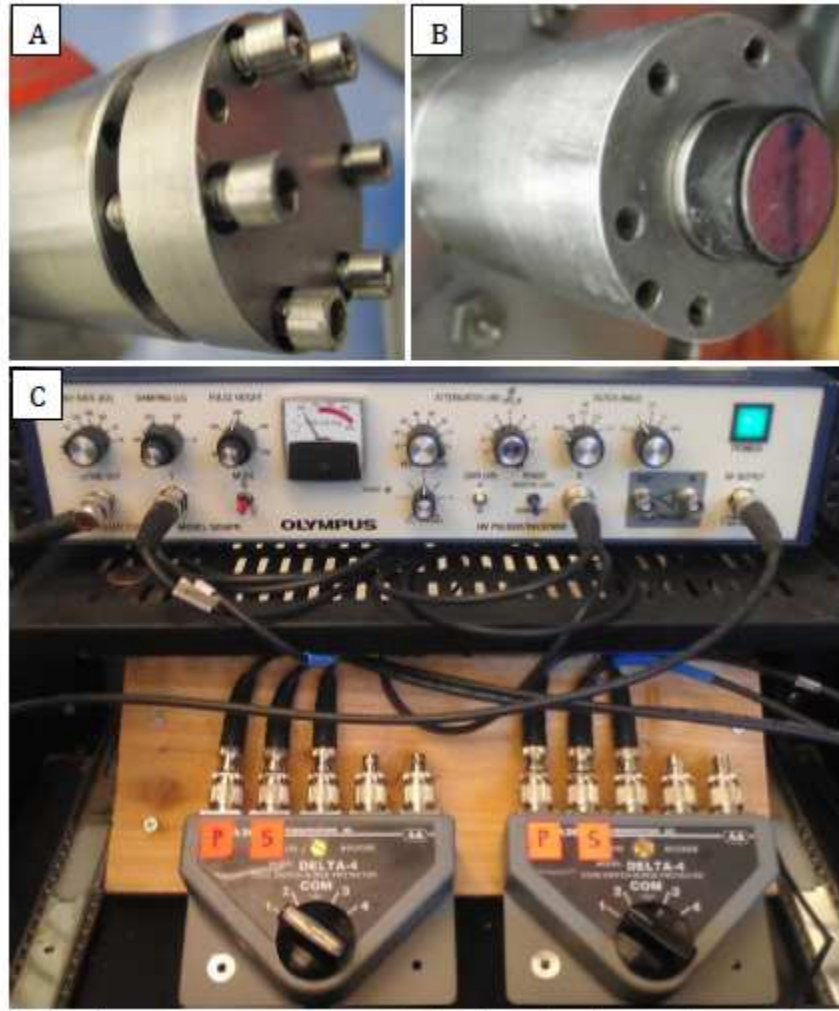


Figure B.14: (A) The endcap of the axial piston which can be removed to attach a transducer. (B) The transducer located within the piston. (C) The pulser/receiver and RF witches for changing between P and S waves measurements (Padin 2016).